FACILE FABRICATION OF NANOCARBON DERIVATIVES FOR OPTICAL AND ELECTROCHEMICAL APPLICATIONS

Synopsis submitted to CHRIST (Deemed to be University)
as partial requirement for the award of the Degree of

DOCTOR OF PHILOSOPHY

IN

PHYSICS

by

RIYA THOMAS

Under the Supervision of
Manoj B
Professor

CHRIST
(DEEMED TO BE UNIVERSITY)
BANGALORE · INDIA

Signature of Scholar **Signature of Supervisor**

CENTRE FOR RESEARCH
CHRIST (Deemed to be University)
BENGALURU

AUGUST 2022

CENTRE FOR RESEARCH

Approval of PhD Synopsis

[as per clause 11(k.) of CU Regulation for the Degree of Doctor of Philosophy, May 2019]

Name of Scholar:	RIYA THOMAS
Department:	PHYSICS AND ELECTRONICS
Name of Supervisor:	DR MANOJ B
Names of Research Advisory Committee: 1. DR IMRAN JAFRI R 2. DR SUMAN MANDAL	
Name and Designation of External Reviewer if applicable:	
Date of Synopsis Presentation:	12-07-2022
Title of the PhD thesis:	FACILE FABRICATION OF NANOCARBON DERIVATIVES FOR OPTICAL AND ELECTROCHEMICAL APPLICATIONS

Approved by:

1. Name of Supervisor: Dr Manoj B Signature:
2. Name of RAC Member: Dr Imran Jafri R Signature:
3. Name of RAC Member: Dr Suman Mandal Signature:
4. Name of External reviewer if applicable Signature:

Head of Department

Date of approval by Doctoral Committee:

Director Centre for Research

TABLE OF CONTENTS

1. INTRODUCTION 1

2. REVIEW OF LITERATURE 5

3. OBJECTIVES 8

4. MATERIALS AND METHODS 8

4.1 SYNTHESIS OF GRAPHENE DERIVATIVE FROM A LOW-COST ENERGY RESOURCE COKE 8

4.2 SYNTHESIS OF HETEROATOM DOPED COKE-BASED GRAPHENE DERIVATIVES FOR FLUORESCENCE BIOIMAGING AND ELECTROCHEMICAL SENSING APPLICATIONS 9

4.2.1 PREPARATION OF MODIFIED ELECTRODES 9

4.3 SYNTHESIS OF HETEROATOM DOPED, ACTIVATED COKE-BASED GRAPHENE DERIVATIVES FOR SUPERCAPACITOR APPLICATIONS 10

4.3.1 PREPARATION OF MODIFIED ELECTRODES 10

4.4 CHARACTERIZATION 11

5. RESULTS AND DISCUSSION 11

5.1 COKE-BASED MULTILAYER GRAPHENE DERIVATIVE: CHARACTERIZATION AND ELUCIDATION OF OPTICAL AND ELECTROCHEMICAL BEHAVIOURS 12

5.1.1 Structural and morphological analysis of coke-based multilayer graphene derivative 12

5.1.2 Elemental compositional analysis of the coke-based multilayer graphene derivative 12

5.1.3 Optical analysis of the coke-based multilayer graphene derivative 15

5.1.4 Electrochemical analysis of the coke-based multilayer graphene derivative 17

5.1.5 Conclusion 18

5.2 HETEROATOM ENGINEERING OF COKE-BASED MULTILAYER GRAPHENE DERIVATIVES FOR FLUORESCENCE BIOIMAGING AND ELECTROCHEMICAL SENSING APPLICATIONS 19

5.2.1 Structural and morphological analysis of the heteroatom doped multilayer graphene derivatives 19

5.2.2 Elemental compositional analysis of the heteroatom doped multilayer graphene derivatives 22

5.2.3 Surface chemistry analysis of the heteroatom doped multilayer graphene derivatives 24

5.2.4 Optical analysis of the heteroatom doped multilayer graphene derivatives 27

5.2.5 Fluorescence bioimaging of human melanoma cells using nitrogen doped multilayer graphene derivatives 32

5.2.6 Electrochemical analysis of heteroatom doped multilayer graphene derivatives 34

5.2.7 Electrochemical sensing of a high-risk abused drug, oxytocin using heteroatom co-

doped graphene derivative modified electrode 35
5.2.8 Conclusion 41

5.3 SIMULTANEOUS HETEROATOM DOPING AND ACTIVATION OF COKE-BASED MULTILAYER GRAPHENE DERIVATIVES FOR SUPERCAPACITOR APPLICATIONS ….41
5.3.1 Structural and morphological analysis of the heteroatom doped, activated multilayer graphene derivatives 42
5.3.2 Elemental compositional analysis of the heteroatom doped, activated multilayer graphene derivatives 44
5.3.3 Surface chemistry analysis of the heteroatom doped, activated multilayer graphene derivatives 44
5.3.4 Heteroatom doped, activated graphene derivatives as an electrode material for supercapacitor applications 48
5.3.4.1 Three-electrode cell configuration 48
5.3.4.2 Two-electrode cell configuration 49
5.3.5 Conclusion 52

6. SUMMARY AND FUTURE PROSPECTS 52

7. STRUCTURE OF THE THESIS 53

BIBLIOGRAPHY 54

LIST OF PUBLICATIONS 60

Journal publications 60

Manuscripts communicated 61

Book chapters 61

Patents filed 61

Patents communicated 61

LIST OF CONFERENCES AND WORKSHOPS ATTENDED 62

LIST OF TABLES

Table 1 Photophysical data obtained from the time-resolved fluorescence spectra 31

Table 2 Determination of oxytocin in real samples using heteroatom doped graphene modified electrode 40

LIST OF FIGURES

Fig. 1a X-ray diffraction pattern of coke and as-synthesized graphite oxide structure 12

Fig. 1b Raman profile of coke and as-synthesized graphite oxide structure 12

Fig. 2 SEM images of coke and as-synthesized graphite oxide structure 13

Fig. 3 FTIR analysis of coke and as-synthesized graphite oxide structure 14

Fig. 4 EDX spectra of coke and as-synthesized graphite oxide structure 14

Fig. 5a UV-Vis absorption spectra of coke and as-synthesized graphite oxide structure 15

Fig. 5b Tauc plot of coke and as-synthesized graphite oxide structure 15

Fig. 6 Fluorescence spectra of coke and as-synthesized graphite oxide structure 15

Fig. 7 CIE chromaticity diagram of coke and as-synthesized graphite oxide structure 17

Fig. 8a CV curves of coke and as-synthesized graphite oxide structure at 50 mV/s 17

Fig. 8b CV curves of as-synthesized graphite oxide structure at different scan rates 17

Fig. 8c GCD curves of coke and as-synthesized graphite oxide structure at 1A/g 17

Fig. 8d GCD curves of as-synthesized graphite oxide structure at different current densities 17

Fig. 8e The specific capacitance obtained for as-synthesized graphite oxide structure at different current densities 17

Fig. 8f Capacitance retention of as-synthesized graphite oxide structure electrode as a function of GCD cycle number under a current density of 15 A/g 17

Fig. 9a X-ray diffraction pattern of doped and undoped multilayer graphene derivatives 19

Fig. 9b Raman profile of doped and undoped multilayer graphene derivatives 19

Fig. 10a N_2 adsorption-desorption isotherms of doped and undoped multilayer graphene derivatives 21

Fig. 10b Pore size distribution of doped and undoped multilayer graphene derivatives 21

Fig. 11 SEM images of doped and undoped multilayer graphene derivatives 22

Fig. 12 FTIR spectra of doped and undoped multilayer graphene derivatives 22

Fig. 13 EDX spectra of doped and undoped multilayer graphene derivatives 23

Fig. 14 XPS survey spectra of doped and undoped multilayer graphene derivatives 24

Fig. 15a High-resolution XPS C1s deconvoluted spectra of doped and undoped multilayer graphene derivatives 25

Fig. 15b High-resolution XPS O1s deconvoluted spectra of doped and undoped multilayer graphene derivatives 25

Fig. 16a Surface atomic composition of different functionalities obtained from C1s peaks of doped and undoped multilayer graphene derivatives 26

Fig. 16b Surface atomic composition of different functionalities obtained from O1s peaks of doped and undoped multilayer graphene derivatives 26

Fig. 17a High-resolution XPS P2p deconvoluted spectra of doped and undoped multilayer graphene derivatives 27

Fig. 17b High-resolution XPS N1s deconvoluted spectra of doped and undoped multilayer graphene derivatives 27

Fig. 18 UV-Vis absorption spectra of doped and undoped multilayer graphene derivatives 27

Fig. 19 Fluorescence spectra of doped and undoped multilayer graphene derivatives 28

Fig. 20 Curve fitting analysis of fluorescence spectra at an excitation wavelength of 340 nm of doped and undoped multilayer graphene derivatives 29

Fig. 21 CIE chromaticity diagram of doped and undoped multilayer graphene derivatives 30

Fig. 22 Time-resolved fluorescence decay spectra of doped and undoped multilayer graphene derivatives 31

Fig. 23 Fluorescent microscopic images of human melanoma cells incubated with various concentrations of nitrogen-doped graphene derivative 33

Fig. 24 Cell viability evaluation of human melanoma cells incubated with increasing concentrations of nitrogen-doped graphene derivative 34

Fig. 25a Cyclic voltammetric responses of modified electrodes corresponding to 1mM $[Fe(CN)6]^{-3/-4}$ in 1M KCl solution at a scan rate of 100 mV/s 34

Fig. 25b Variation of peak current as a function of scan rate 34

Fig. 26a Square wave voltammetric responses of modified electrodes in the presence of 1mM oxytocin in 0.1M PBS at pH 7 36

Fig. 26b Variation of peak current for modified electrodes 36

Fig. 27 Schematic representation of the plausible mechanism for electro-oxidation of oxytocin 37

Fig. 28a The dependence of peak current of oxytocin (1mM) in 0.1M PBS for pH range 5 to 10 38

Fig. 28b The dependence of peak current of oxytocin (1mM) in 0.1M PBS on accumulation time 38

Fig. 28c Square wave voltammetric responses of modified electrode in 0.1M PBS at pH 7 for different concentrations of oxytocin 38

Fig. 28d Variation of peak current as a function of oxytocin concentrations 38

Fig. 29 Selectivity test of NPGH modified electrode in detection of 1μM oxytocin in the absence and presence of interfering species 39

Fig. 30a Square wave voltammetric responses of 5 different modified electrodes in 0.1M PBS at pH 7 for 1μM oxytocin 40

Fig. 30b Stability test of modified electrode after storage for 4 weeks 40

Fig. 31a X-ray diffraction pattern of doped and undoped, activated multilayer graphene derivatives 42

Fig. 31b Raman profile of doped and undoped, activated multilayer graphene derivatives 42

Fig. 32a N_2 adsorption-desorption isotherms of doped and undoped, activated multilayer graphene derivatives 43

Fig. 32b Pore size distribution of doped and undoped, activated multilayer graphene derivatives 43

Fig. 33 FTIR spectra of doped and undoped, activated multilayer graphene derivatives 44

Fig. 34 XPS survey spectra of doped and undoped, activated multilayer graphene derivatives 45

Fig. 35a High-resolution XPS C1s deconvoluted spectra of doped and undoped, activated multilayer graphene derivatives 46

Fig. 35b High-resolution XPS O1s deconvoluted spectra of doped and undoped, activated multilayer graphene derivatives 46

Fig. 36a Surface atomic composition of different functionalities obtained from C1s peaks of doped and undoped, activated multilayer graphene derivatives 47

Fig. 36b Surface atomic composition of different functionalities obtained from O1s peaks of doped and undoped, activated multilayer graphene derivatives 47

Fig. 37a High-resolution XPS N1s deconvoluted spectra of doped and undoped, activated multilayer graphene derivatives 48

Fig. 37b High-resolution XPS P2p deconvoluted spectra of doped and undoped multilayer graphene derivatives 48

Fig. 38a CV curves of heteroatom doped and activated multilayer graphene derivatives at 50 mV/s in 3-electrode cell configuration 49

Fig. 38b GCD curves of heteroatom doped and activated multilayer graphene derivatives at 1A/g in 3-electrode cell configuration 49

Fig. 38c Specific capacitance obtained at different current densities in 3-electrode cell configuration 49

Fig. 38d Capacitance retention of modified electrode as a function of GCD cycle number under a current density of 15 A/g in 3-electrode cell configuration 49

Fig. 39a CV curves of heteroatom doped and activated multilayer graphene derivatives at 50 mV/s in 2-electrode cell configuration 50

Fig. 39b GCD curves of heteroatom doped and activated multilayer graphene derivatives at 1A/g in 2-electrode cell configuration 50

Fig. 39c Specific capacitance obtained at different current densities in 2-electrode cell configuration 50

Fig. 39d Capacitance retention of modified electrode as a function of GCD cycle number under a current density of 15 A/g in 2-electrode cell configuration 50

Fig. 40a Nyquist plot of heteroatom doped and activated multilayer graphene derivatives 51

Fig. 40b Ragone plot of heteroatom doped and activated multilayer graphene derivatives 51

1. INTRODUCTION

The world scientific community is currently concerned in research focusing on the large-scale production, characterization, and real-world applications of graphene and its derivatives. Owing to their unique physico-chemical characteristics, graphene-based materials are exploited to make a significant breakthrough that could be commercially utilized and implemented into everyday life. For nearly a decade, graphene and its derivatives have been realized for their exceptional performance in the field of sensors, biomarkers, supercapacitors, batteries, and medical technologies [1] [2]. Therefore, graphene-based materials could be designated to be a solemn substitute for many conventional materials in several application areas like energy, healthcare, quality control, agriculture, and transportation, enabling fervent innovations and new horizons of possibilities.

The foremost issue discussed with in the current study is the requirement for the early-stage detection of cancer, a leading cause of human death worldwide. As far as global case fatalities are concerned, cancer has the highest mortality rate compared to other diseases. It is well known that; an early cancer diagnosis and effective treatment could significantly reduce the number of cancer fatalities. In recent years, the occurrence of melanoma, a serious type of skin cancer has increased in comparison to other cancer cases. This highly resistant cancer accounts for around 3% out of all malignant tumor cases. Despite the fact that it is only 4% out of all skin cancer types, it causes approximately 80% of all death from skin cancer. The rate of growth and spread of this tumor is rapid. However, if melanoma can be diagnosed at an early pace, it can be readily cured by simple surgical excision.

Molecular imaging technique would be of great significance in the clinical diagnosis and prognosis of cancer, facilitating early-stage detection. Among the various molecular imaging tools, optical or fluorescence imaging can provide real-time monitoring of cellular activities by means of various wavelengths emitted by the fluorescent biomarkers[3]. The imaging probes enables the visualization of molecular process at a cellular or molecular level without perturbing them. The organic dyes, synthetic fluorophores, and conventional semiconductor-based quantum dots known for their superior fluorescence characteristics are highly toxic. Also, the involvement of heavy metals in the synthesis procedure involves an increased cost of production owing to their expensive precursors, which ultimately hinders its complete utilization in bioimaging applications[4].

The second issue dealt with in the current study is the need for real-time surveillance over the perpetual misuse of a high-risk abusive drug, oxytocin, especially in dairy farming

and agriculture. The injection of oxytocin in lactating cattle has become a widespread and unregulated practice to enhance milk production commercially. This hormone leads to the contraction of mammary glands of milch cattle to secrete more milk and, as such, is a cause for deterioration of cattle's health. Even though oxytocin is a mammalian hormone, it has also been injected into stems and roots of plants as a growth promoter. The plants administered with oxytocin stimulate the growth hormones to yield fruits and vegetables of bigger sizes, seeming fresh and plump. Most of the research work discloses that the intake of edibles containing oxytocin over a period of time can engender irreparable damage to human health. It might cause nausea, heart disorders, nerve failures, sterility, memory loss, etc. Recently, many media reports show that oxytocin is used to expedite puberty in under-age girls. The uncontrolled shots given to the girls make them reach sexual maturation earlier and are then pushed into prostitution. Hence, the development of sensitive methods for the determination of oxytocin is a substantial requisite for food safety, as well as societal well-being.

In recent years, several analytical methods such as high-performance liquid chromatography (HPLC) [5], capillary electrophoresis [6], and immunoassay procedures [7] are applied for the quantification of oxytocin. But these techniques are expensive, laborious, in need of sophisticated instrumentation, a tremendous amount of reagents and solvents, pre-treatment of samples, etc. To avoid these obstacles, an electrochemical assay, which is a simple analytic procedure, that responds in a fraction of milliseconds with high sensitivity, has been developed for the sensing of oxytocin [8], [9]. However, some shortcomings still exist and restrict the practical applications of the above electrochemical detection methods, such as tedious electrode fabrication and pre-treatment, the need for waveform modifications for enhanced sensitivity, and a narrower detection range. Therefore, the development of electrochemical sensors expending highly sensitive analytical techniques and effectual electrocatalysts is a pressing need for the quantification of oxytocin.

The third issue dealt with in the current study is the expanding appetite for energy demand which arouses from the upsurge in the world's population and interminable industrial activity. To overcome this energy deficit concern, the energy sources and storage technologies should not only follow the load change but also be capable of balancing the output fluctuations. For this purpose, an electrochemical energy storage system (EES) is considered to be a powerful practical means for pursuing enhanced power quality and energy efficiency. The supercapacitor, as an energy storage device, can bring many advantages, such as fast charge/discharge, high power density, long cycle life, less maintenance, current stabilization, and no environmental pollution, which make it distinct from other storage technologies[10].

With a number of such advantages, supercapacitors have been interested in various applications such as portable electronics, electric vehicles, aircraft, energy power systems, and so on.

Significant efforts have been made by researchers in the field of supercapacitors to find an ideal electrode material for achieving its best electrochemical performance. On the basis of charge storage mechanism, supercapacitors can be classified into electric-double layer capacitors (EDLC), pseudocapacitors, and a combination of both (hybrid). EDL capacitors make use of electrode material's high surface area and store energy electrostatically by an electric double layer accumulated at the electrode-electrolyte interface[11]. In contrast, pseudocapacitors store energy via fast and reversible surface redox reactions of active materials in electrodes, such as conductive polymers or metal oxides[12]. Though EDL capacitors exhibit good stability, the capacitance values are often limited and only 10-20 % of theoretical capacitance is observed. Furthermore, the pseudocapacitance component is not desirable in many applications due to its slow response time and high capacitance decay rate. So, in order to obtain improved supercapacitor efficiency, both of these mechanisms should be incorporated into a single electrode material. These either require several steps during the synthesis process or post-synthesis treatments, which are obstacles to large-scale fabrication.

Heteroatom-doped graphene-based materials have held a lot of potential in fluorescence applications[13] and electrochemical fields, such as supercapacitors[14], and electrochemical sensors[15] owing to the structural, chemical, and electronic modifications induced in pristine graphene lattice by the dopants. Especially, nitrogen and phosphorus with atomic radii comparable to a carbon atom and possessing higher electron-donating ability make them the preferred choice for its adoptions as dopants in graphene-based materials. The introduction of heteroatoms such as N, and P, can alter the electronic transport characteristics as well as fluorescence properties[16]. Thus, the utilization of heteroatom doped graphene as a biomarker facilitates the feasibility of bio-related applications. In addition, excellent electronic and ionic conductivity stemming from heteroatom doping is beneficial to augmenting its electrocatalytic and capacitive performance.

The simultaneous doping of heteroatom can provide a new range of novel materials compared with singly doped material. Among other doping elements, nitrogen and phosphorus positioned in the same column of the periodic table could also eliminate the competing interactions from co-doping. Therefore, nitrogen and phosphorus dual-doped graphene (NPG) could exhibit even superior performance rather than mono-doped graphene because of the so-called synergistic effect [17]. In recent years, many studies have been reported on the improved optical and electrochemical performance of carbon-based catalysts upon co-doping of nitrogen

and phosphorus[18], [19]. Overall, co-doping of two elements into the graphene matrix further advances the application potential of graphene-based materials.

The selection of carbon precursors and adopted synthesis routes play a pivotal role in the large-scale fabrication and commercialization of as-synthesized graphene-based materials. Carbon precursors used for the extraction of graphene and its derivatives are relatively expensive, and some entail high purity. Also, the synthesis techniques include lengthy extraction steps and high manufacturing costs. It is a known fact that fossil fuel coal possesses a highly ordered nanocrystalline sp^2 carbon network[20]. Developing countries where coal is the foremost stock of energy have a higher human death toll every year due to the air pollution arousing from the liberation of the massive amount of greenhouse gases like CO_2, and N_2O from the combustion of coal. Therefore, the utilization of coal as a carbon precursor also enables the transformation of pollution-causing fossil fuel into a value-added product captivating for multipurpose applications.

The preformed clusters of graphitic domains in coal facilitate easier oxidative displacement, exfoliation, and functionalization of carbonaceous nanomaterials employing simple synthesis techniques compared to synthetic graphite. The higher crystallinity of precursors is a mandatory criterion to derive the finest graphene derivatives. Therefore, coke which is known to be the highest quality coal turns out to be an efficient precursor as it holds higher carbon content and fewer impurities. The higher crystallinity results from the enhanced graphitization of parent coal can also sustain lower interface resistance between electrode and electrolyte favoring better electrochemical performance[21]. Moreover, the defect densities enable the energy transition between π-π^* states of the localized electron in sp^2 domains stimulating the photoluminescence emission. Hence, an optimal degree of defects can contribute toward better electrochemical kinetics and proficient photoluminescence mechanisms.

While research in the area of coal-based graphene systems has been very intense in the last few decades, the reports on the optical and electrochemical properties of coke-based graphene derivatives are scarce. In addition, tailoring the corresponding range of physicochemical properties via heteroatom (N, P) doping is an important aspect that requires in-depth investigation for materializing the full application potential of coke-based graphene derivatives. There is a dearth of explicit research on these heteroatom-doped graphene derivatives for their feasible, economical production and affordable practical applications in everyday life to address significant social issues.

2. REVIEW OF LITERATURE

Among all the carbon-based allotropes, research groups across the globe are currently devoting significant attention to the 2-D dimensional allotropic form of carbon termed, graphene in the hope of discovering an application worthy of top-notch. The potential of graphene-based materials is virtually unlimited and promises to revolutionize many fields from energy, electronics, or even health.

Understanding the physicochemical process involved in a biological system and exploring fundamental cellular activities is a prerequisite for cancer theranostics. Various molecular imaging techniques such as magnetic resonance imaging, ultrasound imaging, computed tomography imaging, and fluorescence imaging are being explored for the detection of cancer at an early stage[22]. However, optical or fluorescence imaging can provide highly sensitive detection through imaging probes that can emit light in a range of wavelengths. Up to date, nanomaterials such as semiconductor quantum dots, upconverting nanoparticles, and noble metal nanoparticles are utilized as fluorescent biomarkers for bioimaging applications. However, the inherent limitations in optical and biocompatible properties restricted their widespread applications in bioimaging.

Graphene-based materials could overcome the limitations of traditional quantum dots in regard to their tunable emission, photostability, biocompatibility, solubility in water, and ease of functionalization. Graphene and its derivatives have got superior physiochemical characteristics required by a biomarker for capturing explicable images of biological matter. Significantly, the hydrogen bonding between the graphene surface and oxygen functional groups observed in single or multilayer graphene oxide can exert excellent surface reactivity that can contribute to the adsorptive capability of drugs or biomolecules and growth aspects beneficial for *in-vivo* cellular imaging[23]. Doping of heteroatoms into the graphene system can modulate the electronic structure by altering its functional sites and chemical composition, which considerably improves the fluorescence emission properties. Among the various heteroatoms, nitrogen and phosphorus that are comparable to the size of the carbon atom and possess high electron-donating capability can contribute toward an enhanced fluorescence quantum yield[16]. In this case, it would be prudent to investigate the possibility of applying heteroatom atom doped graphene for fluorescent bioimaging of human melanoma cells.

The naive detection of potentially hazardous drug oxytocin is a vital requisite, owing to its deleterious impact on societal affluence prompted by the unconstrained usage. There is an increased interest in the accurate determination of oxytocin levels in the body; however,

research in this area has unfortunately been limited by the lack of noninvasive methods, especially considering the involvement of vulnerable patient populations. Peptides, like oxytocin, can also be detected through methods like mass spectrometry and various forms of chromatography but are sometimes very time-consuming and can be destructive. On the other hand, it has been known that some amino acids are redox-active and that can be measured with electrochemical techniques that are very suitable for on-site and in situ analysis[24]. The electrochemical detection of oxytocin was reported using cyclic voltammetry scans in conjugation with a boron-doped diamond electrode[9] and carbon fiber microelectrode [25]. In addition, a modified sawhorse waveform has also been formulated for the voltammetric detection of oxytocin[8]. Recently, a chemosensor developed with the combination of a microfluidics platform, molecular imprinting technology, and electrochemical transduction is used for oxytocin determination in biological samples[26]. Although all the above materials exhibited improved voltammetric signals, the involvement of expensive electrodes and sophisticated electrode fabrications, emphasizes the need for developing new materials as well as a sensitive analytical technique for the quantification of oxytocin.

Among all the electrochemical methods, stripping voltammetric analysis provides a powerful tool for the determination of peptides, which possess high sensitivity and fast response time. The development of electrochemical sensors expending especially graphene-based materials has attracted remarkable academic efforts in detection studies due to its high electrical conductivity, ease of functionalization, and fast heterogeneous electron transfer. Several studies have displayed that the doping of heteroatoms (N, P, B) into the graphene system can further enhance its electrochemical characteristics [27]. The charge polarization between carbon atoms and dopants boosts the electron transport, which facilitates the conductivity of graphene lattice. The introduction of dopants can exert alterations in the local chemical environment via tuning of structural defects and functional groups [28]. This ultimately results in improved charge-carrier densities and active sites, which leads to significant electrocatalytic activity. Consequently, there is an immense research opportunity in this field because it is pivotal to recognize the role of the heteroatom atom doped graphene derivative on the electrocatalytic attributes appropriate for an ultrasensitive and anti-fouling electrochemical detection of oxytocin.

The crisis instigated by the imbalance in world's energy supply and demand has led to the research and development of energy storage devices with high efficiency and performance. In this context, supercapacitors have gained increasing attention as a promising candidate for

electrochemical energy storage systems as they can store a large amount of energy, typically 10 to 100 times more energy per unit mass or volume compared to the electrolytic capacitor.

Among the active materials used in supercapacitor electrodes, graphene is of great interest owing to its high theoretical surface area, tunable structure, and excellent conductivity. The outstanding capacitance performance of graphene-based supercapacitors was first reported in 2006 by Jang and his group and its technological significance is now being more widely recognized[29]. Despite these advantages, the electrochemical performances of graphene itself are still hindered by the restacking nature resulting in low active surface area and poor charge storage capability. Recently, many researchers have demonstrated that besides the physical restructuring, tailoring of chemical properties of graphene could result in its improved supercapacitive performance. Doping with heteroatoms such as nitrogen, sulphur, and phosphorus has been preliminarily proven to be an effective method to enhance the capacitance behavior, due to the electronic manipulations by the dopants. Among these heteroatoms, N-doping is advantageous to improve both physical and electrochemical properties such as wettability, capacitive performance, and energy/power densities respectively which can have a positive impact on the overall performance of the system[30]. Phosphorus displays analogous chemical properties to nitrogen since it has the same number of valence electrons, but the higher electron-donating capability and larger atomic radius make it the preferred choice for its application in the broad field of energy storage[31]. However, there is still enormous scope to enhance the capacitive-ability of these electrochemical devices further which is achievable through co-doping of heteroatoms. The doping of nitrogen and phosphorous results in improved charge storage due to the additional pseudo-capacitive component alongside the electric double layer since they have electron-donor characteristics and also an enhanced transport capability due to their exceptionally high electrical conductivity[28]. At the same time, better control over the textural properties (mainly pore size) is desirable to maximize the energy and power densities to fulfill future energy demands. Often, doping leads to blockage of pores which sometimes leaves the doping process inefficient. Besides, a substantial reduction in cost is essential, and it is likely that precursors will play a key role. Therefore, it is highly necessary to develop a technique that achieves simultaneous activation and doping for fabricating heteroatom-doped graphene derivatives from a low-cost, readily available, and renewable precursor.

In contrast to the widely studied world of synthetic graphite-like precursors, the optical and electrochemical properties of globally available, low-cost, and naturally formed carbonaceous materials like coal are worth investigating. The potential of coal in deriving

carbon nanostructures was first reported by Pang and the group via successful extraction of fullerenes (C_{60})[32]. An increased amount of carbon content in coal significantly implies the availability of larger carbon clusters for the extraction of graphene structures. Novel graphene derivatives are synthesized from different types of coal namely bituminous coal, sub-bituminous coal, lignite, and anthracite[33]. Coke, which is made by the thermal annealing of coal, has a higher carbon content and fewer impurities. Thus, coke is considered to be an excellent carbonaceous precursor for the extraction of graphene-based structures. But, in order to unlock the potential of these materials, it is crucial to develop compatible methods of processing them. Moreover, the facile fabrication of heteroatom doped graphene derivatives from coke is of high importance for acquiring application-specific requirements.

Accordingly, the research work presented herein would focus on the facile, scalable, and cost-effective synthesis of heteroatom doped graphene derivatives from high-rank coal, termed coke. Moreover, three critical issues confronting our society at the moment: Early-stage detection of cancer, misuse of the high-risk drug oxytocin, and the high demands of energy, would be addressed by the as-synthesized heteroatom doped graphene derivatives.

3. OBJECTIVES

The present study aims to fabricate novel heteroatom doped graphene derivatives from coke and its utilization for the most demanding real-world applications in quality control, health care, and energy sectors with the following objectives.

- To fabricate graphene derivative from low-cost energy resource, coke by a facile and scalable synthesis route
- To modify the optical and electrochemical characteristics of as-synthesized coke-based graphene derivatives via heteroatom doping for the applications in fluorescence bioimaging of human melanoma cells and electrochemical sensing of oxytocin
- To modify the textural and energy storage characteristics of as-synthesized coke-based graphene derivatives via simultaneous heteroatom doping and activation for supercapacitor application

4. MATERIALS AND METHODS

4.1 SYNTHESIS OF GRAPHENE DERIVATIVE FROM A LOW-COST ENERGY RESOURCE COKE

Improved Hummer's method with modification was adapted for the preparation of graphite oxide from coke. 3g of coke and 18g of $KMnO_4$ were added slowly to the solution of concentrated H_2SO_4 and H_3PO_4 taken in the ratio 9:1 (360ml: 40ml). The mixture is then constantly stirred for 12 h at 50 ºC. The solution is cooled and transferred onto a mixture of ice (200g) and H_2O_2 (3ml). The resulting mixture is centrifuged at 4000 rpm for about 20 minutes and the supernatant is decanted away. The residue is washed multiple times with diluted HCl, ethanol, and distilled water to remove the suspended metal ions until a neutral pH is attained. The residue is further purified by dialysis for 3 days. The separation of graphene sheets was assisted by the ultrasonication of the sample for 1h and finally vacuum dried at 80 ºC for 24h. The resultant coke-derived oxidized graphitic structure is labeled as GrO.

4.2 SYNTHESIS OF HETEROATOM DOPED COKE-BASED GRAPHENE DERIVATIVES FOR FLUORESCENCE BIOIMAGING AND ELECTROCHEMICAL SENSING APPLICATIONS

To prepare nitrogen and phosphorus co-doped graphene (NPG_H), 2 mg/ml of coke-derived graphite oxide was combined with 2.5 ml of phosphoric acid and 3.5 ml of ethylenediamine under stirring. The reactant mixture was ultrasonicated for 1 h at 40 ℃ and transferred to the autoclave for hydrothermal reaction at 180 ℃ for 12 hrs. After filtering, the resultant residue was purified via repeated washing with water, and the slurry was dried in a vacuum oven at 80 ℃. Similarly, nitrogen-doped graphene (NG_H) and phosphorus-doped graphene (PG_H) were prepared following the same procedure using 7 ml of ethylenediamine and 5 ml of phosphoric acid as nitrogen and phosphorus sources, respectively. For comparison, the graphite oxide hydrothermally treated in the absence of dopants produced a sample that was denoted as G_H.

4.2.1 PREPARATION OF MODIFIED ELECTRODES

The heteroatom doped graphene derivative prepared in section 4.2 was used for the modification of working electrode for electrochemical sensing applications. 10 mg of synthesized sample is dispersed in 950 µL of Isopropyl Alcohol with 50 µL of Nafion as a binder. To obtain a homogenous suspension, the mixture was ultrasonicated for 15 minutes. Subsequently, 10 µL of suspension was cast onto a mirror-polished Platinum working electrode and left to dry.

The electrochemical measurements were performed with the Platinum electrode as the working electrode, saturated calomel electrode, and Platinum wire as reference and counter electrode. The electrochemical sensing was carried out employing square wave stripping voltammetry (SWSV) in 0.1M PBS buffer (pH 7) as the electrolyte. All the sensing experiments were repeated thrice to ensure reproducibility.

4.3 SYNTHESIS OF HETEROATOM DOPED, ACTIVATED COKE-BASED GRAPHENE DERIVATIVES FOR SUPERCAPACITOR APPLICATIONS

To prepare heteroatom doped and activated graphene derivative, 250 mg of coke-derived graphite oxide was impregnated with 0.5 ml of 85 wt% H_3PO_4. The mixture was kept overnight stirring and the obtained slurry was activated at 800 °C in a tubular furnace for 3 h under an N_2 flowing atmosphere. The resulting sample was washed multiple times with water and dried in a vacuum oven at 80 °C (sample coded as PG_A). To prepare nitrogen-doped graphene derivative, coke-derived graphite oxide was dispersed in distilled water and, next ethylenediamine was added to the dispersion. The mixture was kept for stirring under 80 °C for 6 h and the obtained slurry is subjected to thermal annealing at 800 °C in a tubular furnace for 3 h under an N_2 flowing atmosphere. The resulting sample was washed multiple times with water and dried in a vacuum oven at 80 °C (sample coded as NG_A). The same phosphoric acid activation procedure is followed on NG_A, to obtain a co-doped and activated graphene derivative (NPG_A). For the comparative studies, thermal annealing of graphite oxide at 800 °C in the absence of dopants produced a sample that was coded as G_A.

4.3.1 PREPARATION OF ELECTRODES

The capacitive properties of heteroatom doped and activated graphene derivatives are evaluated using 3-electrode and 2-electrode systems. For the 3-electrode measurements, the prepared material (in section 4.3) and Nafion (5 wt%) were taken in the ratio 10:1 and dispersed in isopropyl alcohol via sonication. The slurry was coated on the glassy carbon working electrode and subsequently dried at room temperature. The Voltammetric measurements were performed using saturated Calomel and Platinum wire as reference and counter electrode respectively. For making 2-electrode measurements, the prepared material is homogeneously dispersed in ethanol by sonication. Then, the prepared slurry is coated on carbon cloth (area of ~ $1cm^2$) to form a slice as the working electrode. The mass loading for each electrode was ~ 2 mg.

The electrochemical performance was evaluated using cyclic voltammetry with varied scan rates and galvanostatic charge-discharge with a varied a current at potential window of -0 V to 0.8 V. The electrochemical impedance spectroscopy was performed from 1Hz to 100 kHz with a potential amplitude of 5mV/s.

4.4 CHARACTERIZATION

The X-ray pattern of the samples was recorded using Rigaku 6000 X-ray diffractometer with Cu Kα as the radiation source. Structural characterization was carried out using inVia Raman Microscope at 514 nm laser excitation wavelength The surface morphology and elemental composition were obtained using the SEM-EDS model GEMINI ULTRA55. Functional groups were identified with the aid of the Shimazdzu IR spirit-FTIR spectrophotometer. Absorption characteristics were obtained employing the UV-Vis spectrometer JAZ series of Ocean Optics. Shimadzu Fluoro-spectrometer (RF-5301) was used for recording photoluminescent spectra. The compositional analysis was carried out by X-ray Photoelectron Spectroscopy (XPS) (Omicron ESCA probe, Mg Kα X rays). Voltammetric measurements were performed on electrochemical work-station model CH 660E. Fluorescent microscopic images were obtained through an inverted phase-contrast fluorescence microscope at 20 X magnification. The evaluation of cytotoxicity was done by MTT (3-(4,5-dimethythiazol2-yl)-2,5-diphenyl tetrazolium bromide) assay.

5. RESULTS AND DISCUSSION

The current study focuses on the extraction of graphene derivative from low-cost energy resource coke and modification of its physico-chemical properties via heteroatom doping for the utilization in a wide range of potential applications. Firstly, oxidized multilayer graphene derivate was synthesized from precursor coke via a facile acidic oxidation technique and a detailed investigation of structural, morphological, elemental, optical, and electrochemical properties was carried out. Secondly, the as-synthesized multilayer graphene derivatives are further tailored in terms of their fluorescence and electrochemical attributes via doping of nitrogen and phosphorus; and explored its potential in bioimaging and electrochemical sensing applications. Thirdly, simultaneous heteroatom doping and activation of as-synthesized multilayer graphene derivatives are achieved and their efficacy in supercapacitor applications is studied through detailed analysis.

5.1 COKE-BASED MULTILAYER GRAPHENE DERIVATIVE: CHARACTERIZATION AND ELUCIDATION OF OPTICAL AND ELECTROCHEMICAL BEHAVIOURS

In the current study, the utilization of fossil fuel coke for fabricating multilayer graphene derivative via Improved Hummers' method is discussed. The structural, morphological, elemental, optical, and electrochemical characteristics of the as-synthesized coke-based graphite oxide (GrO) structure are also presented in detail.

5.1.1 Structural and morphological analysis of the coke-based multilayer graphene derivative

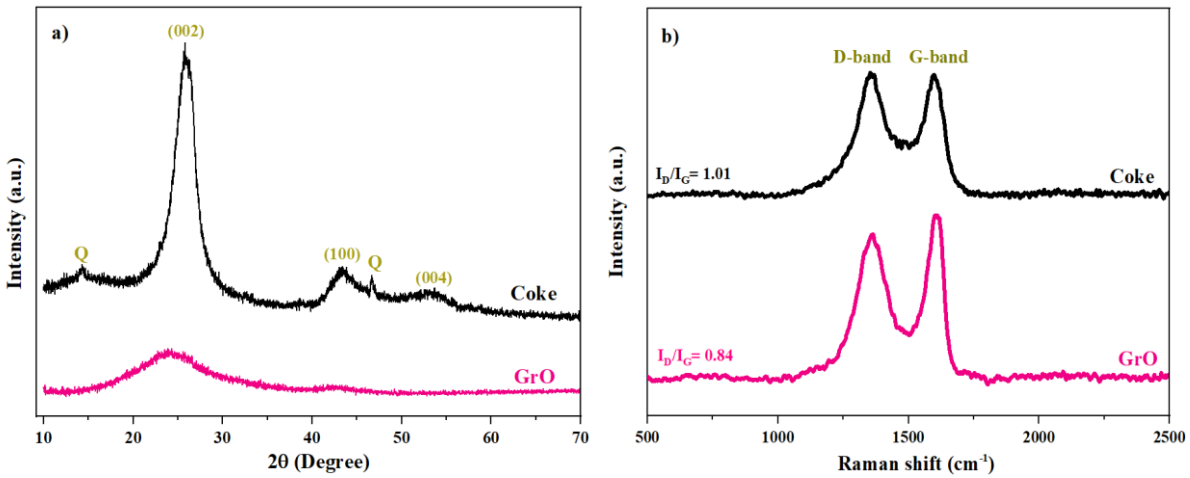

Fig.1 a) X-ray diffraction pattern b) Raman profile of coke and as-synthesized graphite oxide structure

The X-ray diffraction profile of coke, as well as the oxidized multilayer graphene structure obtained via Improved Hummers' method, is presented in Fig. 1a. The sharp and intense peak due to the preformed graphitic plane (002) centered on 2θ = 26º is a clear indication of the higher crystalline nature of carbochemical coke. After the acidic oxidation, a broadened and less intense peak is observed at 23.96º confirming the formation of an amorphous structure of graphite oxide. The (100) and (004) peaks due to the turbostratic carbon appearing at 2θ = 43.12º and 54.15º [34], is significantly weakened in synthesized GrO compared to the precursor. The reduction in the intensity of graphitic planes of GrO indicates the production of more corrugation and defects in the structure along with a less-ordered stacking direction [35]. The peaks found at 2θ = 14º and 44º, validate the existence of additional quartz-like structure in coke [36], [37]. These peaks had completely disappeared after the Hummers' treatment suggesting its demineralization along with exfoliation of graphitic domains. The interlayer spacing of coke and GrO from the characteristic (002) peak is found to be 0.342 nm and 0.370

nm respectively. This increase in interlayer spacing can be attributed to the inclusion of various functional groups in the graphitic plane due to the oxidation process.

The structural modifications of the samples are further investigated by performing Raman analysis. Both coke and GrO are characterized by defect band (D band) owing to the sp^3 carbon atoms or the structural edge defects on the graphene planes and graphitic band (G band) corresponds to the in-plane vibrations of the sp^2 carbon atoms [38] (Fig. 1b). The Raman spectra of coke display the presence of a predominant D-band at 1359 cm^{-1} with an intensity comparable to that of G-band centered at 1599 cm^{-1}. On the other hand, G-band became prominent in Raman spectra of GrO, and both G-band and D-band were blue-shifted to 1610 cm^{-1} and 1361 cm^{-1}, respectively. This shifting can be attributed to the charging of graphite layers due to the intercalants introduced via oxidation[39]. The I_D/I_G ratio measures the specific value of sp^3 atoms present in the disordered graphitic layer to that of sp^2 atoms in the graphitic layer [38]. The GrO shows a lower I_D/I_G ratio (0.84) compared to precursor coke (1.01) despite the increase in the oxygen functional groups. This is because the emergence of graphitic clusters outweighs the increasing amount of defects or the oxygen groups are attached to the edges of GrO and hence caused the minimal effect of defects onto the basal plane[40].

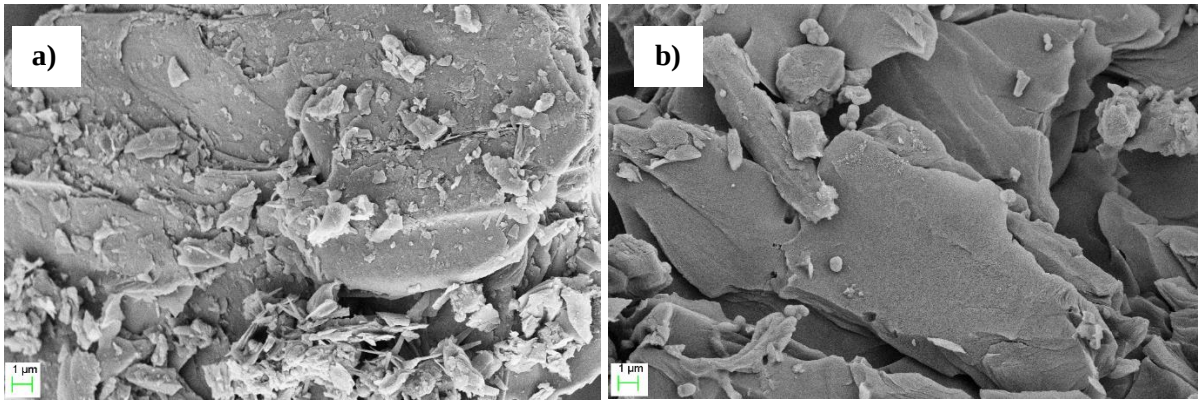

Fig. 2 SEM images of a) coke b) as-synthesized graphite oxide structure

The surface morphology of samples obtained using Scanning Electron microscopy (SEM) is presented in Fig. 2. The prepared graphite oxide exhibits a multilayer-like structure. The higher thickness of GrO sheets is owing to the introduction of oxygen-containing functional groups. The angular tensions experienced by the bonds of the carbon atoms during the synthesis procedure and stabilization followed by it led to the wrinkles at the edges [41]. The stacking of layers due to the agglomeration of graphene layers can also be seen in the synthesized GrO structure.

5.1.2 Elemental compositional analysis of the coke-based multilayer graphene derivative

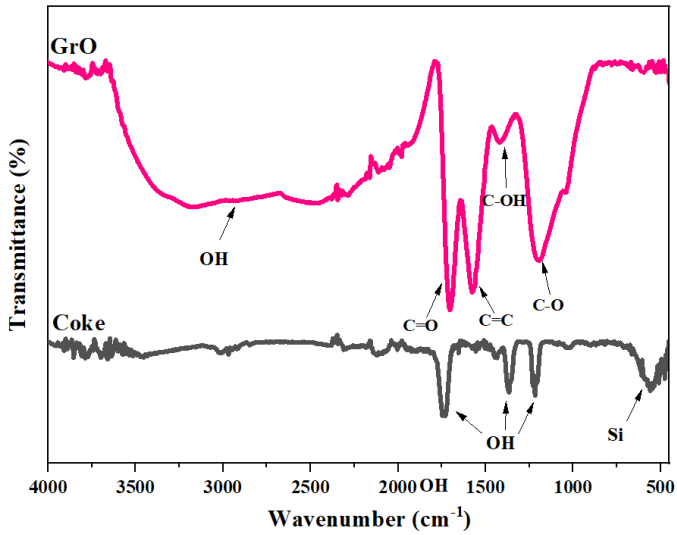

Fig. 3 FTIR analysis of coke and as-synthesized graphite oxide structure

The functional groups of the samples were identified via FTIR analysis over the spectral range 4000-500 cm^{-1}. As seen in Fig. 3, FTIR spectra of GrO possess rich oxygen-containing functional groups, resulting from the acidic oxidation. The appearance of a new peak at 1580 cm^{-1}, owing to the characteristic C=C bond of the carbon skeleton network, again confirms the emergence of graphitic clusters upon hummers' treatment. The broad peak observed at 3392 cm^{-1} originated from the stretching vibrations of O–H group. The carbonyl stretching (C=O) is confirmed by the presence of a peak at 1707 cm^{-1}. The bands associated with the C–O epoxide and C-OH group are present at 1209 cm^{-1} and 1404 cm^{-1}, respectively [40]. Also, the peaks due to silicate minerals completely disappeared in the GrO spectrum after Hummers' treatment, signifying the successful demineralization as well.

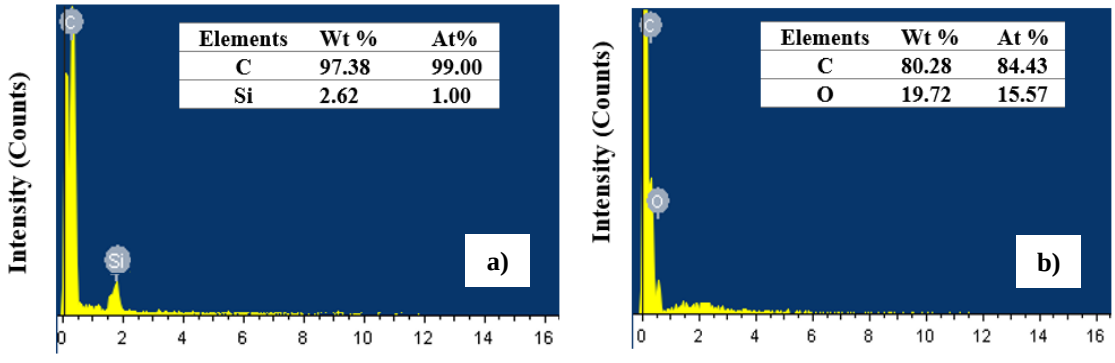

Fig. 4 EDX spectra of a) coke b) as-synthesized graphite oxide structure

The elemental analysis by Energy Dispersive X-ray spectroscopy (EDX) of GrO along with virgin coke is presented in Fig. 4. The EDX data of coke reveals that it contains Carbon (99 At%) and silicates (1 At%) as major elements. Wherein, the GrO has an increased level of oxygen functionalities because of the strong oxidizing agents involved in Hummers' method.

It is observed that the samples mainly consist of Carbon (84.43 At%) and Oxygen (15.57 At%). The compositional analysis by FTIR further corroborates this finding.

5.1.3 Optical analysis of the coke-based multilayer graphene derivative

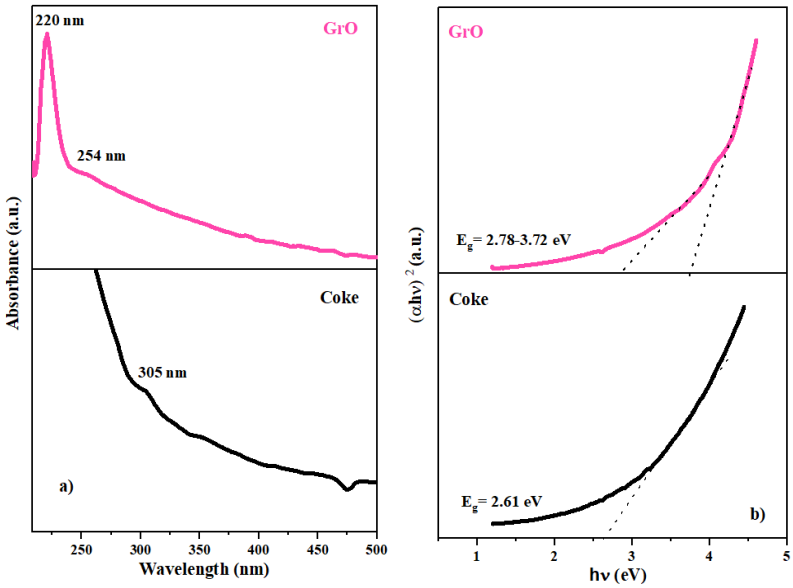

Fig. 5 a) UV-Vis absorption spectra b) Tauc plot of coke and as-synthesized graphite oxide structure

The UV–Vis absorption spectra of coke and GrO are depicted in Fig. 5a. An obvious peak at 220 nm due to π- π* transitions of the C=C bonds is because of the development of oxidized graphite structures. A shoulder peak around 254 nm and 300 nm is owing to n-π* transitions of C=O bonds [42]. Based on this absorption data, the bandgap was obtained from a Tauc plot with linear extrapolation. The calculated bandgap of coke and GrO were in the range of 2.61 eV and 2.78–3.72 eV, respectively. It is the amorphous nature and the non-uniform oxidation of the graphene structures that contribute to the wide range of bandgap for GrO[43].

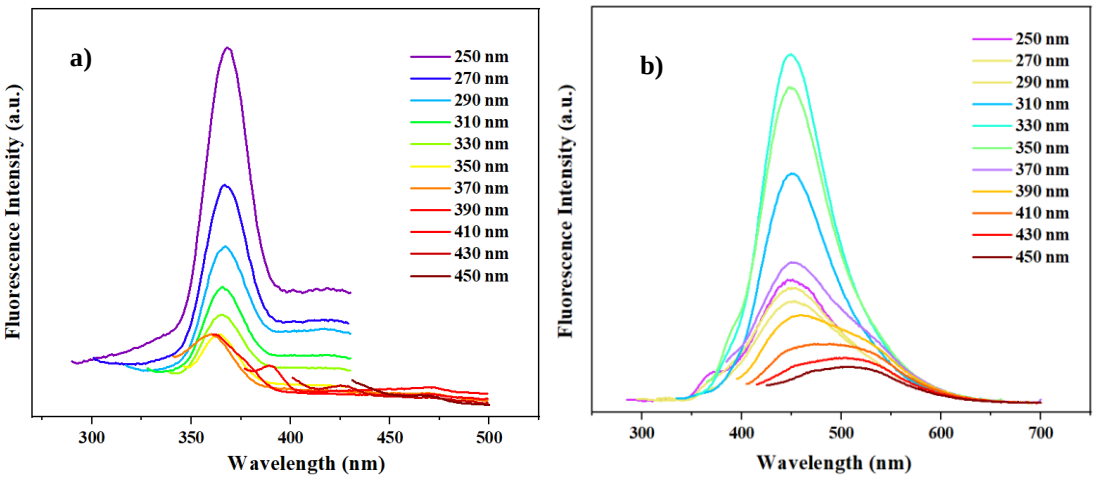

Fig. 6 Fluorescence spectra of a) coke b) as-synthesized graphite oxide structure

The fluorescence spectra of coke and GrO are obtained at varying excitation wavelengths from

250 to 450 nm with a step interval of 20 nm (Fig. 6). The precursor coke shows an excitation-independent fluorescence emission centered at 370 nm for the excitation ranging from 250 to 370 nm and followed by diminished red-shifted emission till 450 nm. The synthesized GrO shows evidence of excitation independent fluorescence until an excitation wavelength of 370 nm and dependent fluorescence beyond 390 nm. The excitation independent behavior is a coalesced effect of surface state and morphology of the sample [44]. The wavelength of emission is determined by the energy band gap which is formed by clusters of sp^2 matrix and from different emission sites [45]. It is suggested that the increase in the size of clusters lead to the decrement of the energy gap between the highest occupied molecular orbital (HOMO) and lowest unoccupied molecular orbital (LUMO)[46]. GrO exhibits an excitation-independent dual emission as evident in Fig. 6b. The observed peak in the UV region is the contribution of small sp^2 clusters having an energy band gap of 3.72 eV and the peak centered on 450 nm originates from a small energy band gap (2.78 eV) of large clusters. This dual emission substantiates the wide range of bandgap for graphite oxide aroused from the different oxidation degree induced via Hummers' treatment. In addition to the excitation independent luminescence, GrO portrays emission-excitation dependency. From the excitation wavelength 390-450 nm, the emission spectra display a redshift with lessening fluorescence intensity. The broad emission peak in the visible region for different wavelengths originates from surface states that include defects and numerous chromophores or fluorophores. The –COOH, –OH, and C–O–C in the graphene sheets contribute to its wavelength-dependent emission [46].

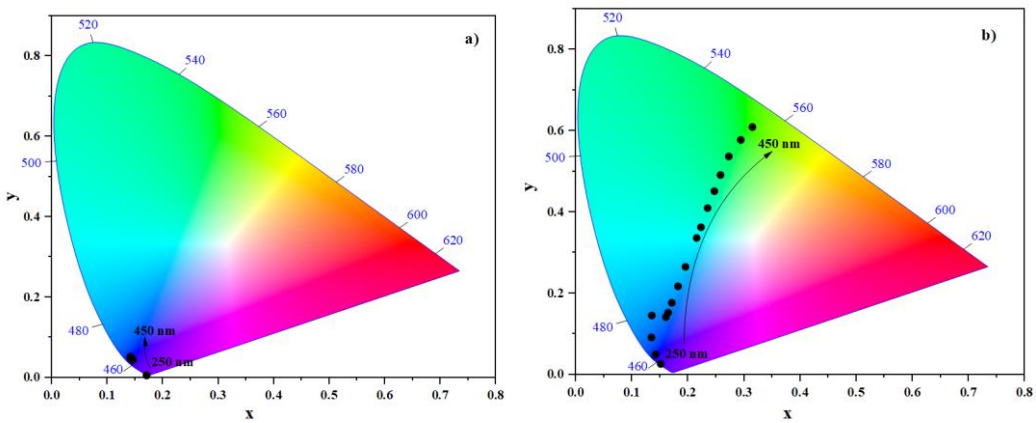

Fig. 7 CIE chromaticity diagram of a) coke b) as-synthesized graphite oxide structure

The CIE (Commission Internationale de l'Elcairage) chromaticity diagrams of the samples are drawn from the data of the PL spectra. As seen in Fig.7, the emission of precursor coke was limited in the blue region, Wherein, a variety of emission colors ranging from blue to green-yellow are noticed for GrO for increasing excitation wavelengths. Thus, the oxidation of coke-based graphite facilitates the fabrication of multi-emissive multilayer graphene

derivatives, owning the potential for various fluorescence applications.

5.1.4 Electrochemical analysis of the coke-based multilayer graphene derivative

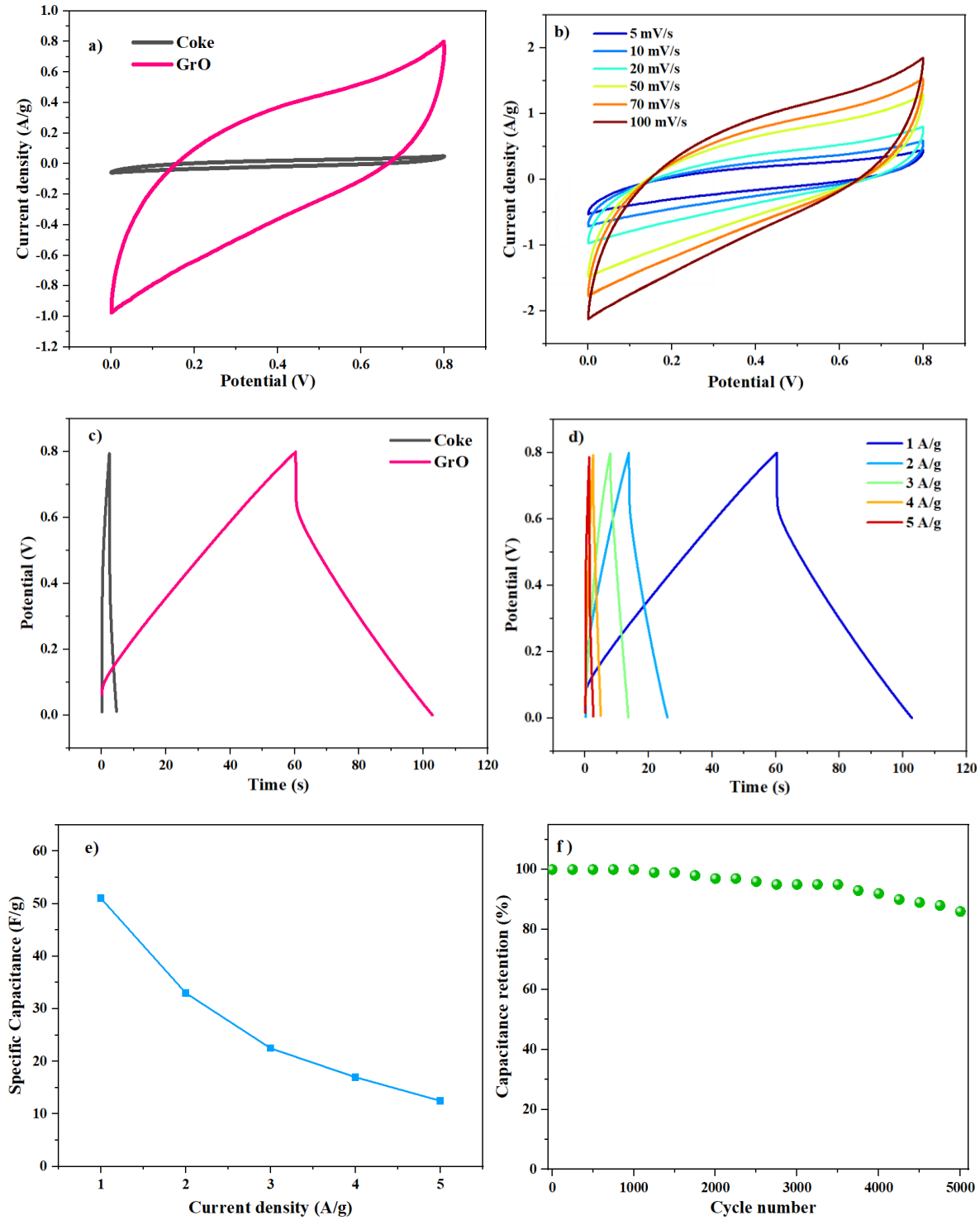

Fig.8 a) CV curves of coke and GrO at 50 mV/s b) CV curves of GrO at different scan rates (5-100 mV/s) c) GCD curves of coke and GrO at 1A/g d) GCD curves of GrO for different current densities (1-5 A/g) e) The specific capacitance obtained for GrO at different current densities f) Capacitance retention of GrO electrode as a function of GCD cycle number under a current density of 15 A/g

The electrochemical properties of coke and as-synthesized GrO are studied using cyclic

voltammetry (CV) in a 3-electrode cell and the corresponding CV curves obtained at 50 mV/s are shown in Fig. 8a. The integrated area of the CV curve for GrO modified electrode was higher in comparison to precursor coke, which is an indication of the superior electrochemical behavior resulting from their abundant active sites and thus favoring the quick charge propagation capability. As seen in Fig. 8b, CV curves for various scan rates exhibited a quasi-rectangular CV curve which is the characteristic of an electric double-layer capacitor. The palpable bumps correspond to the pseudo-capacitance originating from the redox reactions of the oxygen functionalities introduced into the graphene basal planes[47], [48]. The mechanism involved in this faradic reaction can be explained in terms of electrochemical reactions at the electrode-electrolyte interfaces e.g. >C–OH⇔>C=O+H^++e^- [48]. The mirror image of the CV curves at different scan rates indicates the high current response of the sample. For the scan from 5 mV/s to 100 mV/s, the area under the CV curve increases but the quasi-rectangular shape got distorted. The fast transport of ions at higher scan rates disturbs the equilibrium necessary for a symmetric CV curve. The increase in area under the CV curve with the scan rate depicts its good rate capability. The best specific capacitance value was obtained from CV curves reaching up to 45 F/g at 5 mV/s.

The electrochemical behavior of coke and GrO modified electrodes are further evaluated using galvanostatic charge-discharge (GCD) tests. As shown in Fig. 8c GrO exhibited a longer discharge time than that of coke, thus again confirming its superior capacitive behavior. The GCD curves obtained for various current densities are displayed in Fig. 8d. The quasi-triangular and nearly symmetrical shapes of the plot reveal excellent reversibility of EDLC performance. Non-linearity observed in the potential–time curve is due to the storage mechanism of charge via both double-layer and pseudo-capacitance mechanisms[49]. Epoxy and alkyl functional groups on the surface of graphene promote quick faradaic reactions which result in deviation of the ideal linear shape of the V-t curve. From the GCD curve, a specific capacitance of 51 F/g was obtained at 1 A/g current density (Fig. 8e). To evaluate the life cycle and stability of GrO, continuous 5000 charge-discharge cycles were performed at a current density of 15 A/g. The initial specific capacitance of GrO was retained ~85% even after 5000 cycles suggesting its noteworthy cycle durability and electrochemical stability (Fig. 8f).

5.1.5 Conclusion

An eco-friendly and facile synthesis route is employed for the preparation of a multilayer graphene derivative using coke as the precursor. The structural, morphological, and elemental analysis confirms the formation of a defected and oxygenated graphitic structure. The inherent

defect states own by coke are also of high significance as it performs the role of various photoluminescence emission centers. The sp^2 domains and different surface defects promote excitation independent and dependent luminescence substantiating the distinct multi-emission property of GrO. Hence, it serves the purpose of an excellent luminescent that consists of dynamic emissions centers. It is also found from the electrochemical analysis that coke-derived GrO exhibited remarkable energy storage characteristics as well. Thus, the most advantageous carbogenic core and defect densities endorse GrO as a potent contender that could be further manipulated and employed for several optical and electrochemical applications.

5.2 HETEROATOM ENGINEERED COKE-BASED MULTILAYER GRAPHENE DERIVATIVES: APPLICATIONS IN FLUORESCENCE BIOIMAGING OF MELANOMA CELLS AND ELECTROCHEMICAL DETECTION OF OXYTOCIN

In the current study, heteroatom-doped samples namely, phosphorus-doped (PG_H), nitrogen-doped (NG_H), and co-doped (NPG_H) graphene structures possessing distinct optical and electrochemical behaviors are synthesized utilizing coke-based multilayer graphene derivative via one-pot hydrothermal method. The potential applications of as-synthesized heteroatom doped multilayer graphene derivatives in fluorescence bioimaging and electrochemical sensing have also been discoursed.

5.2.1 Structural and morphological analysis of the heteroatom doped multilayer graphene derivatives

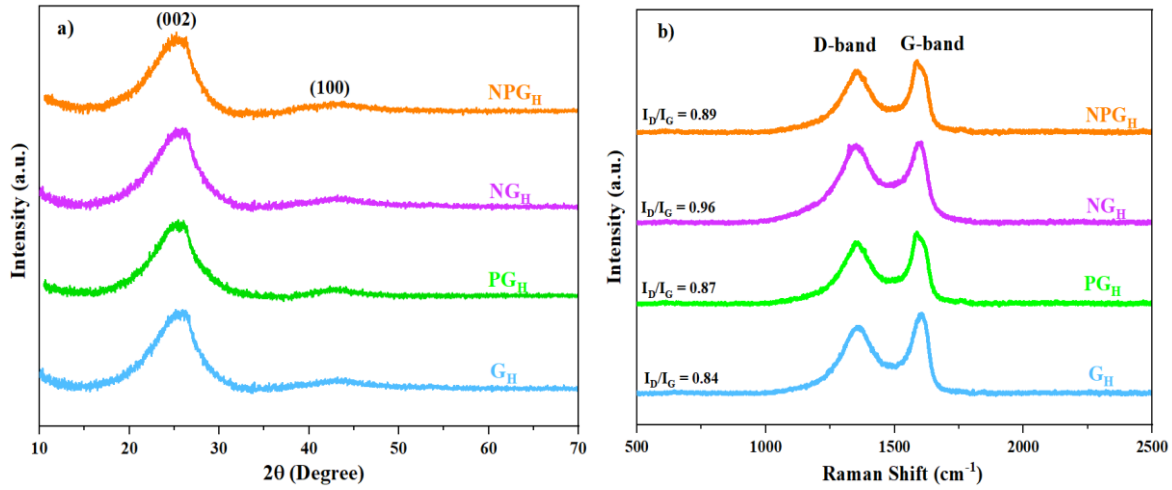

Fig. 9 a) X-ray diffraction pattern b) Raman profile of doped (PG_H, NG_H, NPG_H) and undoped (G_H) multilayer graphene derivatives

To comprehend the variation in crystal structure of coke-based multilayer graphene

system upon doping of heteroatoms, an XRD study is performed and the results are shown in Fig. 9a. The peak attributing to the characteristic graphitic crystal plane (002) is observed at approximately 25º in XRD patterns of all the samples. Whereas the peak centered at 41° having lower intensity is ascribed to the reflection of (100) plane [50]. The XRD patterns of doped samples (PG_H, NG_H, and NPG_H) are similar to that of undoped G_H, signifying that the doping treatment exerts negligible impact on the crystalline structure of graphene system. The interlayer spacing of G_H, PG_H, NG_H, and NPG_H calculated from (002) diffraction peak is 0.351 nm, 0.354 nm, 0.344 nm, and 0.349 nm, respectively. The increased interlayer spacing or the shifting of diffraction peak to lower 2θ degree observed in PG_H is due to the introduction of oxygen functional groups from the phosphorus precursor, H_3PO_4.

The structural modifications and defects induced in the coke-based multilayer graphene system via doping of heteroatoms are studied using Raman spectroscopy. The obtained spectra are shown in Fig. 9b. The Raman features of as-synthesized multilayer graphene derivatives are the so-called D-band and G-band, which are found at ~ 1350 cm^{-1} and 1580 cm^{-1}, respectively. The prevailing D-band is associated with the defects or disorders in the system, and the existence of G-band is recognized in the E_{2g} vibrations of the sp^2 carbon atoms [38]. The peak positions of G-bands in doped samples are witnessed to have a blue shift in comparison to that of pristine G_H. The cause for this shift is aroused from the electron doping effect and the defects associated with the lattice deformation in C-C bond. These modifications in electronic properties and bond configurations strongly contribute to the stiffening of phonons in G-band [51]. The defect densities in the doped samples are quantified using the parameter I_D/I_G, i.e., relative intensity ratio of D-band to G-band. The I_D/I_G values of G_H, PG_H, NG_H, and NPG_H are found to be 0.84, 0.87, 0.96, and 0.89, respectively. The increased I_D/I_G values of doped samples indicate the excess defects in the graphene framework adjudged to the replacement of C atoms by N and P and hence confirmed the successful doping. The abundant defects on the surface of graphene could significantly improve its optical, electrical, and chemical properties. The induced “defect sites” can impact the fluorescence emission by creating additional energy levels for new electron transition pathways [52]. Moreover, these defects may also serve the purpose of reactive active sites beneficial for an enhanced electrocatalytic activity [53].

The N_2 adsorption-desorption isotherms and the corresponding pore-size distribution curves for all samples are shown in Fig. 10. It was found that the N_2 adsorption-desorption isotherm profiles were almost similar, and exhibited the shape of type IV, as prescribed by IUPAC[54]. Along with the increase in relative pressure, steady increases in adsorption

capacity were caused by the adsorptions of nitrogen molecules on mesopores. Thus, the hysteresis loop suggests mesoporosity of these materials with pore condensation at high pressure. This has been further supported by the pore size pattern (shown in Fig. 10(b)). The BET surface area is determined to be 4.36 m^2/g, 8.10 m^2/g, 1.49 m^2/g, and 30.2 m^2/g for G_H, PG_H, NG_H, and NPG_H, respectively. This indicates that the co-doping of heteroatom is helpful for enhancing the surface area along with hierarchical mesoporous structures which are much beneficial for the electrocatalytic performance as it can provide a large accessible area and efficient electron/ion-transport channels.

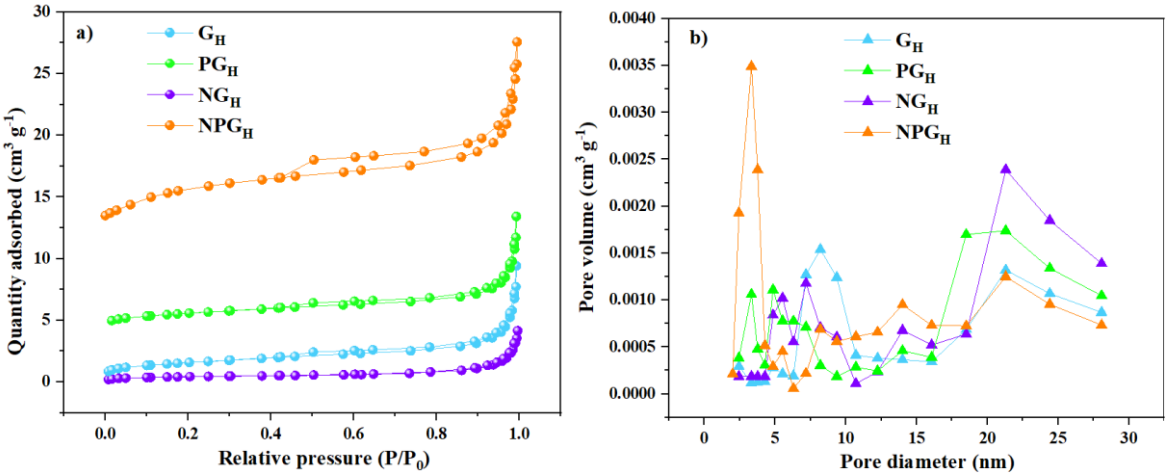

Fig. 10 a) N_2 adsorption-desorption isotherms b) pore size distribution of doped (PG_H, NG_H, NPG_H) and undoped (G_H) multilayer graphene derivatives

The morphologies of heteroatom doped samples are characterized using scanning electron microscopy (SEM). The microstructure analysis in Fig. 11 displayed a compact, stacked, and layered morphology of the graphene structure. The exfoliated graphene layers are coupled to alleviate the thermodynamic instability due to van der Waals's force of attraction between the sheets [55]. The presence of crumples and wrinkles in the exfoliated structure can be ascribed to the deformation of the graphene sheets that happened while the folding and restacking processes [56]. Upon doping of phosphorus, the agglomeration of graphene sheets is suppressed and therefore considerably expanded layers are observed in SEM image of PG_H (Fig. 11b). The SEM results show that the nitrogen-doped multilayer graphene derivative owns a higher degree of restacking of graphene layers as a result of the reduction effect induced by the N-precursor, ethylenediamine (Fig. 11c). However, NPG_H possesses a more crinkled structure with more open edges due to the effect of nitrogen and phosphorus co-doping (Fig. 11d). These surface modifications along with the presence of co-dopants provide a high contact probability of active sites and therefore can potentially augment the electrochemical catalysis and sensitivity.

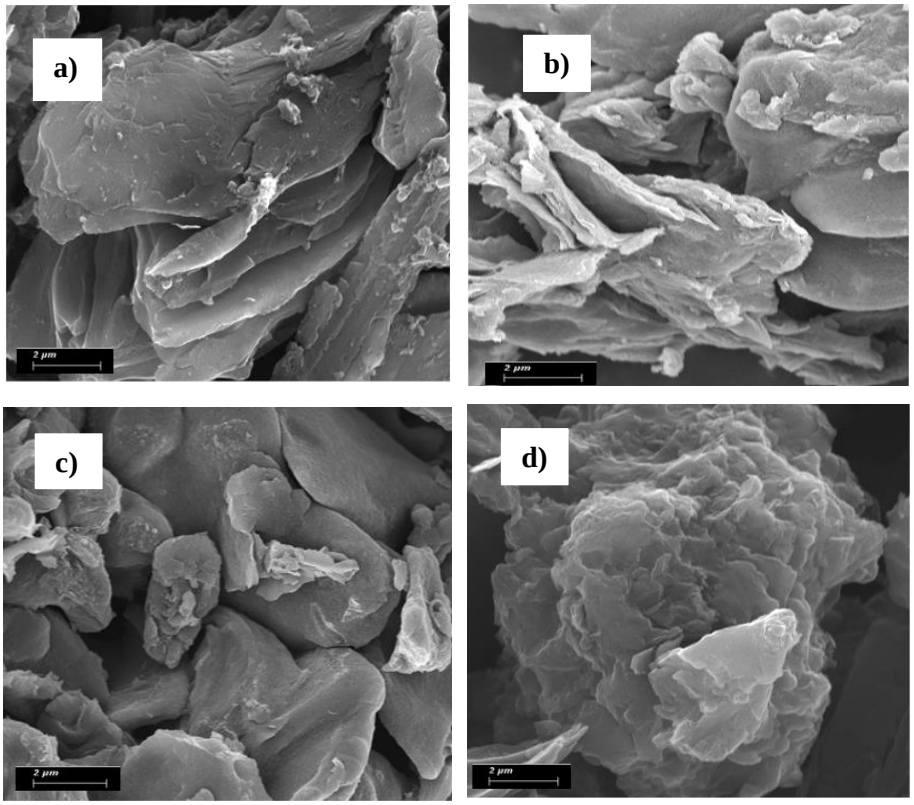

Fig. 11 SEM images of a) Undoped (G_H) b) phosphorus-doped (PG_H) c) nitrogen-doped (NG_H) d) Co-doped (NPG_H) multilayer graphene derivatives

5.2.2 Elemental compositional analysis of the heteroatom doped multilayer graphene derivatives

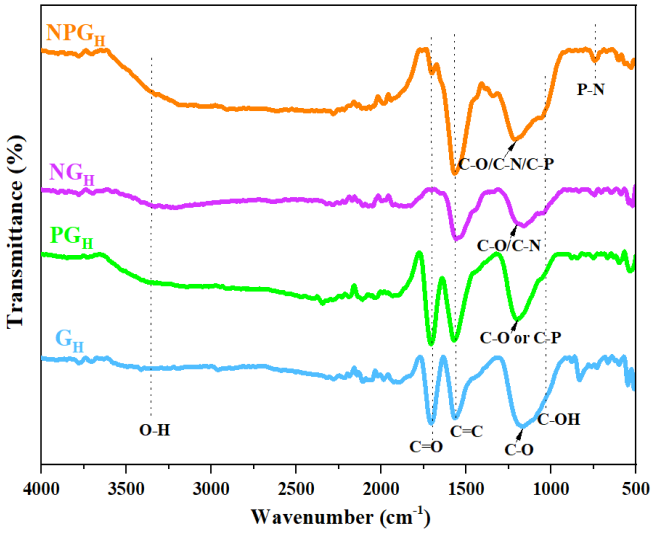

Fig 12. FTIR Spectra of doped (PG_H, NG_H, NPG_H) and undoped (G_H) multilayer graphene derivatives

The chemical structures of all the samples are examined by employing FTIR spectroscopy and the results are depicted in Fig.12. The characteristic absorption peaks corresponding to oxygen functionalities and N/P heteroatoms are observed in the FTIR spectra

of G_H, PG_H, NG_H, and NPG_H. The broad absorption peak around 3400 cm^{-1} corresponds to the vibration of -OH groups or the trapped water molecules. Peaks at 1710, 1572, 1180, and 1050 cm^{-1} are ascribed to the stretching vibrations of C=O bond, skeleton vibrations of graphene domains (C=C), stretching of C-O bond, and presence of C-OH stretching, respectively [40]. It is obvious that the intensity of bands due to the oxygen functionalities (C-O, C=O, C-OH) are declined in NG_H and NPG_H, which are caused by the fact that the samples are deoxygenated due to the reduction effect of nitrogen precursor, ethylenediamine. The wide peak at 1175 cm^{-1} may be assigned to the integrated vibrations of C-O, C-P, or C-N bond [57]. Interestingly, along with the characteristic vibrations of C-P, C-N, and P-O in spectrum of NPG_H an additional peak marked at 730 cm^{-1} indicates the occurrence of N-P bond [58]. Hence, the FTIR spectra confirm the presence of heteroatoms, signifying the successful doping of nitrogen and phosphorus in the graphene network.

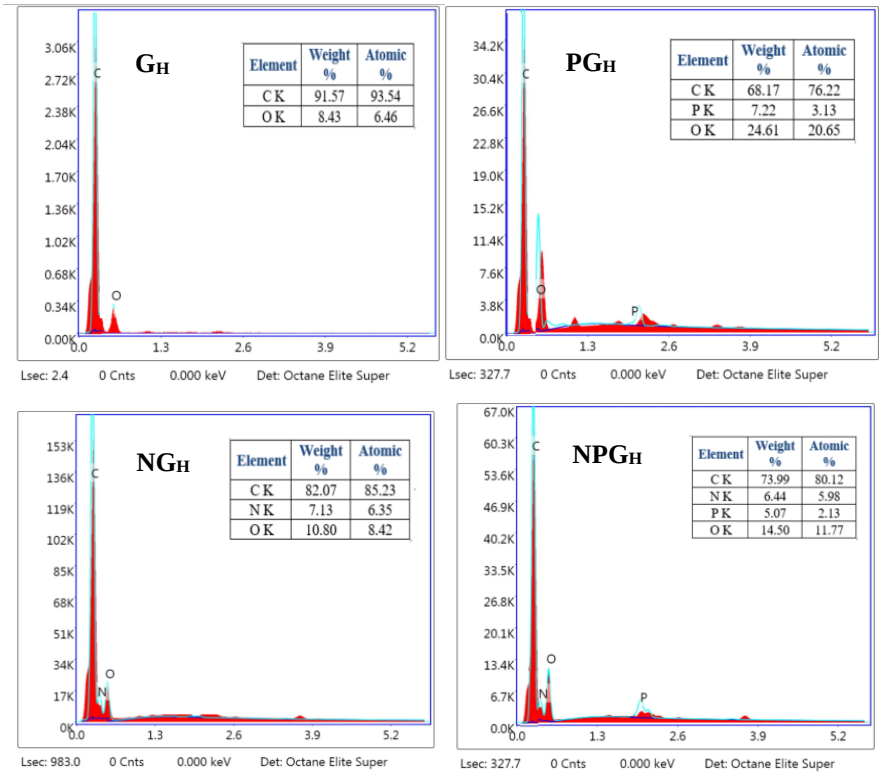
GH
Element | Weight % | Atomic %
C K | 91.57 | 93.54
O K | 8.43 | 6.46
PGH
Element | Weight % | Atomic %
C K | 68.17 | 76.22
P K | 7.22 | 3.13
O K | 24.61 | 20.65
NGH
Element | Weight % | Atomic %
C K | 82.07 | 85.23
N K | 7.13 | 6.35
O K | 10.80 | 8.42
NPGH
Element | Weight % | Atomic %
C K | 73.99 | 80.12
N K | 6.44 | 5.98
P K | 5.07 | 2.13
O K | 14.50 | 11.77
Lsec: 2.4 0 Cnts 0.000 keV Det: Octane Elite Super
Lsec: 327.7 0 Cnts 0.000 keV Det: Octane Elite Super
Lsec: 983.0 0 Cnts 0.000 keV Det: Octane Elite Super
Lsec: 327.7 0 Cnts 0.000 keV Det: Octane Elite Super

Fig. 13 Elemental composition analysis of a) undoped (G_H) b) phosphorus-doped (PG_H) c) nitrogen-doped (NG_H) d) co-doped (NPG_H) multilayer graphene derivatives

The elemental compositions of as-prepared heteroatom doped graphene structures are identified using energy-dispersive x-ray spectroscopy (EDX) measurements (Fig. 13). Only carbon and oxygen were detected on the surface of G_H; wherein, the presence of heteroatoms (N/P) on the surface of doped samples (PG_H, NG_H, NPG_H) was confirmed. Besides, the non-appearance of any other foreign elements demonstrates the purity of all samples.

5.2.3 Surface chemistry characteristics of the heteroatom doped multilayer graphene derivatives

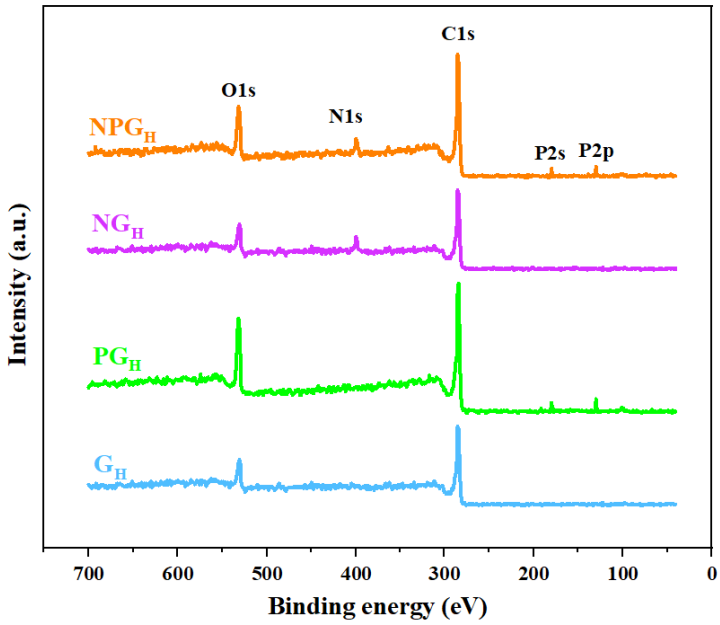

Fig. 14 XPS survey spectrum of doped (PG_H, NG_H, NPG_H) and undoped (G_H) multilayer graphene derivatives

In order to further analyze the type of heteroatoms species, XPS measurements were performed, and the results are shown in Fig. 14. The overlaid survey spectrum revealed the presence of phosphorus and nitrogen atoms in NPG_H (N: 3.92 At %, P: 1.73 At %), PG_H (P: 2.89 At %), and NG_H (N: 5.92 At %). In contrast, G_H comprises only carbon and oxygen atoms with an atomic concentration of 90.68 At % and 9.32 At %, respectively. These results indicate that the heteroatoms are doped into graphene structure and thus, corroborate the findings from EDX, FTIR, and Raman analysis.

The nature of chemical bonds in each heteroatom doped graphene sample is gained through the analysis of the core level characteristic peaks. The high-resolution spectra and deconvoluted peaks (bonding components) in the region of C1s and O1s for doped and undoped samples are shown in Fig. 15. The peak corresponding to sp^2 or sp^3, carbon at 284.7 eV is the characteristic feature of the C1s region (Fig. 15a). The component at 285.5 ± 0.1 eV is assigned to C atoms bonded to the heteroatoms (N/P)[59], [60]. The presence of C–P and C-N peaks confirms the successful doping of P and N atoms into the carbon lattice of graphene sheets. The component at 286.1 ± 0.1 eV is assigned to C atoms directly bonded to the oxygen atoms in hydroxyl or epoxy configurations. The smaller components at 287.5 ± 0.3 eV and 288. 9 ± 0.3 eV are related to carbonyl (C=O) and carboxyl groups (-O-C=O) [61]. Deconvolution of O1s spectra (part b of Fig. 15) produces 4 main peaks around 530.5 ± 0.2 eV, 531.8 ± 0.2 eV,

533.1 ± 0.3 eV, and 534 ± 0.3 eV corresponding to C=O (of carbonyl group), C-O (of epoxy group), C-OH (of hyroxyl group) and -O-C=O (of carboxyl group) respectively [62]. Wherein, the doped samples exhibited 532.5 ± 0.1 eV and 533.7 ± 0.2 eV corresponding to nitric oxide (NOx) and P-O-P group that have resulted from the intercalation of the heteroatoms [63], [64].

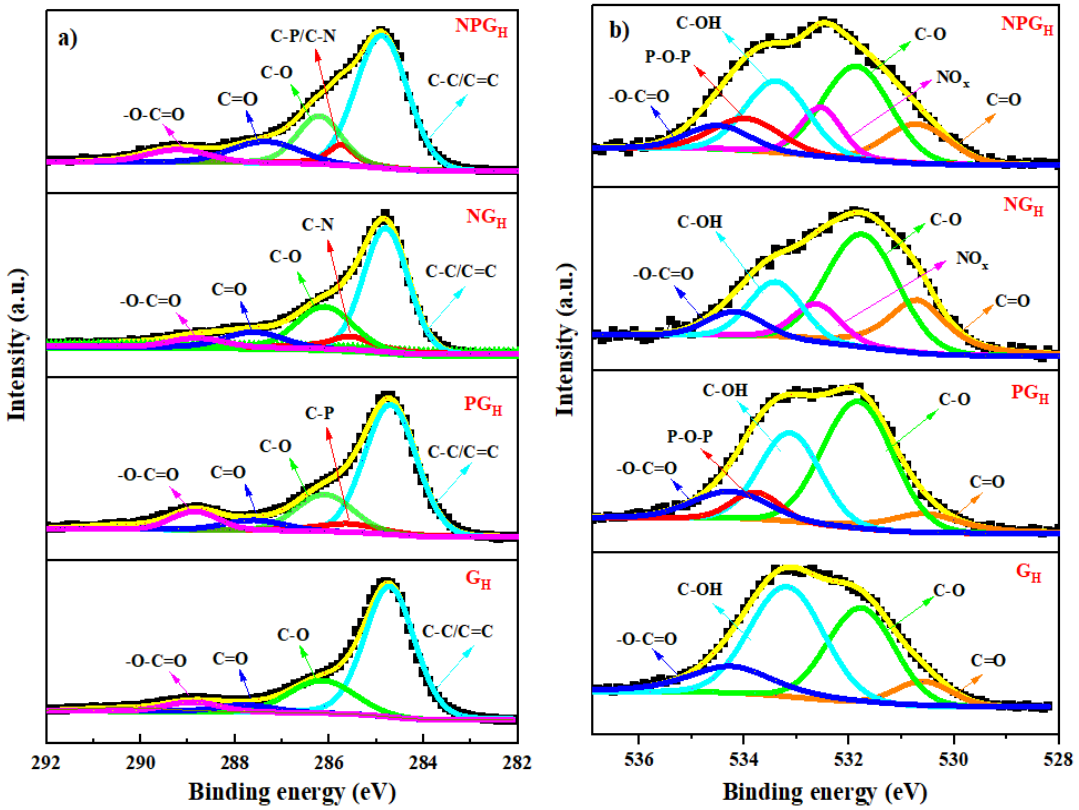

Fig. 15 High-resolution XPS deconvoluted spectra of a) C1s b) O1s for doped (PG_H, NG_H, NPG_H) and undoped (G_H) multilayer graphene derivatives

The atomic component fraction of each surface functional group has been calculated from the area of the deconvoluted C1s and O1s peaks of the respective samples. Fig. 16a presents the variation in the content of graphitic carbon (area of C-C/C=C peak) and oxygenated carbon (sum of CO + C=O + -O-C=O peaks) in all four samples. It is worth mentioning that the highest fraction of graphitic carbon (80%) is detected in the undoped sample (G_H), followed by NG_H (72%), NPG_H (67%), and PG_H (63%). The replacement of carbon atoms by heteroatoms (N/P) and the introduction of oxygen functionalities by the phosphorus dopant (H_3PO_4-Phosphoric acid) have significantly reduced the content of graphitic carbon. Moreover, NG_H comprises the least amount of oxygenated carbon out of all four samples due to its reducing effect. The XPS spectral analyses of the O1s spectra revealed that the as-synthesized samples possess a carbon network enriched with different oxygen functionalities and the atomic composition of each of those oxygen moieties is displayed in Fig. 16b. It should be noted that the contribution of C-O and C-OH is more substantial

compared to C=O and O-C=O. For heteroatom modified samples, in parallel with the main oxygen components, there is also observed a small contribution of NOx and P-O-P. Hence, it is evident from the graphs that the surface atomic content of the doped and undoped samples relies on the nature of the chemical modification involved.

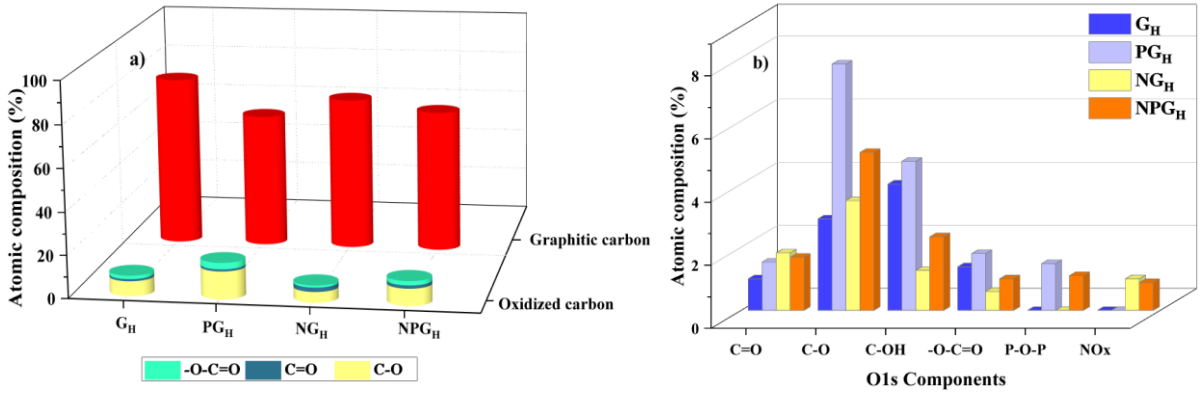

Fig. 16 (a,b) Surface atomic composition of different functionalities obtained from C1s and O1s peaks of doped (PG_H, NG_H, NPG_H) and undoped (G_H) multilayer graphene derivatives

The N1s and P1s spectrum are used to elucidate the phosphorus and nitrogen dopant configurations in the graphene lattice. The deconvolution of the high-resolution spectra of P2p shown in Fig. 17a revealed the presence of core-level peaks at binding energies of 129.5 ± 0.1 eV and 130.4 eV, for elemental phosphorus and graphitic phosphorus, respectively. The peak observed at 134.7 ± 0.1 eV is due to the P-O of the metaphosphate group [65], [66]. Compared with NG_H, an additional peak at a binding energy of 132.8 eV is observed in NPG_H, attributed to the N-P bond aroused from the co-doping of heteroatoms [67]. To further reflect on the environment of the nitrogen atom in mono-doped and co-doped graphene systems, the deconvolution analysis of the core level peaks of N1s spectra is carried out as shown in Fig. 17b. The deconvoluted components observed at binding energies of 398.7 eV and 399.9 ± 0.1 eV, suggest the pyridinic N and graphitic/pyrrolic N doping configurations, respectively. The contribution from N-oxide is witnessed at the binding energy of 401.8 eV [68]. Also, a small peak is observed at 401.1 eV in N1s spectra of NPG_H, which is associated with the bonding of nitrogen with phosphorus to form N-P signatures [69]. Thus, the configuration of heteroatoms in the graphene lattice could be resolved using x-ray photoelectron spectroscopy, as the difference in binding energy is high enough to distinguish between the adsorptive or substitutional doping.

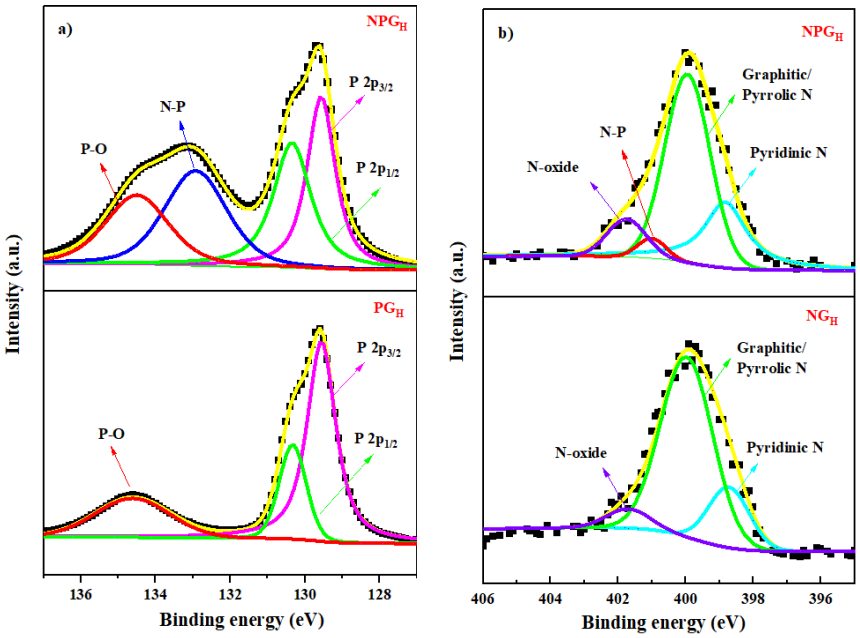

Fig. 17 High-resolution XPS deconvoluted spectra of (a) P2p (b) N1s for doped (PG_H, NG_H, NPG_H) multilayer graphene derivatives

5.2.4 Optical analysis of the heteroatom doped multilayer graphene derivatives

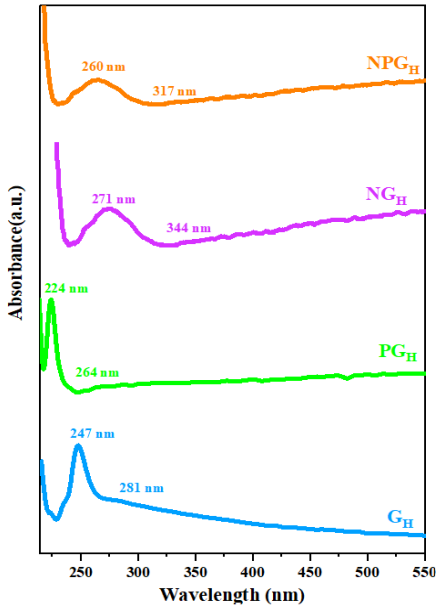

Fig. 18 UV-Vis absorption spectra of doped (PG_H, NG_H, NPG_H) and undoped (G_H) multilayer graphene derivatives

The optical properties of heteroatom doped samples are studied in detail using UV-vis absorption spectra and fluorescence spectra. Fig.18 shows the corresponding UV-Vis absorption spectra of doped and undoped samples. The absorption peak corresponding to the π- π* transitions of C=C bond are observed at 247 nm, 224 nm, 271 nm, and 260 nm, for G_H, PG_H, NG_H, and NPGH, respectively. Wherein, the absorption peaks witnessed at 281 nm, 264 nm, 344 nm, and 317 nm are the absorption shoulder peaks due to the n-π* transitions of the

C=O. The C=C bonds arouse from the sp^2 conjugated carbon core of the heteroatom doped graphene derivatives and the C=O bonds are due to the oxygen-containing functional groups existing at the graphene edges [42].

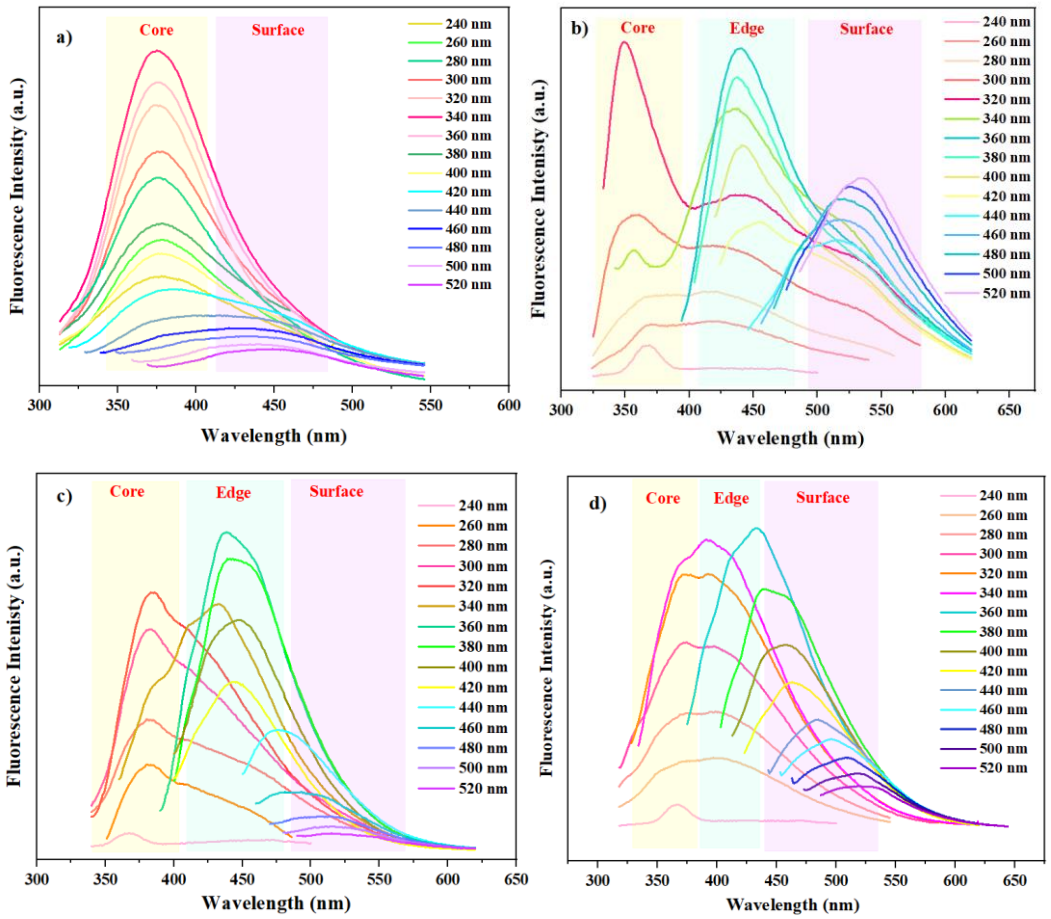

Fig. 19 Fluorescence spectra of a) undoped (G_H) b) phosphorus-doped (PG_H) c) nitrogen-doped (NG_H) d) co-doped (NPG_H) multilayer graphene derivatives

To unravel the fluorescence emission of the heteroatom doped graphene system, the emission spectra were obtained for the excitation wavelengths ranging from 240 to 520 nm in intervals of 20 nm. As seen in Fig. 19, the intensity of fluorescence emission initially increases and then decreases with the increment in excitation wavelength. This effect has been observed in the nanostructured materials owing to several factors such as heterogeneous surface states, electronic properties, and varying morphology[70]. For relatively lower wavelengths, the electrons are pumped into higher energy states of the conduction band which is distant from the radiative electronic states. This significantly drops the photon emission and hence, the intensity of fluorescence emission is found to increase with the excitations in shorter wavelength regions. Wherein, for longer wavelengths regions, fewer electrons are pumped into the conduction band and thereby the emission spectra show a reduction in the fluorescence intensity with an increase in excitation wavelength[71]. Furthermore, the strong emission

bands demonstrated in the fluorescence spectra signify the existence of different emissive centers. The spectra of undoped graphene system display two characteristic bands, which can be attributed to the core state and surface state. The π-π*charge transfer transitions in the sp^2 conjugated carbon domain and the surface functional groups contribute towards these core and surface states, respectively. But, in the heteroatom-doped graphene system, along with these two characteristic bands an additional spectral band, so-called "edge states", achieved via n-π* transitions from N, P, or O groups are witnessed [72].

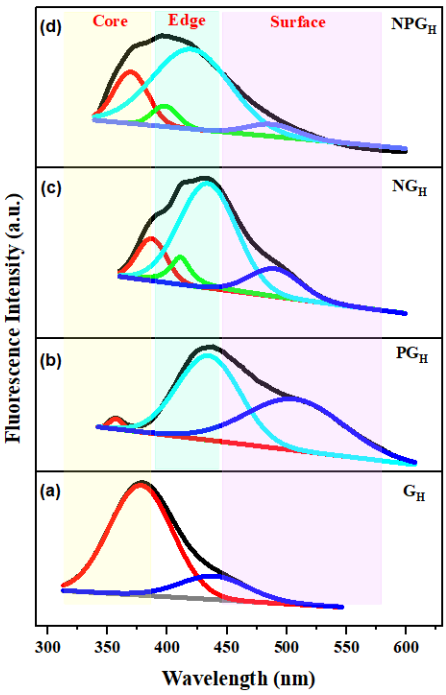

Fig. 20 Curve fitting analysis of fluorescence spectra at an excitation wavelength of 340 nm for doped (PG_H, NG_H, NPG_H) and undoped (G_H) multilayer graphene derivatives

The fluorescence spectra consisting of two or three overlapping characteristic bands can be deconvoluted into gaussian-like emission peaks, which comprise excitation-independent and excitation-dependent emission peaks. Fig. 20 shows the deconvoluted fluorescence spectra for doped (PG_H, NG_H, NPG_H) and undoped samples (G_H) measured at an excitation wavelength of 340 nm. As seen in Fig. 20 (a-d), all the samples exhibited core bands with emission peaks centered at 375 nm, 353 nm, 384 nm, and 369 nm, respectively for G_H, PG_H, NG_H, and NPG_H. Similarly, the fluorescence bands owing to the surface functional groups that are primarily excitation dependent are also spotted. Especially, in doped samples, the emissions from edge bands provide evidence for the existence of heteroatoms related to emissive centers. The fluorescence spectra of PG_H, NG_H, and NPG_H display an emission maximum at 424 nm, 440 nm, and 427 nm, respectively. Wherein, NG_H and NPG_H possess two additional edge state emissions, at 411 nm and 398 nm, respectively which are caused by the sub-band gaps within

the edge. It is also observed that the intensity of core bands declined with the introduction of heteroatoms, implying that edge bands are the most domineering emissive component in doped samples. Furthermore, the blueshift or redshift observed in the core, edge, and surface state emissions is caused by the alterations in defects or surface functional groups induced by doping of heteroatoms. Compared to G_H (375 nm), the PG_H exhibited a blueshift (353 nm), while NG_H showed a redshift (384 nm). These shifts in core band emissions can be explained in terms of the electronegativity of the dopants (P-2.19, N-3.04) relative to carbon (2.55). For higher electronegative atoms, n-electrons are strongly attracted and hence higher energy is required to excite the electrons [73]. Thus, the transition energy increases in the order of PG_H, NPG_H, and NG_H and it is in agreement with the UV-absorption spectra.

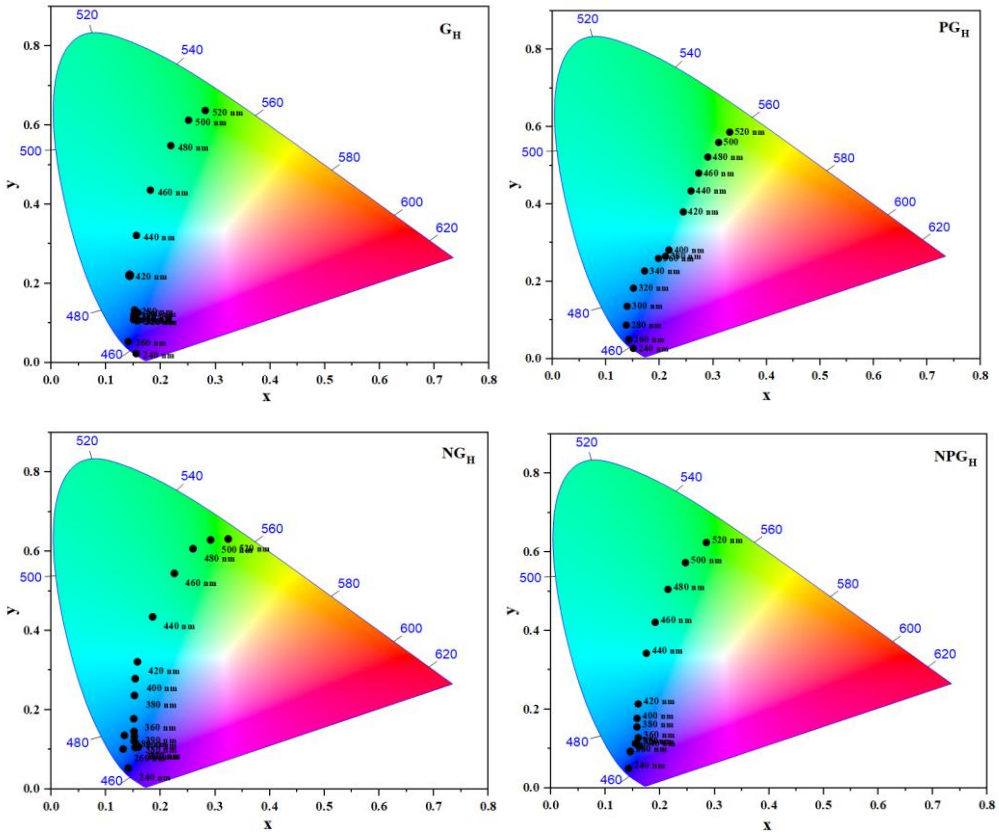

Fig. 21 CIE chromaticity diagram of doped (PG_H, NG_H, NPG_H) and undoped (G_H) multilayer graphene derivatives

The CIE (Commission Internationale de l'Elcairage) chromaticity diagrams of all the samples are drawn from the PL spectra data. As seen in Fig. 21, the emission colors ranging from blue to green-yellow are noticed for each samples for increasing excitation wavelengths, implying their potential applications in fluorescence sensing, bio-imaging, and optoelectronics.

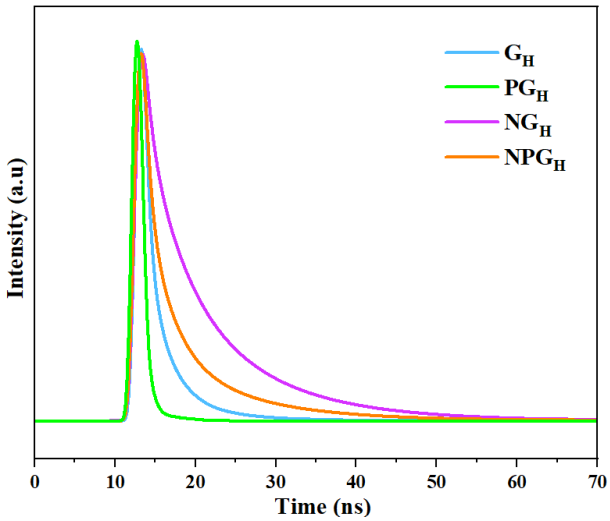

Fig. 22 Time-resolved fluorescence decay spectra for doped (PG_H, NG_H, NPG_H) and undoped (G_H) multilayer graphene derivatives

Fluorescence lifetime measurements are carried out using the time-correlated single-photon counting (TCSPC) technique and the decay profiles are depicted in Fig. 22. The fluorescence decay profile exhibited multi-exponential behavior and the emission decay is best fitted using a triple exponential function. The average lifetime of undoped G_H is calculated to be 2.59 ns. After phosphorus doping, the fluorescence decay is found to be suppressed and the corresponding fluorescence lifetime is 0.39 ns. In case of nitrogen doping, the calculated fluorescence lifetime is 8.51 ns, which is much higher than that of the phosphorus-doped or co-doped (NPG_H -5.95 ns) graphene system.

For a comprehensive analysis, the radiative and non-radiative decay rates of all the samples are estimated using following equations and the results are summarized in Table 1;

Radiative decay rate, $k_r = \frac{\phi}{\tau}$ (1)

Non-radiative decay rate, $k_{nr} = \frac{1-\phi}{\tau}$ (2)

Where, ϕ and τ are quantum yield (Q.Y.), and average lifetime of the sample, respectively[73].

Table 1 Photophysical data obtained from the time-resolved fluorescence spectra

	τ (ns)	**Q.Y. %**	**K_r (ns)**	**K_{nr} (ns)**
G_H	2.67	10	0.04	0.33
PG_H	0.36	8	0.22	2.6
NG_H	8.51	16	0.01	0.09
NPG_H	5.95	12	0.02	0.14

The fluorescence Q.Y. of G_H, PG_H, NG_H, and NPG_H is determined to be around 8-16 %. The largest change in Q.Y. is found in nitrogen-doped sample, where the Q.Y. is increased by 1.6-fold times than that of the undoped sample. The calculated average lifetime is found to be consistent with the fluorescence Q.Y. for all the samples. The correlated data reveal that the long fluorescence lifetime observed for NG_H is attributable to its high Q.Y. as well as the delayed radiative decay rate. Wherein, in PG_H the non-radiative relaxation pathway is found to be more favourable, which in turn lessened its fluorescence lifetime and Q.Y. Neither phosphorus doping, or co-doping could facilitate the enhancement of fluorescence Q.Y.

The surface functional groups attached to the edges of the graphene lattice have a significant influence on the photophysical characteristics. The C-O/C-OH groups can synergistically hybridize into sp^2 conjugated π-domains to form a fluorophore, while -O-C=O/COOH groups act as a non-radiative recombination center[71]. This finding corresponds to the high-resolution XPS spectra of C1s (Fig. 15a) for G_H, PG_H, NG_H, and NPG_H. The Q.Y. followed a reverse trend with the peak height of the -O-C=O group. Therefore, it is reasonable to believe that the fluorescence Q.Y. is critically affected by epoxy/hydroxyl groups and carboxyl groups. To authenticate the photostability of as-synthesized heteroatom doped graphene derivatives, each sample was exposed to illumination (~350 nm) for 5h, and only minimal photobleaching was witnessed (< 8%) in the fluorescence emission profile examined after the exposure.

The optical analysis of the heteroatom doped graphene derivative reveals that the doping of nitrogen could significantly enhance the fluorescence properties, which are appropriate for multidisciplinary applications. Especially, the remarkable fluorescence, high quantum yield, excellent photostability, and long fluorescence lifetime exhibited by the nitrogen-doped graphene prompt them as an ideal candidate for fluorescence bioimaging applications.

5.2.5 Fluorescence bioimaging of human melanoma cells using nitrogen-doped multilayer graphene derivative

To appraise the efficacy of highly fluorescent nitrogen-doped multilayer graphene derivative (NG_H) in bioimaging applications, cellular imaging was carried out in human melanoma cells (SKMEL). Fig. 23 displays the fluorescent microscopic images of SKMEL cells incubated with NG_H obtained using an excitation filter of 450-480 nm. The sample was found to impart fluorescence to the SKMEL cell line as compared with the untreated control group of cells as observed through an inverted phase-contrast fluorescence microscope at 20 X

magnification. As can be seen from the figure, the fluorescent heteroatom-doped graphene could easily enter the cell and exhibited a green fluorescence image in sight.

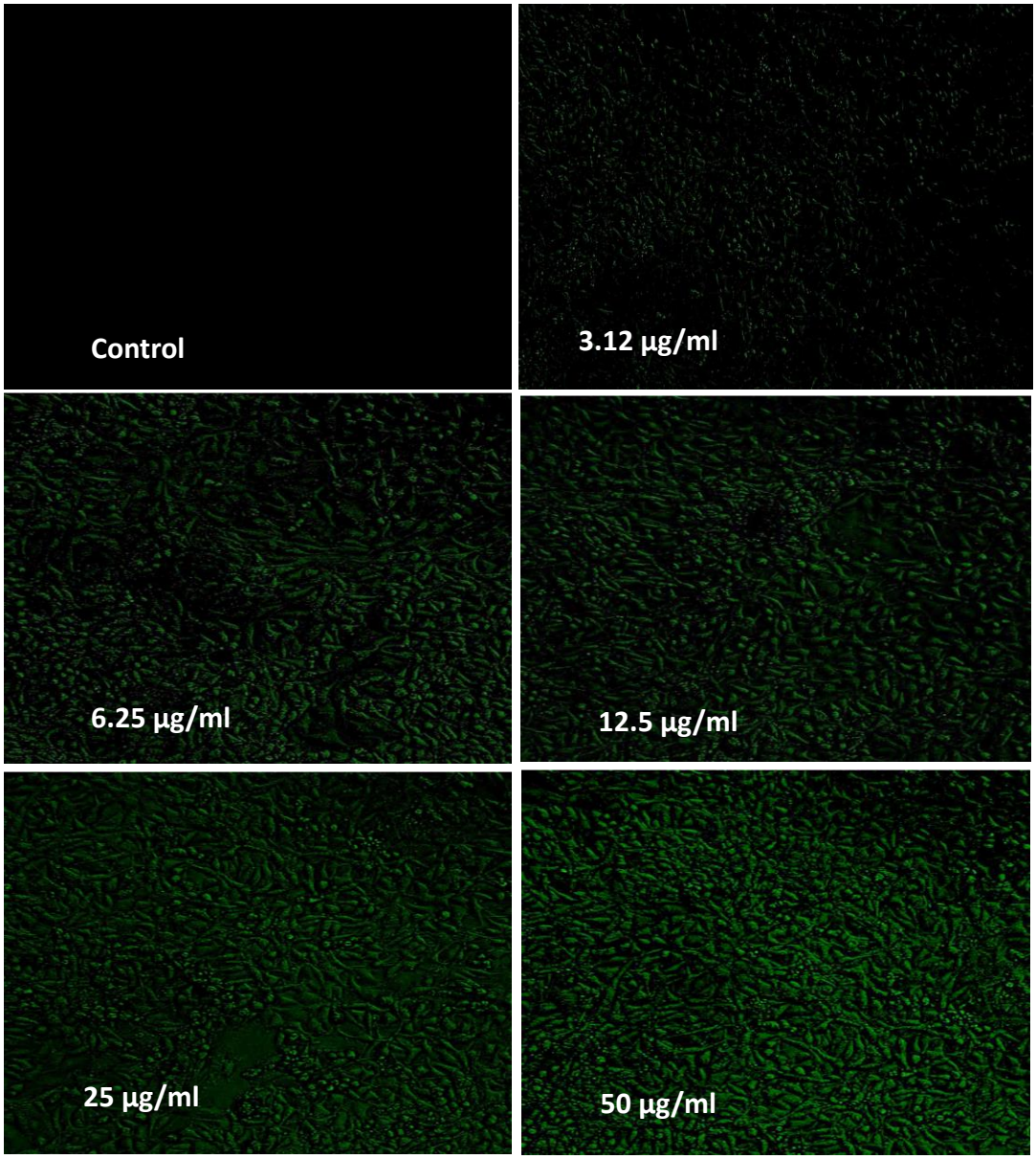

Fig. 23 Fluorescent microscopic images of SKMEL cells incubated with various concentrations of NG_H obtained using an excitation filter of 450-480 nm

The cytotoxicity of the biomarker is a vital parameter for its applicability in the bioimaging of cells. Hence, the cytotoxicity of NG_H was evaluated by means of an MTT assay for SKMEL cells. Fig. 24 indicated the cell viability evaluation of SKMEL incubated with an increasing concentration of NG_H. The cell viability was ~ 85%, even after 24 h incubation for concentrations 3.12-25 µg/mL. Thus, the above results portray the biocompatibility of as-synthesized nitrogen-doped graphene derivatives, especially in lower concentrations for bioimaging applications.

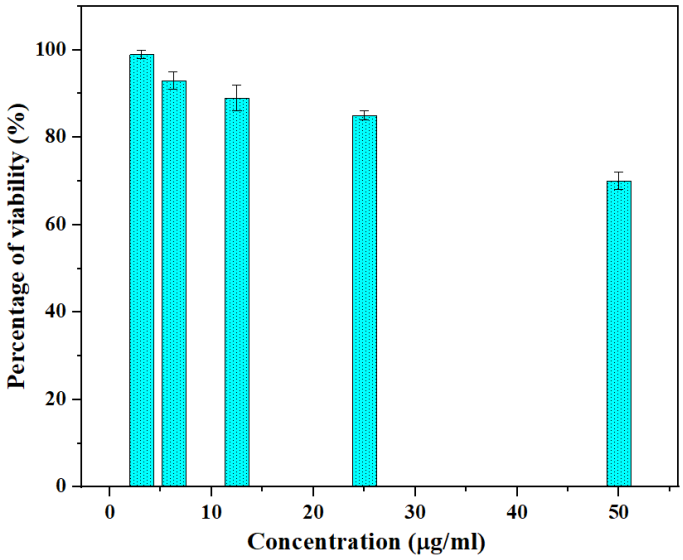

Fig. 24 Cell viability evaluation of SKMEL cells incubated with increasing concentration of nitrogen-doped multilayer graphene derivative (NG_H)

5.2.6 Electrochemical analysis of heteroatom doped multilayer graphene derivatives

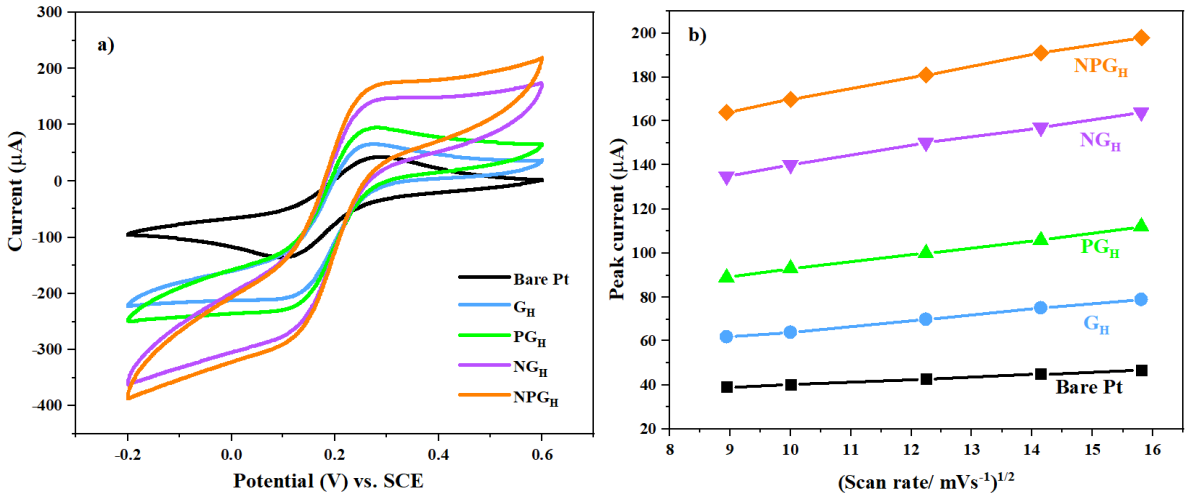

Fig. 25 a) Cyclic voltammetric responses of modified electrodes corresponding to 1mM $[Fe(CN)_6]^{-3/-4}$ in a 1M KCl solution at a scan rate of 100 mV/s b)Variation of peak current as a function of scan rate

The electrochemical efficacies of modified electrodes are evaluated employing a redox pair of $[Fe(CN)_6]^{-3/-4}$ and the corresponding cyclic voltammograms (CV) are recorded at a scan rate of 100 mV/s. As seen in Fig. 25a, compared with bare Pt, the peak currents of redox probes are significantly enhanced for PG_H and NG_H, indicating that the doping of heteroatoms can facilitate fast electron transfer kinetics. But, the peak current on NPG_H is higher than those of mono-doped graphene derivatives, which might be related to the synergistic effect and surface modifications of co-doping beneficial for fast electron transfer between $[Fe(CN)_6]^{-3/-4}$ ions and the electrode surface.

In addition, the electroactive surface area is another crucial physiochemical factor that influences the accumulation efficiency of analytes on the surface of working electrode. Obviously, when the area of the exposed surface is higher at the electrode-electrolyte interface, the electrocatalytic reactions are significantly enhanced.

The Randles-Sevcik equation (Equation 1) was utilized for the estimation of electroactive surface area [74].

$$I_p = (2.687 \times 10^5) n^{3/2} v^{1/2} D^{1/2} AC \quad (3)$$

Where I_p is the anodic peak current (A), n is the number of electrons exchanged in the process (n=1 for $[Fe(CN)_6]^{-3/-4}$), v is the scan rate (V/s), D is the diffusion coefficient (D= 6.7 x 10^{-6} cm^2/s), A is the electroactive surface area (cm^2), and C is the concentration of ferricyanide (mol/cm^3).

Fig. 25b shows the Randles-Sevcik representations of redox species obtained from the CV curves of modified electrodes. The electroactive surface area of each electrode is calculated using the slope of the Randles-Sevcik plot. The effective surface area of bare Pt, G_H, PG_H, NG_H, and NPG_H are estimated to be 0.017 cm^2, 0.037 cm^2, 0.049 cm^2, 0.062 cm^2 and 0.074 cm^2 respectively. Thus, the co-doping of nitrogen and phosphorus atoms could increase the surface area of NPG_H modified electrode by 4.5 times that of the bare Pt electrode. These results obtained from the standard redox system suggest the excellent electrochemical performance of the NPG_H modified electrode that can be utilized for sensor applications.

5.2.7 Electrochemical sensing of a high-risk abused drug, oxytocin using heteroatom co-doped graphene derivative modified electrode

The modified electrodes are then evaluated for the detection of oxytocin peptide using square wave stripping voltammetry (SWSV), as the technique is highly analytical sensitive and can also provide better peak resolution. Fig. 26a shows the SWSV curves of bare and modified electrodes in the presence of 1mM oxytocin in 0.1M PBS at pH 7. At the bare Pt electrode, no electrochemical signals of oxytocin are detected. After modifying the electrode with G_H, a low oxidation current of ~17.1 µA is achieved with a peak potential of ~ 0.3 V. The peak current is considerably increased to 30.6 µA and 41.2 µA with the modification of electrode by PG_H and NG_H, respectively. However, in the case of NPG_H, the peak current (51.3 µA) is higher than that of mono-doped graphene-modified electrodes. The variation in the oxidation peak current for the modified electrodes is shown in Fig. 26b. The superior sensing performance of NPG_H modified electrode could be attributed to that; (1) The synergistic effect generated by co-doping of nitrogen and phosphorus contributes towards its excellent electrocatalytic activity (2) The

high electrochemical surface area of NPG_H improves the charge transfer efficiency, and resulted in a higher current response (3) The formation of crumpled graphene skeleton system with underlying defect densities provides abundant reactive catalytic sites to facilitate electrocatalytic oxidation of oxytocin species as much as possible. Henceforth, based on the superior interface properties, the NPG_H modified electrodes are employed for all further experiments.

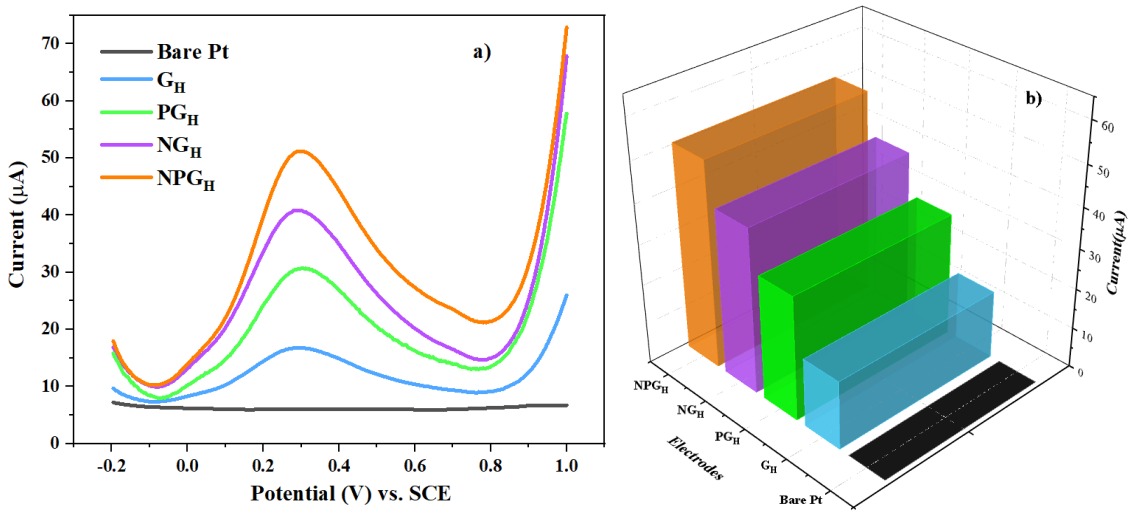

Fig. 26 a) Square wave voltammetric responses of modified electrodes in the presence of 1mM oxytocin in 0.1M PBS at pH 7 b) Variation of peak current for modified electrodes

Taking into account the electrocatalytic behavior of analyte adsorbed on the electrode surface, the following mechanism of electrochemical oxidation of oxytocin can be assumed. The oxytocin molecule consists sequence of 9 amino acids (tyrosine-isoleucine-glutamine-asparagine-cysteine-proline-leucine-glycine), among that tyrosine is known to be electrochemically active and hence, oxytocin can be detected electrochemically. The general understanding is that, the phenol group in the tyrosine moiety is initially oxidized to semi-quinone by loss of 2 electrons [75]. Subsequently, this unstable oxidation product is thought to undergo chemical reaction to form easily oxidizable product hydroquinone, which would be then adsorbed on the surface of the electrode [76]. This is evident from the SWSV curves for the hydroquinone's redox species at ~ 0.3 V in Fig. 26a. The mechanism involved in the electrochemical redox reaction of oxytocin is represented in Fig. 27.

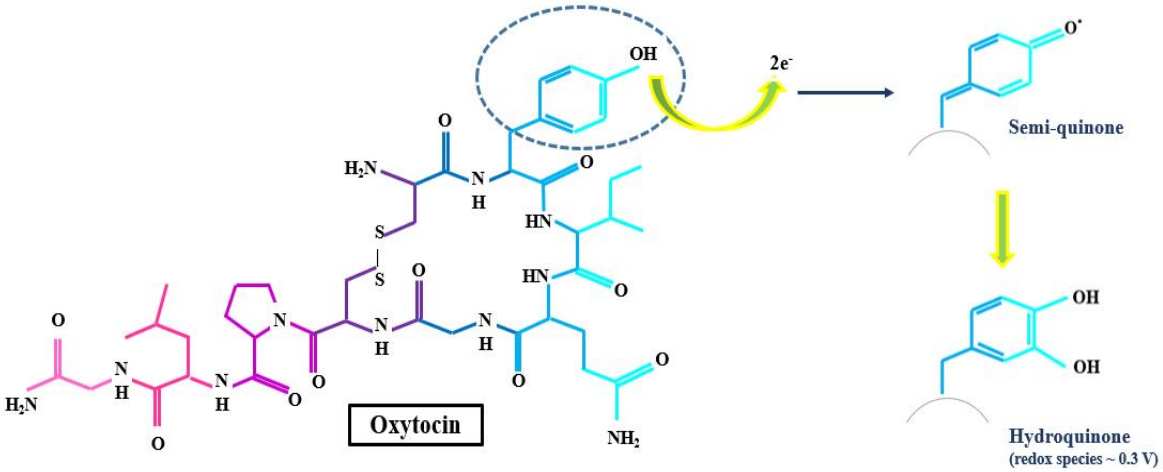

Fig. 27 Schematic representation of the plausible mechanism for electro-oxidation of oxytocin

The voltammetric conditions such as supporting electrolyte pH value and accumulation time that influences the electrochemical redox behavior of oxytocin were optimized, considering the enhanced voltammetric signal. The effect of supporting electrolyte's pH values on the electrochemical response for 1 mM oxytocin was evaluated in the pH range of 5 to 10 (Fig. 28a). The peak currents of the oxytocin are found to be increasing upto a pH value of 7, and with the further increment of the pH value, the current is gradually declined. Therefore, according to the maximum peak current obtained at neutral medium, 0.1 M PBS with pH 7 is selected for the latter experiments. The accumulation time for the adsorptive stripping voltammetric detection is a vital aspect that assurances the maximum probable exposure of electrode surface to the analyte. The influence of accumulation time was investigated in the range from 0 to 90 s, and the results are shown in Fig. 28b. The peak current of oxytocin is intensified until it reached the plateau region at 30 s. With further increase in accumulation time, the peak current persisted at a constant value, and afterward, current response is weakened. This phenomenon is due to the surface saturation of the electrode surface due to the adsorption of oxytocin, thus blocking the transfer of electrons and leading to electrode fouling [77]. Considering the highest current response, an accumulation time of 30 s is employed for the following analysis.

The application of NPG modified electrode in quantitative determination of oxytocin was investigated by changing its concentrations using the SWSV method under optimized conditions. The dependence of stripping current for various concentrations of oxytocin in the range of 0.1 to 95 nM is depicted in Fig. 28c. As can be seen from the SWSV curves, the oxidation peak around ~ 0.3 V displayed a proportion increment with the standard additions of oxytocin. The calibration plot of oxidation peak current (I_P) vs. concentration (C) exhibited a

linear response in two ranges (Fig. 28d). The first linear range is obtained between 0.1 nM and 10 nM with regression equation, I_P (µA) = 8.41 + 0.12.C (nM) (R^2=0.987) and the second range between 15 nM and 95 nM with regression equation, I_P (µA) = 8.43 + 0.07.C (nM) (R^2=0.993). The limit of detection (LOD) is calculated from the first linear range using the equation LOD= 3σ/m; where σ is the standard deviation and m is the slope of the calibration plot. The detection limit of the NPG_H modified electrode is found to be 0.04 nM. Overall, the sensor based on coke-derived heteroatom doped graphene electrode developed in the present work displayed superior analytic performance, especially with respect to an improved linear detection range, as well as the lower limit of detection in comparison to conventional analytical techniques and other electrochemical sensors [78][79].

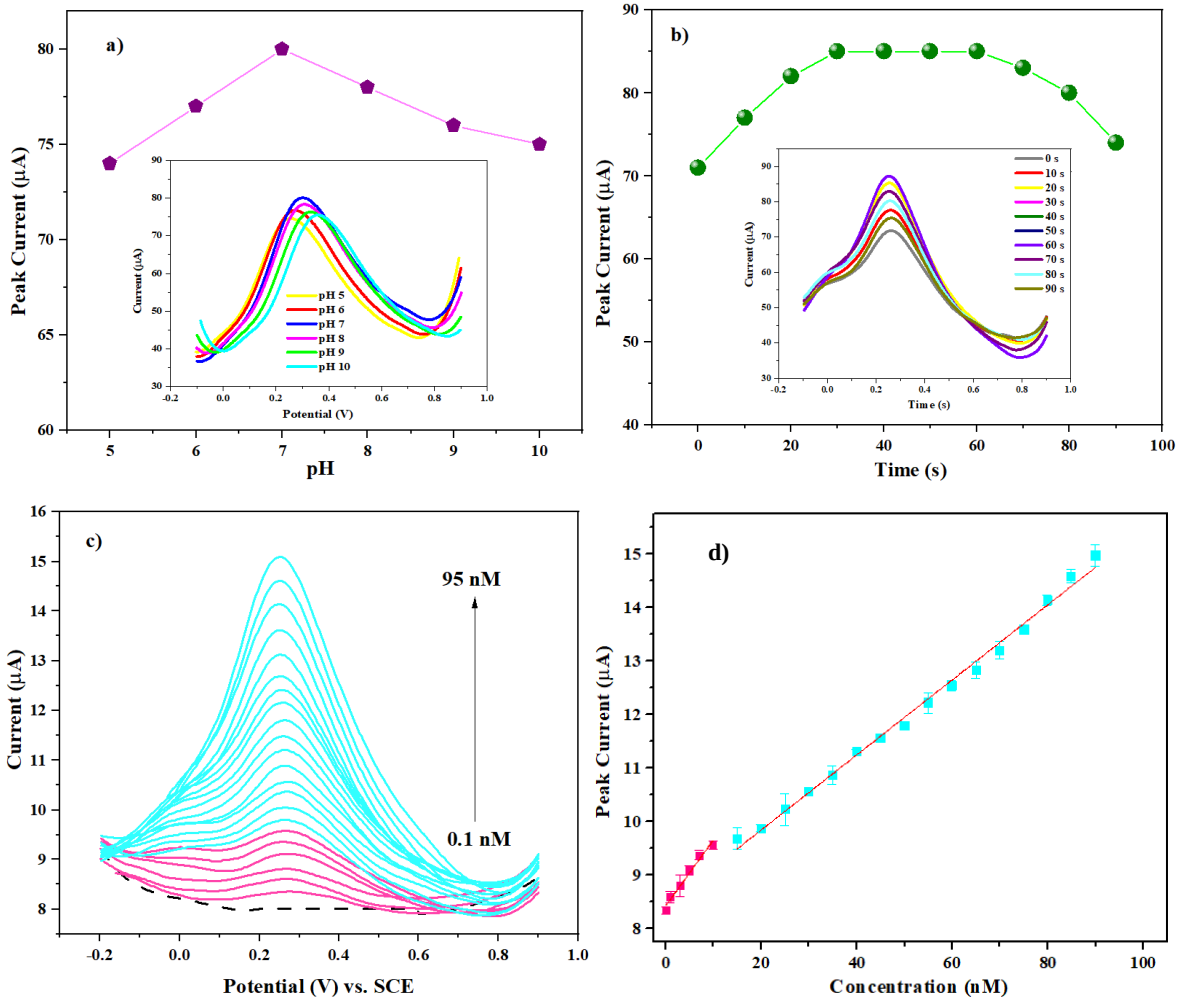

Fig. 28 a) The dependence of peak current of oxytocin (1mM) in 0.1M PBS for pH range 5 to 10 (Inset: SWSV curves obtained for various pH) b) The dependence of peak current of oxytocin (1mM) in 0.1M PBS on accumulation time (Inset: SWSV curves obtained for various accumulation time) c) Square wave voltammetric responses of NPG_H modified electrode in 0.1M PBS at pH 7 for different concentrations of oxytocin d) Variation of peak current as a function of oxytocin concentrations

The effect of possible interferents on the current response of NPG_H modified electrode in detection of oxytocin was studied in the presence of various foreign species (Fig. 29). The biological substances like ascorbic acid, uric acid, glucose and sucrose often co-exist with tyrosine moiety in food processing, human fluids and clinical analysis. Therefore, the interfering impact of these substances are evaluated at 100-fold concentrations. In addition, 500-fold excess concentrations of commonly occurring inorganic ions like K^+, Na^+, Mg^{2+}, Ca^{2+} Cl^-, Zn^{2+}, and Fe^{3+}, are tested as interferents. The peak current of oxytocin is recorded in the presence of interfering species and compared with that of the current response without any interferents. There is no significant change in the sensing response efficiency of oxytocin, confirming the excellent selectivity of fabricated sensor towards the detection of oxytocin.

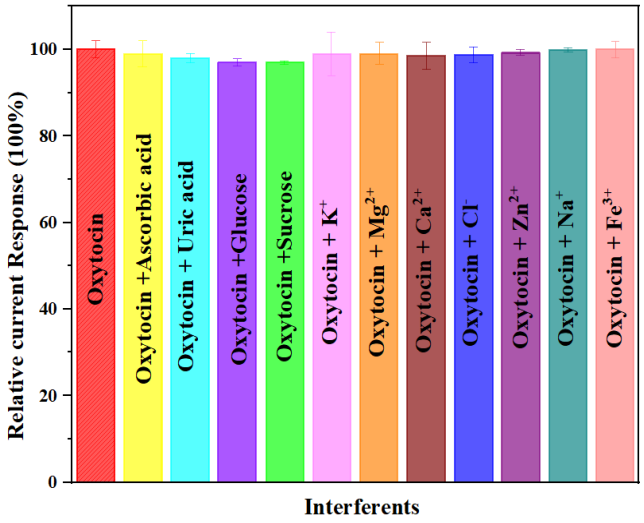

Fig. 29 Selectivity test of NPG_H modified electrode in detection of 1µM oxytocin in the absence and presence of interfering species

To assess the reproducibility of the developed sensor, 5 different NPG_H modified electrodes were fabricated to determine 1 µM oxytocin in 0.1M PBS at pH 7. The peak currents for all electrochemical assays measured using 5 electrodes were almost constant, as evidenced by the current response plot in Fig. 30a. The relative standard deviation is found to be 2.11 %, proving the satisfactory reproducibility of the sensor for analytical purposes. However, when it comes to practical applications, the long-term stability of the electrode is an essential aspect that has to be considered. The stability of NPG_H modified electrode stored at room temperature was studied once in 5 days by measuring 1 µM of oxytocin with SWSV method (Fig. 30b). The results showed that the current response declined to 98 % after the first week of storage and then to ~ 88 % after four weeks, implying the adequate stability of fabricated electrode.

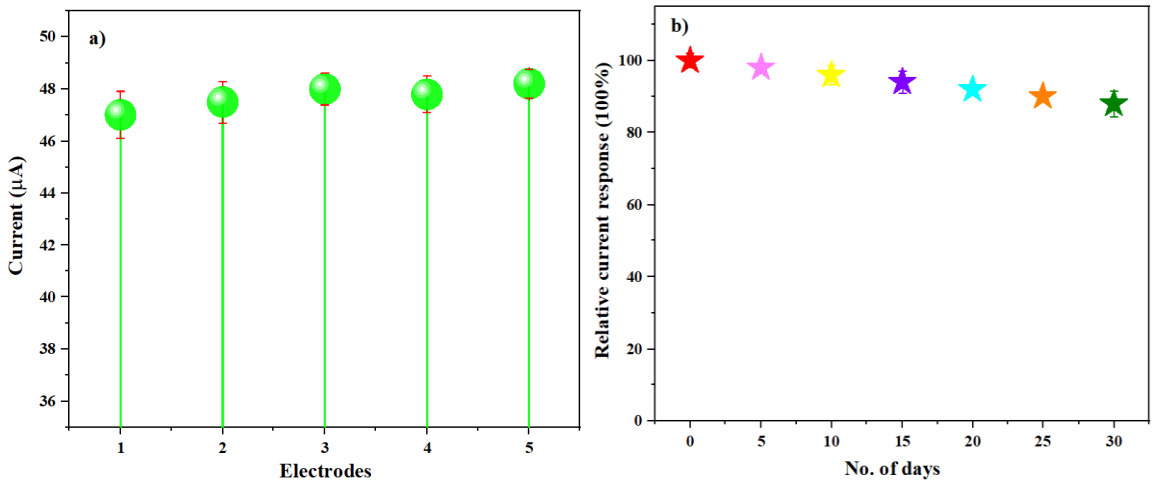

Fig. 30 a) Square wave voltammetric responses of 5 different NPG_H modified electrodes in 0.1M PBS at pH 7 for 1μM oxytocin b) Stability test of NPG modified electrode for 4 weeks

Table 2 Determination of oxytocin in real samples using NPG_H modified electrode

	Added (nM)	Found (nM)	Recovery	RSD (%)
Milk	30	29.17	97.23	2.89
	60	59.44	99.06	1.45
	90	93.23	103.58	4.46
Fruit Juice	30	30.21	100.07	3.13
	60	58.89	98.15	2.11
	90	88.76	98.62	2.76
Human Urine	30	30.66	102.23	3.01
	60	59.86	99.77	3.34
	90	93.42	103.81	1.54
Human saliva	30	28.66	95.54	2.98
	60	58.80	98.01	3.44
	90	92.30	102.78	2.89

The proposed sensor was utilized for the non-invasive detection of oxytocin in real life samples such as milk, fruit juice, human a) urine, and b) saliva. For oxytocin content estimation, samples were spiked with three different concentrations (30 nM, 60 nM, and 90 nM) of oxytocin prepared from its pharmaceutical formulation (Oxytocin injection I.P., 2.5mg/mL, Pitocin ®, Pfizer Limited, India). The samples are analyzed via method of standard addition and each experiment is repeated thrice to verify the reproducibility. As shown in Table 2, the obtained RSD value is below 5%, signifying the adequacy and precision of the proposed method. The recovery values are found in the range of 90.01-105.23 %, entailing the promising

practical application of developed NPG_H modified electrode for the determination of oxytocin in food and biological samples.

5.2.8 Conclusion

In this study, heteroatom-doped multilayer graphene derivatives were synthesized via a one-pot hydrothermal method utilizing phosphoric acid and ethylenediamine as phosphorus and nitrogen precursors, respectively. The successful doping of heteroatoms in the graphene lattice was confirmed via XRD, Raman, FTIR, EDX, and XPS analysis. It is found that nitrogen doping could enhance the fluorescence properties of graphene derivatives, wherein phosphorus doping and co-doping could neither facilitate the enhancement of fluorescence Q.Y and lifetime. Utilizing the remarkable fluorescence properties and noteworthy biocompatibility, nitrogen-doped graphene derivative was used as a biomarker for the fluorescence bioimaging application of human melanoma cells. But, the electrochemical characteristics of graphene derivatives were significantly improved by the co-doping of heteroatoms, resulting from their synergistic effect. The voltammetric response showed that effective co-doping of nitrogen and phosphorus atoms could increase the electrochemically active surface area of the electrode by 4.5 times that of bare Platinum working electrode. As a result, NPG_H modified electrode was utilized for the electrochemical sensing of a potentially hazardous drug, oxytocin. The developed sensor displayed commendable sensitivity, selectivity, reproducibility, and repeatability with a lower detection of a limit of 0.04 nM. In conclusion, doping of heteroatoms on the novel coke-based multilayer graphene derivatives could harvest excellent fluorescence and electrochemical applications, which is preferred over other conventional analysis techniques.

5.3 SIMULTANEOUS HETEROATOM DOPING AND ACTIVATION OF COKE-BASED MULTILAYER GRAPHENE DERIVATIVES FOR SUPERCAPACITOR APPLICATIONS

In the current study, simultaneous heteroatom-doped and activated samples are obtained using H_3PO_4 as phosphorus precursor as well as an activation agent. In order to understand the efficacy of co-doping of heteroatoms in electrochemical properties, the doping of nitrogen was achieved using ethylenediamine as the nitrogen precursor. The as-synthesized phosphorus-doped, nitrogen-doped, and co-doped coke-based multilayer graphene derivative was denoted as PG_A, NG_A, and NPG_A, respectively. The potential applications of as-synthesized heteroatom

doped activated multilayer graphene derivatives as an electrode material for supercapacitor are presented and discussed in detail.

5.3.1 Structural and morphological analysis of the heteroatom doped, activated multilayer graphene derivatives

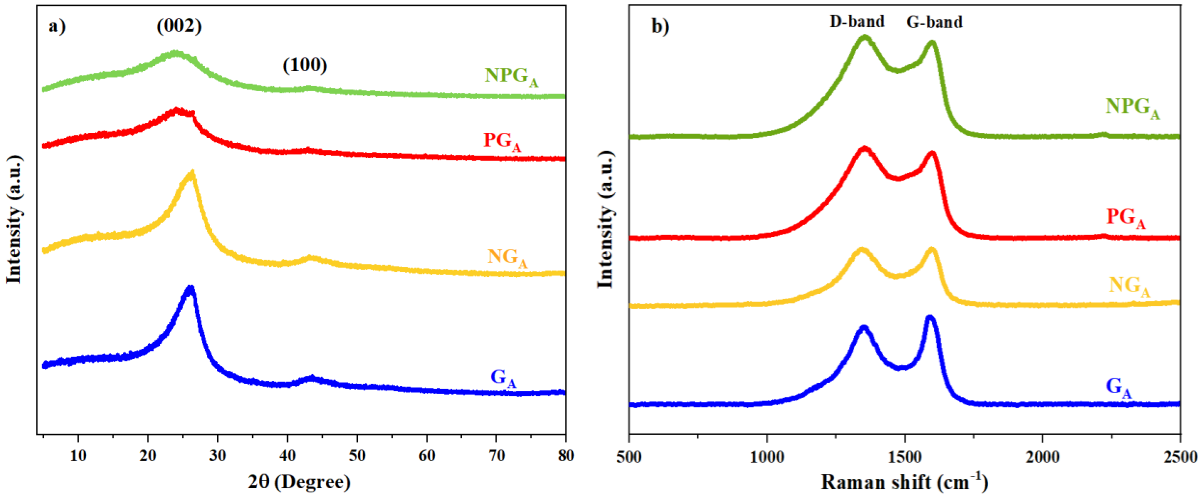

Fig. 31 a) X-ray diffraction pattern b) Raman profile of doped (NG_A, PG_A, NPG_A) and undoped (G_A) activated multilayer graphene derivatives

The X-ray diffraction profiles of as-synthesized heteroatom doped, activated samples are depicted in Fig 31a. All the samples exhibited diffraction peaks corresponding to (002) and (100) planes at ~ 26º and 43º, respectively. In PG_A and NPG_A, the peak due to (002) plane gradually reduced and become broader, which implies that the activation with phosphoric acid inhibits the stacking effect or reduces the domain size of graphene. Furthermore, (002) peak shifted to a lower 2θ position ~ 24.1º (PG_A) and 24.6º (NPG_A); this change might be ascribed to the introduction of oxygen functional groups from H_3PO_4.

Raman analysis was conducted to further characterize the carbon structure and degree of disorderedness. As seen in Fig. 31b, Raman spectra display graphitic band (G) at 1590 cm^{-1}, 1601 cm^{-1}, 1603 cm^{-1}, 1606 cm^{-1}, and disorder band (D) at 1350 cm^{-1}, 1352 cm^{-1}, 1354 cm^{-1}, 1356 cm^{-1} for G_A, NG_A, PG_A, and NPG_A, respectively. The observed blue shift in the peak positions of G-band in doped samples is due to the stiffening of phonons aroused from the modifications in electronic properties and bond configuration induced by doping of heteroatoms[51]. The ratio of D-band to G-band quantifies the extent of disorderedness in a material. The value of I_D/I_G ratio for G_A, NG_A, PG_A, and NPG_A, is calculated to be 0.86, 0.97, 1.01, and 1.08, respectively. These results indicate that the heteroatom doping along with phosphoric acid activation can enhance the defect densities of materials. These characteristics

are favorable for the formation of defect structures, thus favoring the accessibility of more active sites which in turn can improve the electrochemical performance.

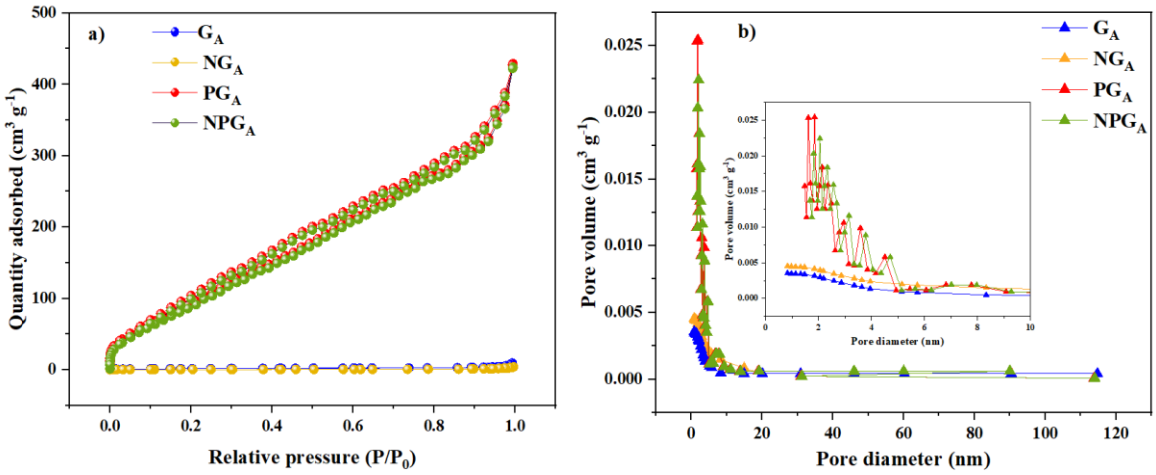

Fig. 32 a) N_2 adsorption-desorption isotherms b) pore size distribution of doped (NG_A, PG_A, NPG_A) and undoped (G_A) activated multilayer graphene derivatives

The effect of activation on the textural properties of prepared samples was thoroughly examined by employing surface area and pore size analyzer. Fig.32a shows the N_2 sorption isotherm of heteroatom doped activated samples. It was found that the profile of H_3PO_4 activated samples possesses a combination of the shape of type I and type IV, as prescribed by IUPAC[54]. In low-pressure region, samples show a steep increase in their isotherm curve followed by a steady increase in plateau region with the increase in pressure. For relative pressure $P/P_0 > 0.45$, the occurrence of hysteresis loop in the desorption curve indicates the presence of micropores and mesopores in the prepared samples. This is further confirmed by the results from the pore size distribution, showing that the H_3PO_4 activated samples exhibit a hierarchical micro-mesoporous framework (Fig.32b). The porosity is a crucial and significant property in deciding the performance of electrochemical energy storage. While the ions get adsorbed and accumulated in the micropores to form a double layer, the diffusion of ions via low resistive paths to these micropores is offered by mesopores. The BET surface area is calculated to be 405.1 m^2/g, 420.4 m^2/g, m^2/g, 2.7 and 5.2 m^2/g, for NPG_A, PG_A, NG_A, and G_A, respectively. The high surface area and improved porosity (abundant micropores and mesopores) provide a large interfacial area between electrode and electrolyte which provides an excess of interaction and charge storage.

5.3.2 Elemental compositional analysis of the heteroatom doped, activated multilayer graphene derivatives

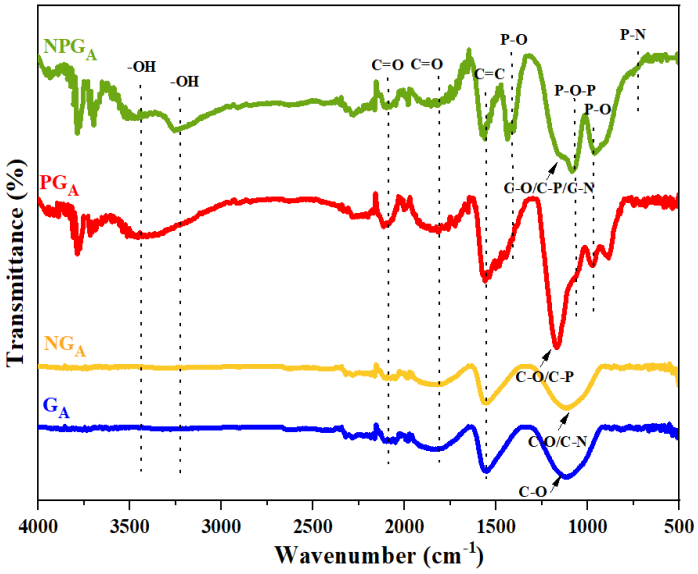

Fig. 33 FTIR spectra of doped (NG_A, PG_A, NPG_A) and undoped (G_A) activated multilayer graphene derivatives

Fig. 33 manifests the difference in surface functional groups of doped and undoped activated multilayer graphene derivatives. According to FTIR results, the spectrum of phosphoric acid activated graphene samples are rich in oxygen-containing functional groups. Bands at 3440 cm^{-1} and 3234 cm^{-1} are attributed to the -OH stretching vibrations. The spectrum displayed vibrations of C=O of a carboxylic group between 1700-2200 cm^{-1}. The characteristic peak due to the carbon skeleton network (C=C) is observed at 1570 cm^{-1}. The wide band at 1175 cm^{-1} may be assigned to the integrated vibrations of C-O, C-P, or C-N bond. The bands at 1390 cm^{-1} and 963 cm^{-1} are caused by the symmetric vibrtaions of P-O and a peak at 1070 cm^{-1} is due to the symmetric vibration of P-O-P bridge. Appearance of new peak at 730 cm^{-1} in NPG_A indicates the occurrence of N-P bond induced by the co-doping of heteroatoms. The presence of these prominent peaks of oxygen based functional groups especially in PG_A and NPG_A suggests the hydrophilic nature, which determines the wettability of the material.

5.3.3 Surface chemistry characteristics of the heteroatom doped, activated multilayer graphene derivatives

To obtain insight into the mechanism of doping and nature of chemical bonds formed during the activation process, XPS spectra were obtained for all the samples and are displayed in Fig. 34. The XPS survey spectra exhibiting typical peaks of C, O, N and P confirm that the doping precursors are effectively incorporated into the graphene structure. The survey spectrum revealed the presence of phosphorus and nitrogen atoms in NPG_A (N: 5.82 At %, P:

5.79 At %), PG_A (P: 5.94 At %), and NG_A (N: 6.12 At %). Wherein, undoped G_A comprises only carbon and oxygen atoms with an atomic concentration of 92.12 At % and 7.88 At %, respectively.

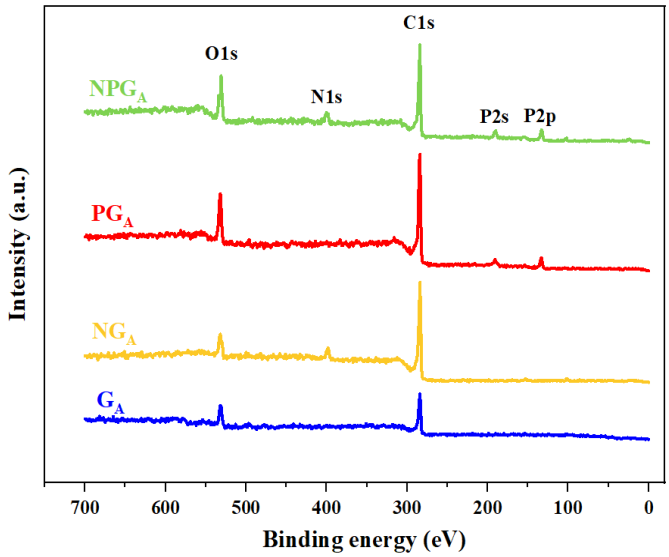

Fig. 34 XPS survey spectrum of doped (NG_A, PG_A, NPG_A) and undoped (G_A) activated multilayer graphene derivatives

The high-resolution deconvoluted C1s XPS spectra revealed that besides a prominent peak at 284.7 eV owing to the C-C bond, an apparent tail at higher binding energy attributed to the bonding of carbon atom with oxygen functional groups and heteroatoms is also present (Fig. 35a). The C1s region of all the samples consists of well-resolved binding energy configurations at 286.1 ± 0.1 eV, 287.5 ± 0.2 eV, and 288.9 ± 0.3 eV related to epoxy/hydroxyl (C-O/C-OH), carbonyl (C=O) and carboxyl groups (-O-C=O), respectively. Compared to G_A, an additional component at 285.5 ± 0.2 eV assigned to C atoms directly bonded to the heteroatoms (N/P) is observed in NG_A, PG_A, and NPG_A. The deconvoluted O1s spectra shown in Fig. 35b. disclose the different chemical states of oxygen in each sample. The peak at 530.6 ± 0.1 eV is related to the carbon double bonded to oxygen (C=O). The peaks at 531.7 ± 0.3, 533.1 ± 0.2 eV, and 534.2 ± 0.3 eV are corresponding to the C-O (of epoxy group), C-OH (of hydroxyl group), and -O-C=O (of carboxyl group), respectively. It can be observed from the comparison of O1s spectra, NG_A, PG_A, and NPG_A have additional peaks at 532.4 ± 0.1 eV and 533.7 ± 0.1 eV implying the presence of nitric oxide (NOx) and P-O-P group aroused from the introduction of heteroatoms.

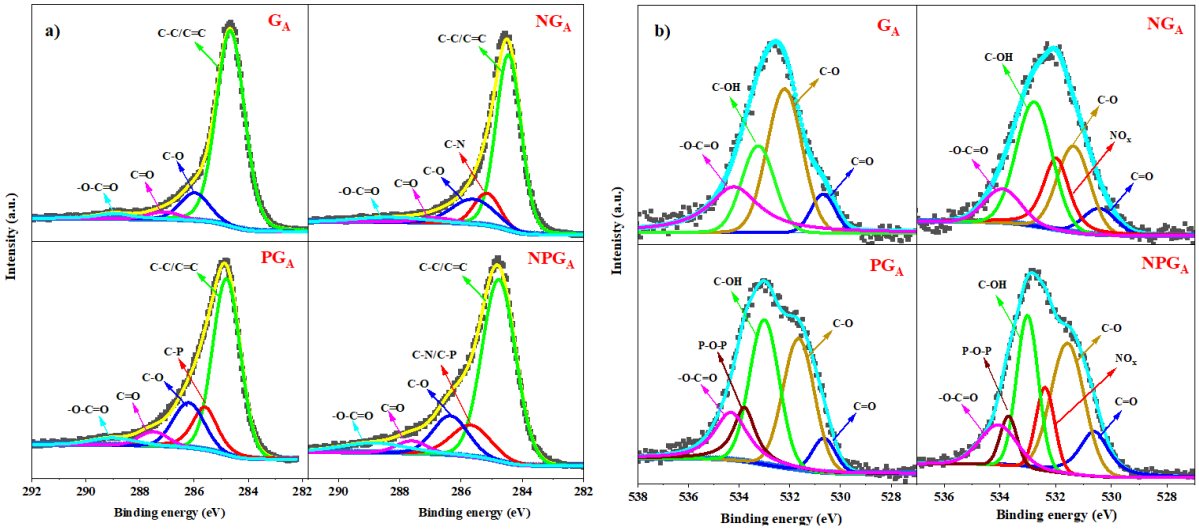

Fig. 35 High-resolution XPS deconvoluted spectra of a) C1s b) O1s for doped (NG_A, PG_A, NPG_A) and undoped (G_A) multilayer graphene derivatives

The atomic component fraction of each surface functional group has been calculated from the area of deconvoluted C1s and O1s peaks. The variation in the content of graphitic carbon (area of C-C/C=C peak) and oxygenated carbon (sum of CO + C=O + -O-C=O peaks) in each sample is presented in Fig. 36. It is significant that the fraction of graphitic carbon gradually reduced upon doping of heteroatoms. The highest fraction of graphitic carbon (94%) is detected in the undoped sample (G_H), followed by NG_H (89%), PG_H (83%), and NPG_H (78%). This trend was explained by two reasons (i) replacement of carbon atoms by heteroatoms (N/P) (ii) introduction of oxygen functionalities by the phosphorus dopant (H_3PO_4-Phosphoric acid). The atomic composition fraction of oxygen species in as-synthesized samples is displayed in Fig. 36b. Comparison between the atomic concentrations shows that the PG_A and NPG_A are enriched with oxygen functionalities after the activation process. This suggests that phosphoric acid acts as an oxidizing agent resulting in the formation of carbon-oxygen structures. The contribution of C-O and C-OH is found to be more substantial compared to C=O and O-C=O. In heteroatom-modified samples, small contributions of NOx and P-O-P are also witnessed. It should be noted that the oxygen functional groups influence the electrochemical behavior of graphene electrodes. Especially, suitable oxygen content and hydrophilic group like -O-C=O incorporated in the graphene network can facilitate the wettability of the electrode material.

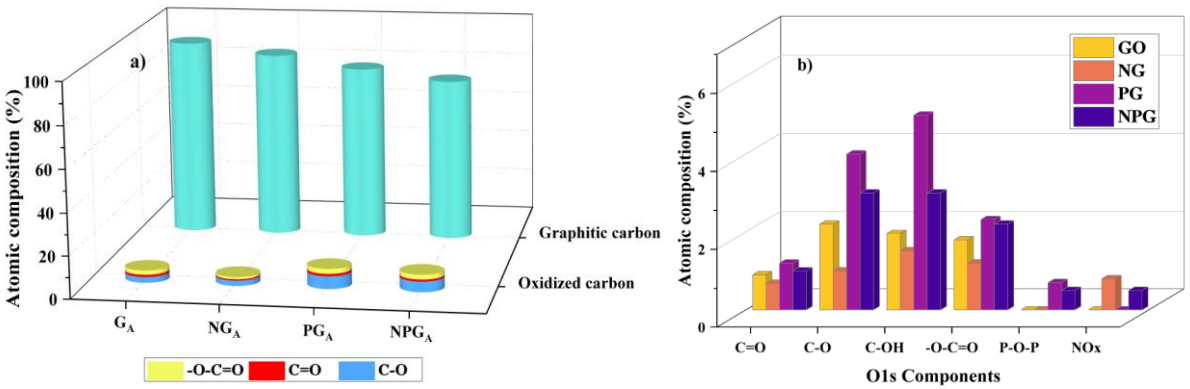

Fig. 36 (a,b) Surface atomic composition of different functionalities obtained from C1s and O1s peaks of doped (NG_A, PG_A, NPG_A) and undoped (G_A) multilayer graphene derivatives

The N1s spectra demonstrate that nitrogen atoms are inserted into graphene structures in the form of "pyridinic", "pyrrolic", and "graphitic" N (Fig. 37a). The peaks at 398.6 ± 0.1 eV, 400.1 ± 0.1 eV, and 401.8 ± 0.2 eV are ascribed to the pyridinic N and graphitic/pyrrolic N doping configurations. Also, a small peak is observed at 401.1 eV in N1s spectra of NPG_A, which is associated with the incorporation of N-P features [69]. In comparison with PG_A, the N1s spectra of NPG_A possess a graphitic/pyrrolic and pyridinic N-rich graphene network. The possible reason for the high content of graphitic/pyrrolic N and pyridinic N is due to the higher amount of nitrogen atoms available with the active sites of vacant carbon bonds created by the oxygen functional group introduced by the phosphoric acid. The electrochemical behavior is heavily dependent on the type and amount of nitrogen species. The experimental and theoretical calculations indicate that graphitic/pyrrolic N and pyridinic N-rich graphene networks can be essential to enhance the supercapacitive characteristics.

The state of phosphorus atoms was examined by analyzing the P2p XPS core level peaks. As seen in Fig. 37b, the P2p spectra of PG_A and NPG_A could be deconvoluted into 2 bands: P-O (134.6 ± 0.2 eV) and C-PO_3 (133.3 ± 0.3 eV), representing that the P atoms are in a high-oxidation state. Also, the C-P band at a less oxidized state (132.6 ± 0.1 eV) which is assigned to the graphitic phosphorus is observed. This indicates that at a higher temperature more phosphorus is inserted into the graphene network by substituting the carbon atoms and hence no peak due to the elemental phosphorus is witnessed. In addition, a small peak at 132.3 eV owing to the N-P bond is observed in the P2p spectra of NPG_A. This co-doping of P and N atoms can create new active sites and initiate a synergistic effect, which can further enhance the electrochemical performance.

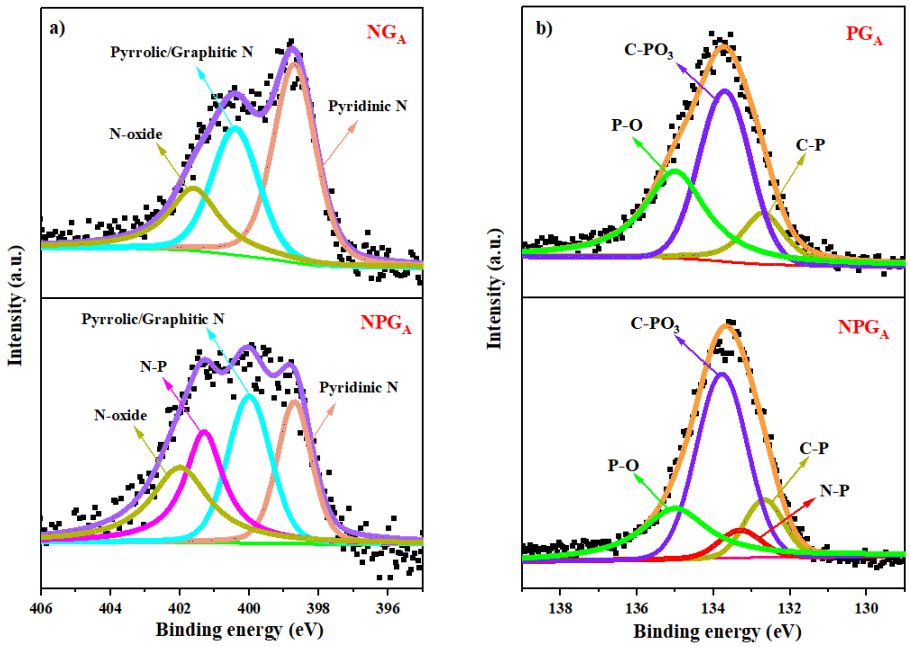

Fig. 37 High-resolution XPS deconvoluted spectra of (a) P2p (b) N1s for doped (NG_A, PG_A, NPG_A) multilayer graphene derivatives

5.3.4 Heteroatom doped, activated graphene derivatives as an electrode material for supercapacitor applications

5.3.4.1 Three-electrode cell configuration

The electrochemical performance of as-prepared samples for the potential application as supercapacitor electrodes was evaluated using a 3-electrode system. Fig. 38a shows the cyclic voltammetric (CV) curves obtained for various samples in a three-electrode cell configuration within the potential window of 0 to 0.8 V at a scan rate of 50 mV/s. The quasi-rectangular shape of the CV curves indicates the electric double layer and pseudocapacitive nature of the modified electrodes. Interestingly, the current densities were found to be drastically improved upon the phosphoric acid activation. Note that, the performance of NPG_A was much superior in comparison to PG_A, suggesting that the doping of nitrogen combined with the activation process can significantly enhance the energy storage characteristics.

The galvanostatic charge-discharge (GCD) measurements for the samples were carried out within the potential window of 0 to 0.8 V at a current density of 1A/g and the results are shown in Fig. 38b. The slight deviation from the triangular shape of the GCD curves also advocates the contribution of both electric double layer and pseudocapacitive behaviors in the charge storage mechanism. The pseudocapacitance contributions are from the oxygen-containing functional groups of GO and the heteroatoms (N, P) introduced in the graphene system via doping. The specific capacitance obtained under different current densities is shown in Fig.38c. At 1A/g, estimated specific capacitance values are 28 F/g, 37 F/g, 215 F/g, and 322 F/g, for

G_A, NG_A, PG_A, and NPG_A, respectively. These results are consistent with the CV characterizations. The electrochemical stability of the NPG_A modified electrode was evaluated by performing the charge-discharge technique under the current density of 15 A/g. After 5000 cycles, the capacitance retention was ~93 %, which indicates the excellent cyclic stability of the NPG_A modified electrode (Fig. 38d).

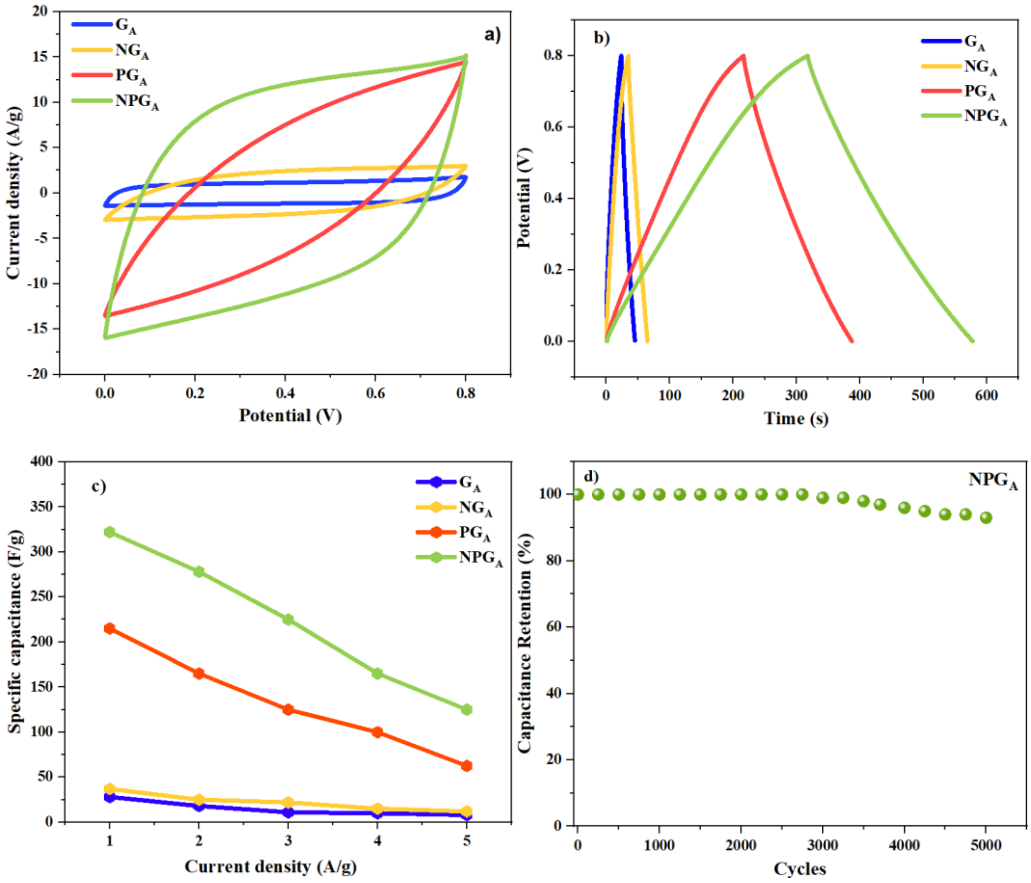

Fig. 38 a) CV curves of heteroatom doped and activated multilayer graphene derivatives at 50 mV/s b) GCD curves of heteroatom doped and activated multilayer graphene derivatives at 1A/g c) The specific capacitance obtained at different current densities d) Capacitance retention of NPG_A electrode as a function of GCD cycle number under a current density of 15 A/g

5.3.4.2 Two-electrode cell configuration

To evaluate the practical applicability, the activated samples were further tested in a 2-electrode cell system by means of cyclic voltammetry, galvanostatic charge-discharge technique, and electrochemical impedance spectroscopy. The CV curves obtained at a potential scan rate of 50 mV/s, show slight distortions from the rectangular shape, associated with the pseudocapacitance contributions (Fig. 39a). However, by comparing the current response of the CV curves, NPG_A exhibited higher current density compared to mono-doped (NG_A, PG_A) activated or undoped (G_A) samples. To get a more accurate idea about the specific capacitance

values of the as-synthesized material, GCD curves were obtained within the potential window of 0 to 0.8 V (Fig.39b). The isosceles triangular GCD curves without many distortions demonstrate the remarkable capacitive behavior and noteworthy electrochemical reversibility. But, NPG_A displayed an extended discharge time in the GCD curve and thus leading to a higher specific capacitance. The specific capacitances of G_A, NG_A, PG_A, and NPG_A at a current density of 1A/g are calculated to be 14 F/g, 19 F/g, 117 F/g, and 167 F/g, respectively (Fig.39c). Furthermore, no IR drop was witnessed in the GCD curve of activated sample, representing the negligible resistance of the electrode, which could be attributed to its excellent conductivity. Finally, the cyclic stability and practical durability of NPG_A were checked by performing 5000 numbers of GCD cycling at 15A/g (Fig.39d). The capacitance retention was found to be ~90% after 5000 cycles.

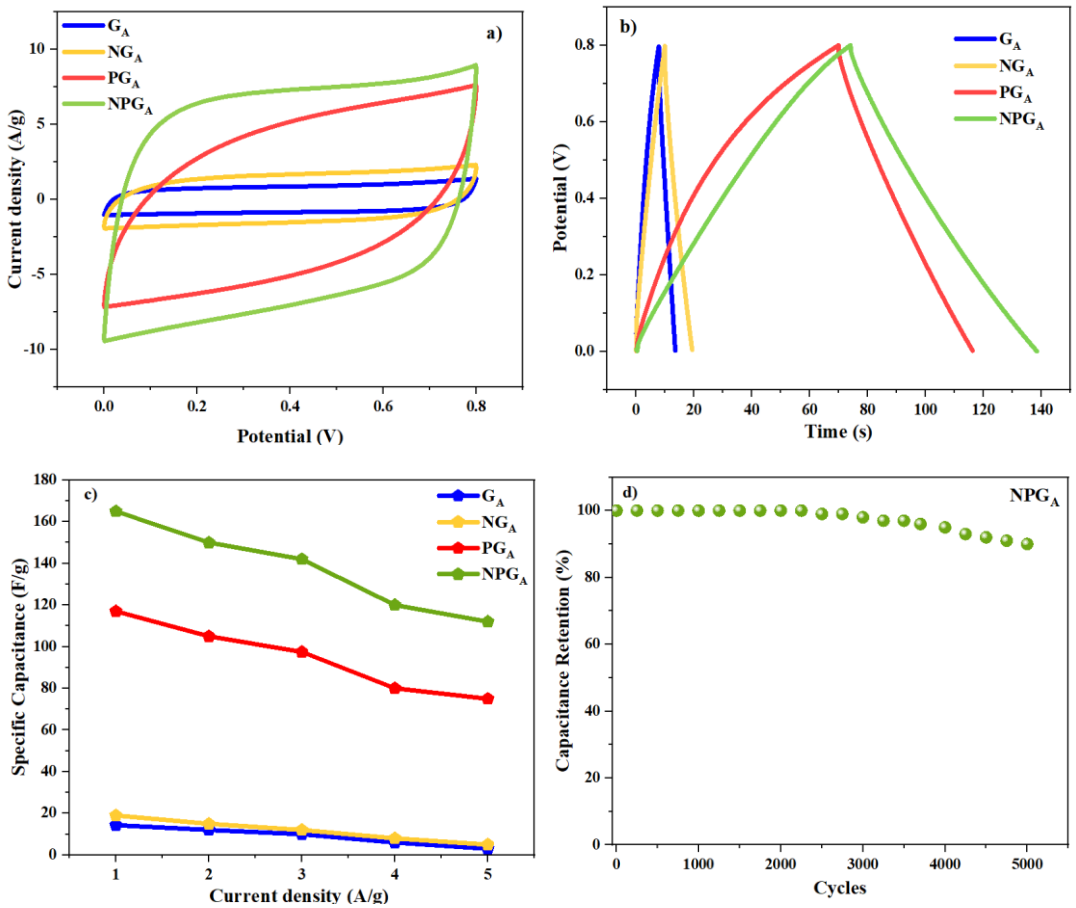

Fig. 39 a) CV curves of heteroatom doped and activated multilayer graphene derivatives at 50 mV/s b) GCD curves of heteroatom doped and activated multilayer graphene derivatives at 1A/g c) The specific capacitance obtained at different current densities d) Capacitance retention of NPG_A electrode as a function of GCD cycle number under a current density of 15 A/g

To understand the electrochemical kinetics of fabricated electrodes, electrochemical impedance spectroscopy was performed in the frequency range of 0.01 to 100 kHz with an

impedance potential of 5mV, and the comparative Nyquist plots are shown in Fig.40a. The diameter of the semi-circular arc observed in the high-frequency region represents the charge transfer resistance (R_{ct}) and the perpendicular straight line in the low-frequency region indicates the electric double layer formation or the diffusion resistance. The R_{ct} values for G_A, NG_A, PG_A, and NPG_A are 37.4 Ω, 26.44 Ω, 6.9 Ω, and 2.8 Ω, respectively. As evident from the plot, there is a significant reduction in the diameter of the semi-circular arc for PG_A and NPG_A, in comparison with G_A and NG_A implying their lower charge transfer resistance. The smaller diameter of the semicircle signifies the higher penetrating ability of the electrolyte ions into the electrode material. Further, in the low-frequency region, NPG_A displayed a steeper slope of ~ 90° than other samples, showing its better capacitive behavior. Deviation from the straight line or more slope witnessed for the heteroatom doped, activated sample is due to the pseudocapacitance contribution from oxygen, nitrogen, and phosphorus functional groups. While the textural properties induced by H_3PO_4 activation along with the P-doping can generate pathways for the transportation of ions and electrons, the N-doping can facilitate fast ion mobility. Hence, it can be concluded that the enhanced electrochemical performance of NPG_A is owing to the contribution of both electric double-layer behavior and pseudocapacitive behavior. The inset shows the equivalent circuit diagram for the Nyquist plot. The resistance offered by the cell bulk system involved with solution resistance is represented by R_1. The resistance at electrode-electrolyte interface and capacitance due to electric double layer is represented by R_2 and C_2, respectively. The resistance due to the charge-transfer resistance and capacitance due to the diffusion of ions are represented by R_3 and C_3, respectively. W is related to the Warburg impedance.

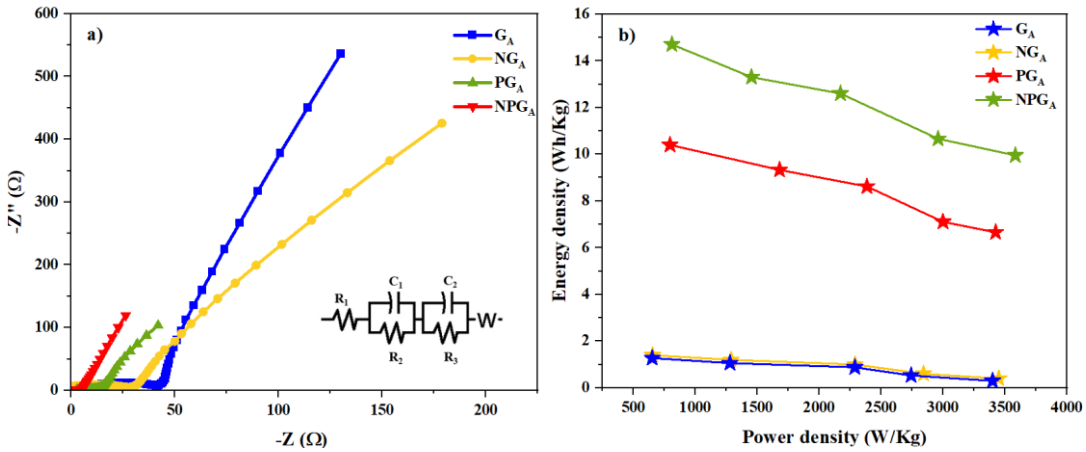

Fig. 40 a) Nyquist plot (Inset: equivalent circuit) b) Ragone plot of doped (NG_A, PG_A, NPG_A) and undoped (G_A) activated multilayer graphene derivatives

In any high-performance supercapacitor, its electrode material should show significant energy

density along with high power density. The Ragone plot which demonstrates the variation of energy densities with corresponding power densities is illustrated in Fig.40b.As per the experimental results, at a power density of 812 W/kg, NPG_A by the virtue of the synergistic effect of the heteroatoms, showed the maximum energy density of 14 Wh/kg at 1 A/g current density. At the similar power density, PG_A, NG_A, and G_A modified electrodes showed the energy density of 10.4 Wh/kg, 1.4 Wh/kg, and 1.2 Wh/kg, respectively. Thus, the higher specific capacitance value, low charge transfer resistance, significant energy, and power densities confirm the reliability of the NPG_A as an electrode material for supercapacitor.

5.3.5 Conclusion

The study demonstrates the facile preparation of a simultaneous heteroatom doped and activated hybrid electrode material composed of a hierarchical micro-meso porous structure for the fabrication of high-performance supercapacitor. The as-synthesized multilayer graphene derivatives showed the presence of high content of nitrogen and phosphorus, enriched defect densities, and high surface area. The co-doped multilayer graphene derivative exhibits a maximum specific capacitance of 322 F/g and 167 F/g in 3-electrode and 2-electrode cells, respectively. Moreover, it delivered an energy density of 14 Wh/kg along with power density of 812 W/kg at current density of 1A/g. Thus, the symmetrical triangular shape, high capacitance values, negligible IR drop, noteworthy cyclic stability, and low charge-transfer resistance value suggest the excellent performance of NPG_A as a supercapacitor electrode material.

6. SUMMARY AND FUTURE PROSPECTS

In summary, the utilization of fossil fuel coke for fabricating multilayer graphene derivative via facile, cost-effective, and scalable synthesis technique and its physio-chemical modifications achieved through the doping of heteroatoms namely, nitrogen and phosphorus for fluorescence bioimaging, electrochemical sensing, and supercapacitor applications, have been established in the current study.

Coke-based graphite oxide (GrO) obtained via Improved Hummers' method possesses an oxidized and defected multilayer graphene structure. The sp^2 domains and surface defect states of the as-synthesized GrO rendered multi-emissive fluorescence emission attributes. The abundant active sites induced in the graphitic structure favor the quick propagation of charges/ions, and thus contribute towards its superior electrochemical behavior. The results are captivating, implying that these optical and electrochemical characteristics of coke-derived

multilayer graphene structures can be further tailored for several potential applications.

The heteroatom doped coke-based multilayer graphene derivatives (PG_H, NG_H, NPG_H) with various structures, morphologies, surface chemistries, and elemental compositions are synthesized via one-pot hydrothermal method. The as-prepared heteroatom doped multilayer graphene derivatives own the presence of phosphorus and nitrogen atoms at doping concentrations of (N: 3.92 At %, P: 1.73 At %), (P: 2.89 At %), and (N: 5.92 At %) in NPG_H, PG_H, and NG_H, respectively. The nitrogen doping enhanced their luminescence characteristics resulting in high-quantum yield and long fluorescence lifetime, best suited for fluorescence bioimaging applications. The co-doped multilayer graphene derivative demonstrated superior electrochemical characteristics and sensing performance. It was utilized for the electrochemical sensing of a potentially hazardous drug, oxytocin. with a lower detection of a limit of 0.04 nM.

The simultaneous heteroatom doping and activation were achieved via thermal annealing of the coke-based graphite oxide along with nitrogen and phosphorus precursors to produce heteroatom-doped multilayer graphene derivatives, namely, NG_A, PG_A, and NPG_A. The structure, morphologies, surface chemistry, and electrochemical characteristics of PG_A, and NPG_A samples were completely distinct, due to the role of H_3PO_4 as a phosphorus precursor as well as an activation agent. Especially, NPG_A obtained via co-doping of heteroatoms showed the best electrochemical behaviour with a specific capacitance of 322 F/g and 167 F/g in 3-electrode and 2-electrode cells, respectively. The good capacitive properties may be attributed to the high surface area, hierarchical pore structure, and synergistic effect of heteroatoms.

The scope of future work involves the achievement of precise control of the doping concentration and surface chemistry of heteroatom atom doped multilayer graphene derivatives for the enhancement of fluorescence characteristics, sensing performance, and energy storage capabilities in terms of quantum yield, sensing specificity, and extended potential window, respectively which would lead to more developments in the commercialization of coke-based multilayer structures.

7. STRUCTURE OF THE THESIS

The thesis would be designed to include eight chapters. Chapter 1 would encompass a detailed introduction to the heteroatom doped graphene structures, including their preparation, properties, applications, and significance of coke as a precursor among other expensive precursors would be discussed. Chapter 2 would be devoted to reviewing the existing literature outlining the implication and applicability of heteroatom doping, especially nitrogen and phosphorus atoms. An overview of the research methodology adopted for the current work

would be presented in Chapter 3. Chapter 4 would elaborate on the fabrication and investigation of the optical and electrochemical properties of coke-based oxidized multilayer graphene structure would be discussed. The synthesis and characterization of heteroatom doped multilayer graphene derivative and its potential application in fluorescence bioimaging and selective electrochemical sensing of oxytocin would be presented in Chapter 5. Chapter 6 would discuss the preparation and analyses of heteroatom doped, activated multilayer graphene derivatives as an electrode material for supercapacitor. Finally, Chapter 7 would present a detailed summary and conclusions derived from the current work along with a sight of the scope for future work.

BIBLIOGRAPHY

[1] A. T. Didеikin and A. Y. Vul', "Graphene oxide and derivatives: The place in graphene family," *Frontiers in Physics*, vol. 6, no. JAN, p. 149, 2019, doi: 10.3389/FPHY.2018.00149/BIBTEX.

[2] H. Grajek, J. Jonik, Z. Witkiewicz, T. Wawer, and M. Purchała, "Applications of Graphene and Its Derivatives in Chemical Analysis," *Crit Rev Anal Chem*, vol. 50, no. 5, pp. 445–471, Sep. 2020, doi: 10.1080/10408347.2019.1653165.

[3] M. C. Pierce, D. J. Javier, and R. Richards-Kortum, "Optical contrast agents and imaging systems for detection and diagnosis of cancer," *International journal of cancer. Journal international du cancer*, vol. 123, no. 9, p. 1979, Nov. 2008, doi: 10.1002/IJC.23858.

[4] A. M. Derfus, W. C. W. Chan, and S. N. Bhatia, "Probing the Cytotoxicity of Semiconductor Quantum Dots," *Nano Letters*, vol. 4, no. 1, pp. 11–18, Jan. 2004, doi: 10.1021/NL0347334.

[5] V. Kumar *et al.*, "Development and Validation of an HPLC Method for Oxytocin in Ringer's Lactate and its Application in Stability Analysis," *http://dx.doi.org/10.1080/10826070600864742*, vol. 29, no. 16, pp. 2353–2365, Sep. 2007, doi: 10.1080/10826070600864742.

[6] R. Haselberg, V. Brinks, A. Hawe, G. J. de Jong, and G. W. Somsen, "Capillary electrophoresis-mass spectrometry using noncovalently coated capillaries for the analysis of biopharmaceuticals," *Analytical and Bioanalytical Chemistry*, vol. 400, no. 1, pp. 295–303, Apr. 2011, doi: 10.1007/S00216-011-4738-4/TABLES/2.

[7] G. Leng and N. Sabatier, "Measuring Oxytocin and Vasopressin: Bioassays, Immunoassays and Random Numbers," *J Neuroendocrinol*, vol. 28, no. 10, Oct. 2016, doi: 10.1111/JNE.12413.

[8] F. A. Liu *et al.*, "Modified Sawhorse Waveform for the Voltammetric Detection of Oxytocin," *J Electrochem Soc*, vol. 169, no. 1, p. 017512, Jan. 2022, doi: 10.1149/1945-7111/AC4AAE.

[9] K. Asai, T. A. Ivandini, and Y. Einaga, "Continuous and selective measurement of oxytocin and vasopressin using boron-doped diamond electrodes," *Scientific Reports 2016 6:1*, vol. 6, no. 1, pp. 1–10, Sep. 2016, doi: 10.1038/srep32429.

[10] S. Huang, X. Zhu, S. Sarkar, and Y. Zhao, "Challenges and opportunities for supercapacitors," *APL Materials*, vol. 7, no. 10, p. 100901, Oct. 2019, doi: 10.1063/1.5116146.

[11] H. Ji *et al.*, "ARTICLE Capacitance of carbon-based electrical double-layer capacitors," *Nature Communications*, 2014, doi: 10.1038/ncomms4317.

[12] Y. Liu, S. P. Jiang, and Z. Shao, "Intercalation pseudocapacitance in electrochemical energy storage: recent advances in fundamental understanding and materials development," *Materials Today Advances*, vol. 7, p. 100072, Sep. 2020, doi: 10.1016/J.MTADV.2020.100072.

[13] J. Ju, R. Zhang, S. He, and W. Chen, "Nitrogen-doped graphene quantum dots-based fluorescent probe for the sensitive turn-on detection of glutathione and its cellular imaging," *RSC Advances*, vol. 4, no. 94, pp. 52583–52589, Oct. 2014, doi: 10.1039/C4RA10601F.

[14] R. Santhosh *et al.*, "Heteroatom doped graphene based hybrid electrode materials for supercapacitor applications," *Electrochimica Acta*, vol. 276, pp. 284–292, Jun. 2018, doi: 10.1016/J.ELECTACTA.2018.04.142.

[15] S. Kaushal, M. Kaur, N. Kaur, V. Kumari, and P. P. Singh, "Heteroatom-doped graphene as sensing materials: a mini review," *RSC Advances*, vol. 10, no. 48, pp. 28608–28629, Aug. 2020, doi: 10.1039/D0RA04432F.

[16] X. Kou, S. Jiang, S. J. Park, and L. Y. Meng, "A review: recent advances in preparations and applications of heteroatom-doped carbon quantum dots," *Dalton Transactions*, vol. 49, no. 21, pp. 6915–6938, Jun. 2020, doi: 10.1039/D0DT01004A.

[17] C. Yu, Z. Liu, X. Meng, B. Lu, D. Cui, and J. Qiu, "Nitrogen and phosphorus dual-doped graphene as a metal-free high-efficiency electrocatalyst for triiodide reduction," *Nanoscale*, vol. 8, no. 40, pp. 17458–17464, Oct. 2016, doi: 10.1039/C6NR00839A.

[18] R. Li, Z. Wei, and X. Gou, "Nitrogen and Phosphorus Dual-Doped Graphene/Carbon Nanosheets as Bifunctional Electrocatalysts for Oxygen Reduction and Evolution," *ACS Catalysis*, vol. 5, no. 7, pp. 4133–4142, May 2015, doi: 10.1021/ACSCATAL.5B00601/SUPPL_FILE/CS5B00601_SI_001.PDF.

[19] A. Ananthanarayanan *et al.*, "Nitrogen and phosphorus co-doped graphene quantum dots: synthesis from adenosine triphosphate, optical properties, and cellular imaging," *Nanoscale*, vol. 7, no. 17, pp. 8159–8165, Apr. 2015, doi: 10.1039/C5NR01519G.

[20] A. Singh and A. K. Ojha, "Coal derived graphene as an efficient supercapacitor electrode material," *Chemical Physics*, vol. 530, Feb. 2020, doi: 10.1016/J.CHEMPHYS.2019.110607.

[21] M. Bora, D. Bhattacharjya, and B. K. Saikia, "Coal-Derived Activated Carbon for Electrochemical Energy Storage: Status on Supercapacitor, Li-Ion Battery, and Li-S Battery Applications," *Energy and Fuels*, vol. 35, no. 22, pp. 18285–18307, Nov. 2021, doi: 10.1021/ACS.ENERGYFUELS.1C02518/ASSET/IMAGES/MEDIUM/EF1C02518_0014.GIF.

[22] Q. Meng and Z. Li, "Molecular imaging probes for diagnosis and therapy evaluation of breast cancer," *International Journal of Biomedical Imaging*, vol. 2013, 2013, doi: 10.1155/2013/230487.

[23] G. K. Yogesh, E. P. Shuaib, P. Roopmani, M. B. Gumpu, U. M. Krishnan, and D. Sastikumar, "Synthesis, characterization and bioimaging application of laser-ablated graphene-oxide nanoparticles (nGOs)," *Diamond and Related Materials*, vol. 104, p. 107733, Apr. 2020, doi: 10.1016/J.DIAMOND.2020.107733.

[24] E. v. Suprun, “Direct electrochemistry of proteins and nucleic acids: The focus on 3D structure,” *Electrochemistry Communications*, vol. 125, p. 106983, Apr. 2021, doi: 10.1016/J.ELECOM.2021.106983.

[25] A. G. Zestos, F. A. Liu, and T. Asrat, “Oxytocin Peptide Detection with Carbon Electrodes and Fast Scan Cyclic Voltammetry,” *ECS Meeting Abstracts*, vol. MA2021-01, no. 63, p. 1677, May 2021, doi: 10.1149/MA2021-01631677MTGABS.

[26] P. S. Sharma *et al.*, “Synthesis and application of a ‘plastic antibody’ in electrochemical microfluidic platform for oxytocin determination,” *Biosensors and Bioelectronics*, vol. 100, pp. 251–258, Feb. 2018, doi: 10.1016/J.BIOS.2017.09.009.

[27] Z. Zhang, W. L. Bai, K. X. Wang, and J. S. Chen, “Electrocatalyst design for aprotic Li–CO2 batteries,” *Energy & Environmental Science*, vol. 13, no. 12, pp. 4717–4737, Dec. 2020, doi: 10.1039/D0EE03058A.

[28] Y. Deng, Y. Ji, H. Wu, and F. Chen, “Enhanced electrochemical performance and high voltage window for supercapacitor based on multi-heteroatom modified porous carbon materials,” *Chemical Communications*, vol. 55, no. 10, pp. 1486–1489, Jan. 2019, doi: 10.1039/C8CC08391F.

[29] “US7623340B1 - Nano-scaled graphene plate nanocomposites for supercapacitor electrodes - Google Patents.” https://patents.google.com/patent/US7623340B1/en (accessed May 23, 2022).

[30] M. Mirzaeian, Q. Abbas, D. Gibson, and M. Mazur, “Effect of nitrogen doping on the electrochemical performance of resorcinol-formaldehyde based carbon aerogels as electrode material for supercapacitor applications,” *Energy*, vol. 173, pp. 809–819, Apr. 2019, doi: 10.1016/J.ENERGY.2019.02.108.

[31] Q. Abbas, R. Raza, I. Shabbir, and A. G. Olabi, “Heteroatom doped high porosity carbon nanomaterials as electrodes for energy storage in electrochemical capacitors: A review,” *Journal of Science: Advanced Materials and Devices*, vol. 4, no. 3, pp. 341–352, Sep. 2019, doi: 10.1016/J.JSAMD.2019.07.007.

[32] L. S. K. Pang, A. M. Vassallo, and M. A. Wilson, “Fullerenes from coal,” *Nature (London); (United Kingdom)*, vol. 350:6335, no. 6335, p. 480, 1991, doi: 10.1038/352480A0.

[33] S. Hashmi, A. Mushtaq, R. Ahmed, and Z. U. Ali, “Synthesis and Characterization of Reduced Graphene Oxide from Indigenous Coal: A Non-Burning Solution,” *International Journal of Membrane Science and Technology*, vol. 9, no. 1, pp. 1–12, 2022, doi: 10.15379/2410-1869.2022.09.01.01.

[34] Q. T. Ain, S. H. Haq, A. Alshammari, M. A. Al-Mutlaq, and M. N. Anjum, “The systemic effect of PEG-nGO-induced oxidative stress in vivo in a rodent model,” *Beilstein Journal of Nanotechnology*, vol. 10, pp. 901–911, 2019, doi: 10.3762/BJNANO.10.91.

[35] T. Wang, L. X. Wang, D. L. Wu, W. Xia, and D. Z. Jia, “Interaction between nitrogen and sulfur in co-doped graphene and synergetic effect in supercapacitor,” *Sci Rep*, vol. 5, Mar. 2015, doi: 10.1038/SREP09591.

[36] N. A. El-Hussiny, A. A. Khalifa, A. A. El-Midany, A. A. Ahmed, and M. E. H. Shalabi, “Effect of replacement coke breeze by charcoal on technical operation of iron ore sintering,” *Int J Sci Eng Res*, vol. 6, pp. 681–686, 2015.

[37] J. J. Ahn *et al.*, “Inter-Laboratory study to define the temperature interval for a thermoluminescence heating unit used to identify irradiated food,” *Food Science and*

Biotechnology 2012 21:3, vol. 21, no. 3, pp. 853–857, Jun. 2012, doi: 10.1007/S10068-012-0110-5.

[38] A. C. Ferrari, "Raman spectroscopy of graphene and graphite: Disorder, electron–phonon coupling, doping and nonadiabatic effects," *Solid State Communications*, vol. 143, no. 1–2, pp. 47–57, Jul. 2007, doi: 10.1016/J.SSC.2007.03.052.

[39] A. M. Dimiev and J. M. Tour, "Mechanism of graphene oxide formation," *ACS Nano*, vol. 8, no. 3, pp. 3060–3068, Mar. 2014, doi: 10.1021/NN500606A/SUPPL_FILE/NN500606A_SI_001.PDF.

[40] S. Y. Lee and R. L. Mahajan, "A facile method for coal to graphene oxide and its application to a biosensor," *Carbon N Y*, vol. 181, pp. 408–420, Aug. 2021, doi: 10.1016/J.CARBON.2021.05.007.

[41] A. E. F. Oliveira, G. B. Braga, C. R. T. Tarley, and A. C. Pereira, "Thermally reduced graphene oxide: synthesis, studies and characterization," *Journal of Materials Science*, vol. 53, no. 17, pp. 12005–12015, Sep. 2018, doi: 10.1007/S10853-018-2473-3/FIGURES/9.

[42] F. Zheng, W.-L. Xu, H.-D. Jin, X.-T. Hao, and K. P. Ghiggino, "Charge transfer from poly (3-hexylthiophene) to graphene oxide and reduced graphene oxide," *RSC Adv*, vol. 5, no. 109, pp. 89515–89520, 2015.

[43] P. Kumar, B. Sain, and S. L. Jain, "Photocatalytic reduction of carbon dioxide to methanol using a ruthenium trinuclear polyazine complex immobilized on graphene oxide under visible light irradiation," *Journal of Materials Chemistry A*, vol. 2, no. 29, pp. 11246–11253, 2014.

[44] G. Xing *et al.*, "Solution-Processed Tin-Based Perovskite for Near-Infrared Lasing," *Advanced Materials*, vol. 28, no. 37, pp. 8191–8196, Oct. 2016, doi: 10.1002/ADMA.201601418.

[45] P. Dutta *et al.*, "Excitation wavelength dependent UV fluorescence of dispersed modified graphene oxide: Effect of pH," *Journal of Luminescence*, vol. 168, pp. 269–275, Dec. 2015, doi: 10.1016/J.JLUMIN.2015.08.033.

[46] B. Manoj, A. M. Raj, and G. C. Thomas, "Tailoring of low grade coal to fluorescent nanocarbon structures and their potential as a glucose sensor," *Scientific Reports 2018 8:1*, vol. 8, no. 1, pp. 1–9, Sep. 2018, doi: 10.1038/s41598-018-32371-9.

[47] M. Sohail *et al.*, "Modified and improved Hummer's synthesis of graphene oxide for capacitors applications," *Modern Electronic Materials*, vol. 3, no. 3, pp. 110–116, Sep. 2017, doi: 10.1016/J.MOEM.2017.07.002.

[48] B. Xu *et al.*, "What is the choice for supercapacitors: graphene or graphene oxide?," *Energy & Environmental Science*, vol. 4, no. 8, pp. 2826–2830, Aug. 2011, doi: 10.1039/C1EE01198G.

[49] P. Dharmalingam, V. Ramanan, G. G. Karthikeyan, N. S. Palani, R. Ilangovan, and P. Ramamurthy, "A study on the electrochemical performance of nitrogen and oxygen co-doped carbon dots derived from a green precursor for supercapacitor applications," *Journal of Materials Science: Materials in Electronics*, vol. 28, no. 24, pp. 18489–18496, Dec. 2017, doi: 10.1007/S10854-017-7796-3.

[50] X. Chen and T. T. Lim, "Highly-efficient peroxymonosulfate activation for sulfacetamide degradation over nitrogen-functionalized graphene: The effect of thermal annealing temperature on reactive functional groups," *Chemical Engineering Transactions*, vol. 73, pp. 145–150, 2019, doi: 10.3303/CET1973025.

[51] B. J. Matsoso, K. Ranganathan, B. K. Mutuma, T. Lerotholi, G. Jones, and N. J. Coville, "Time-dependent evolution of the nitrogen configurations in N-doped graphene films," *RSC Advances*, vol. 6, no. 108, pp. 106914–106920, Nov. 2016, doi: 10.1039/C6RA24094A.

[52] P. R. Kharangarh, S. Umapathy, and G. Singh, "Effect of defects on quantum yield in blue emitting photoluminescent nitrogen doped graphene quantum dots," *Journal of Applied Physics*, vol. 122, no. 14, Oct. 2017, doi: 10.1063/1.4991693.

[53] Y. Jia, K. Jiang, H. Wang, and X. Yao, "The Role of Defect Sites in Nanomaterials for Electrocatalytic Energy Conversion," *Chem*, vol. 5, no. 6, pp. 1371–1397, Jun. 2019, doi: 10.1016/J.CHEMPR.2019.02.008.

[54] Z. A. Alothman, "A review: Fundamental aspects of silicate mesoporous materials," *Materials*, vol. 5, no. 12, pp. 2874–2902, 2012, doi: 10.3390/MA5122874.

[55] "[PDF] Preparation and Characterization of Nitrogen Doped Reduced Graphene Oxide Sheet | Semantic Scholar." https://www.semanticscholar.org/paper/Preparation-and-Characterization-of-Nitrogen-Doped-Mageed-Radiah/3e9a5e23dcad49adb73382fa8cb4889b788a04a0 (accessed May 04, 2022).

[56] W. Zhang, P. Wu, Z. Li, and J. Yang, "First-principles thermodynamics of graphene growth on Cu surfaces," *Journal of Physical Chemistry C*, vol. 115, no. 36, pp. 17782–17787, Sep. 2011, doi: 10.1021/JP2006827/SUPPL_FILE/JP2006827_SI_001.PDF.

[57] X. Mu, B. Yuan, X. Feng, S. Qiu, L. Song, and Y. Hu, "The effect of doped heteroatoms (nitrogen, boron, phosphorus) on inhibition thermal oxidation of reduced graphene oxide," *RSC Advances*, vol. 6, no. 107, pp. 105021–105029, Nov. 2016, doi: 10.1039/C6RA21329D.

[58] M. Ozhukil Valappil, M. Ahlawat, V. K. Pillai, and S. Alwarappan, "A single-step, electrochemical synthesis of nitrogen doped blue luminescent phosphorene quantum dots," *Chemical Communications*, vol. 54, no. 83, pp. 11733–11736, Oct. 2018, doi: 10.1039/C8CC07266C.

[59] B. Liu, C. M. Yang, Z. Liu, and C. S. Lai, "N-Doped Graphene with Low Intrinsic Defect Densities via a Solid Source Doping Technique," *Nanomaterials (Basel)*, vol. 7, no. 10, Oct. 2017, doi: 10.3390/NANO7100302.

[60] R. Li, Z. Wei, X. Gou, and W. Xu, "Phosphorus-doped graphene nanosheets as efficient metal-free oxygen reduction electrocatalysts," *RSC Advances*, vol. 3, no. 25, pp. 9978–9984, Jun. 2013, doi: 10.1039/C3RA41079J.

[61] X. Chen, X. Wang, and D. Fang, "A review on C1s XPS-spectra for some kinds of carbon materials," *https://doi.org/10.1080/1536383X.2020.1794851*, pp. 1048–1058, 2020, doi: 10.1080/1536383X.2020.1794851.

[62] F. G. Pacheco, A. A. C. Cotta, H. F. Gorgulho, A. P. Santos, W. A. A. Macedo, and C. A. Furtado, "Comparative temporal analysis of multiwalled carbon nanotube oxidation reactions: Evaluating chemical modifications on true nanotube surface," *Applied Surface Science*, vol. 357, pp. 1015–1023, Dec. 2015, doi: 10.1016/J.APSUSC.2015.09.054.

[63] S. Sakulsermsuk, P. Singjai, and C. Chaiwong, "Influence of plasma process on the nitrogen configuration in graphene," *Diamond and Related Materials*, vol. 70, pp. 211–218, Nov. 2016, doi: 10.1016/J.DIAMOND.2016.11.001.

[64] C. Huang, T. Sun, and D. Hulicova-Jurcakova, "Wide electrochemical window of supercapacitors from coffee bean-derived phosphorus-rich carbons," *ChemSusChem*, vol. 6, no. 12, pp. 2330–2339, 2013, doi: 10.1002/CSSC.201300457.

[65] Y. T. Yew, Z. Sofer, C. C. Mayorga-Martinez, and M. Pumera, "Black phosphorus nanoparticles as a novel fluorescent sensing platform for nucleic acid detection," *Materials Chemistry Frontiers*, vol. 1, no. 6, pp. 1130–1136, Jun. 2017, doi: 10.1039/C6QM00341A.

[66] R. Langer *et al.*, "Tailoring Electronic and Magnetic Properties of Graphene by Phosphorus Doping," *ACS Applied Materials and Interfaces*, vol. 12, no. 30, pp. 34074–34085, Jul. 2020, doi: 10.1021/ACSAMI.0C07564/SUPPL_FILE/AM0C07564_SI_001.PDF.

[67] A. R. MacIntosh *et al.*, "Phosphorus and Nitrogen Centers in Doped Graphene and Carbon Nanotubes Analyzed through Solid-State NMR," *Journal of Physical Chemistry C*, vol. 122, no. 12, pp. 6593–6601, Mar. 2018, doi: 10.1021/ACS.JPCC.7B11671/SUPPL_FILE/JP7B11671_SI_001.PDF.

[68] M. Figueras, I. J. Villar-Garcia, F. Vines, C. Sousa, V. A. de La Pena O'Shea, and F. Illas, "Correcting Flaws in the Assignment of Nitrogen Chemical Environments in N-Doped Graphene," *Journal of Physical Chemistry C*, vol. 123, no. 17, pp. 11319–11327, May 2019, doi: 10.1021/ACS.JPCC.9B02554/SUPPL_FILE/JP9B02554_SI_001.PDF.

[69] J. Li *et al.*, "Highly N,P-doped carbon dots: Rational design, photoluminescence and cellular imaging," *Microchimica Acta*, vol. 184, no. 8, pp. 2933–2940, Aug. 2017, doi: 10.1007/S00604-017-2314-0/FIGURES/6.

[70] V. K. Singh *et al.*, "Bright-blue-emission nitrogen and phosphorus-doped carbon quantum dots as a promising nanoprobe for detection of Cr(VI) and ascorbic acid in pure aqueous solution and in living cells," *New Journal of Chemistry*, vol. 42, no. 15, pp. 12990–12997, Jul. 2018, doi: 10.1039/C8NJ02126K.

[71] J. Tang *et al.*, "Influence of Group Modification at the Edges of Carbon Quantum Dots on Fluorescent Emission," *Nanoscale Research Letters*, vol. 14, no. 1, Dec. 2019, doi: 10.1186/S11671-019-3079-7.

[72] G. Yang *et al.*, "Exploring the Emissive States of Heteroatom-Doped Graphene Quantum Dots," *Journal of Physical Chemistry C*, vol. 122, no. 11, pp. 6483–6492, Mar. 2018, doi: 10.1021/ACS.JPCC.8B01385/SUPPL_FILE/JP8B01385_SI_001.PDF.

[73] M. K. Barman, B. Jana, S. Bhattacharyya, and A. Patra, "Photophysical properties of doped carbon dots (N, P, and B) and their influence on electron/hole transfer in carbon dots-nickel (II) phthalocyanine conjugates," *Journal of Physical Chemistry C*, vol. 118, no. 34, pp. 20034–20041, 2014, doi: 10.1021/JP507080C/SUPPL_FILE/JP507080C_SI_001.PDF.

[74] C. G. Zoski, J. Leddy, Drew. Dunwoody, and A. J. Bard, "Student solutions manual : to accompany Electrochemical methods : fundamentals and applications, second edition [by] Allen J. Bard, Larry R. Faulkner," p. 145.

[75] P. Zhao, R. N. Zare, and H. Chen, "Absolute Quantitation of Oxidizable Peptides by Coulometric Mass Spectrometry," *J Am Soc Mass Spectrom*, vol. 30, no. 11, pp. 2398–2407, Nov. 2019, doi: 10.1007/S13361-019-02299-Z.

[76] B. v. Sarada, T. N. Rao, D. A. Tryk, and A. Fujishima, "Electrochemical Oxidation of Histamine and Serotonin at Highly Boron-Doped Diamond Electrodes," *Analytical Chemistry*, vol. 72, no. 7, pp. 1632–1638, Apr. 2000, doi: 10.1021/AC9908748.

[77] H. Yi, K. Wu, S. Hu, and D. Cui, "Adsorption stripping voltammetry of phenol at Nafion-modified glassy carbon electrode in the presence of surfactants," *Talanta*, vol. 55, no. 6, pp. 1205–1210, Dec. 2001, doi: 10.1016/S0039-9140(01)00531-8.

[78] P. S. Sharma *et al.*, "Synthesis and application of a 'plastic antibody' in electrochemical microfluidic platform for oxytocin determination," *Biosensors and Bioelectronics*, vol. 100, pp. 251–258, Feb. 2018, doi: 10.1016/J.BIOS.2017.09.009.

[79] R. Rani, S. Medhe, K. R. Raj, and M. Srivastava, "Standardization of HPTLC method for the estimation of oxytocin in edibles," *Journal of Food Science and Technology*, vol. 50, no. 6, p. 1222, Dec. 2013, doi: 10.1007/S13197-013-1036-5.

LIST OF PUBLICATIONS

Journal Publications

1. **Riya Thomas** & Manoj B. Luminescence and energy storage characteristics of coke-based graphite oxide. *Materials Chemistry and Physics.* 257:123854. http://dx.doi.org/10.1016/j. matchemphys.2020.123854 (Impact factor –4.09)
2. Ramya, A. V., **Riya, Thomas,** & Manoj, B. Mesoporous onion-like carbon nanostructures from natural oil for high-performance supercapacitor and electrochemical sensing applications: Insights into the post-synthesis sonochemical treatment on the electrochemical performance. *Ultrasonics Sonochemistry*. 79 p.105767. https://doi.org/10.1016/j .ultsonch.2021.105767 (Impact factor – 7.491)
3. **Riya Thomas** & Manoj B. Antibacterial performance of GO–Ag nanocomposite prepared via ecologically safe protocols. *Applied Nanoscience*. 10(11):4207-19. https://doi.org/ 10.1007/s13204-020-01539-z **(**Impact factor -3.67)
4. **Riya Thomas** & Manoj B. Electrochemical efficacies of coal derived nanocarbons. *International Journal of Coal Science & Technology*. 2020:1-4. https://doi.org/ 10.1007/s40789-020-00379-0 (SJR - 0.94)
5. **Riya Thomas** & Manoj B. Dielectric performance of graphene nanostructures prepared from naturally sourced material. *Materials Today: Proceedings*. 2021, 1;43:3424-7. https://doi.org /10.1016/j.matpr.2020.09.075(SJR – 0.35)
6. Aleena Ann Mathew, Meera Antony, **Riya Thomas** & Manoj B. Fluorescent PVDF dots: from synthesis to biocidal activity *Polymer Bulletin,* 1-18. https://doi.org/10. 1007/s00289-022-04096-3 **(**Impact factor -2.87)
7. Shivanand Chougle, Anna Mary, **Riya Thomas** & Manoj B. Quantifying the role of nanocarbon fillers on dielectric properties of PVDF matrix. *Polymer and polymer composites* https://doi.org/10.1177%2F09673911221087597 (Impact factor -2.00)
8. Jicksy Joy, Mithun sanady, **Riya Thomas** & Manoj B. Biosynthesized Ag Nanoparticles: a

Promising Pathway for Bandgap Tailoring, ***Biointerface Research in Applied Chemistry*****,** 11: 8875–8883. https://doi.org/10.33263/BRIAC112.88758883. (SJR - 0.25)

9. Annpriya Johnson, Devika Santhosh, **Riya Thomas,** Elcey C & Manoj B. Non-antibacterial carbon particles and its fluorescence properties. ***ECS Transactions,*** https://doi.org/10.1149/10701.9015ecst (SJR - 0.21)

Manuscripts communicated

1. Heteroatom Engineered Graphene Based Electrochemical Assay for the Quantification of High-Risk Abused Drug Oxytocin in Edibles and Biological Samples (Submitted to food chemistry - Under revision)
2. Probing heteroatom doped graphene derivatives for bioimaging applications of human melanoma cells. (Communicated to the Journal of photochemistry and photobiology:A)
3. Simultaneous heteroatom doped and activated coke-based graphene derivatives for supercapacitor applications (Communicated to the Journal of Electrochimica Acta)

Other Publications

1. **Riya Thomas**, Jayaseeli E, Sharma NS & Manoj B. Opto-electric property relationship in phosphorus embedded nanocarbon. *Results in Physics*. 10:633-9. (Impact Factor:4.56)
2. Mututu V, Sunitha AK, **Riya Thomas**, Pandey M, Manoj B. An investigation on structural, electrical and optical properties of GO/ZnO nanocomposite. Int. J. Electrochem. 14(3752-3763):3752. (Impact Factor:1.76)

Book Chapters

1. **Riya Thomas** & Manoj B. Fabrication approaches in graphene for supercapacitors. Graphene as Energy storage materials for supercapacitors, *Materials Research forum LLC, USA,* 64, 1-24.
2. **Riya Thomas** & Manoj B. Application of Nanomaterials in Fuel Cell and Photovoltaic System *Nanotechnology for Electronic Applications*, 149-167.

Patent published

1. **Riya Thomas & Manoj B.** Heteroatom doped coke-based nanocarbon for the detection of oxytocin. IN Patent E-101/9805/2021- CHE.
2. **Riya Thomas & Manoj B.** Development of nitrogen-doped multilayer graphene derivative from coke for imaging biomarker applications IN Patent E-101/9283/2022- CHE

Patents communicated

1. **Riya Thomas & Manoj B.** Fabrication of heteroatom doped, activated graphene-based architecture derived from coke as supercapacitor electrode material

List of conferences and workshops attended

1. Participated and presented a paper in *International Conference on Physics of Materials and Nanotechnology (ICPN)* happened at Mangalore University, India
2. Participated and presented a paper in the *International Conference At 11th Bangalore Nano 2020* organized by DST and government of Karnataka
3. Participated and presented a paper in the *International Conference 5 Nano 2020* organized by Mangalam college of Engineering, Kottayam, Kerala
4. Participated and presented a paper in *Mesmac International Conference on Applying theory: Paradigms, Practices and Faultlines* happened at MES Mampad college, Kerala, India
5. Attended the *National Workshop On Advanced Analytical Techniques In Material Science (WAATMS)* at University of Calicut, Kerala
6. Participated in the state level workshop on *Recent trends in Nanoscience* in Jyothi Nivas College, Bangalore
7. Participated in the *E-poster competition* conducted by Nesamony memorial Christian college, Marthandam, Kanyakumari
8. Participated in *20-days virtual summer school on "Nanoscience and Nanomaterials"* organized by University of madras
9. Attended *one day national webinar on "Modern Scientific Trends In Research Methodology"* organized by jagadguru college, *Karnataka*
10. Attended *International online webinar on Supercapacitors* organized by Christ irinjalakuda, Kerala
11. Participated in the workshop on *Raman Spectroscopy* Organized by Bangalore University
12. Participated in *International virtual webinar on "Advanced materials for energy conversion and storage"* organized by sathyabama institute of science and technology, Chennai, Tamilnadu